Characterizing a Mid-IR laser source with a molecular beam

Doctoral Dissertation
Doctoral Program in Metrology (31.st cycle)

Characterizing a Mid-IR laser source with a molecular beam

Davide D'Ambrosio

* * * * * *

Supervisors
Prof. M. Inguscio, Supervisor
Prof. P. De Natale Co-supervisor

Politecnico di Torino
April 29, 2019

I hereby declare that, the contents and organisation of this dissertation constitute my own original work and does not compromise in any way the rights of third parties, including those relating to the security of personal data.

. . . . . .

Davide D'Ambrosio

Turin, April 29, 2019

Summary

High resolution molecular spectroscopy is a powerful tool to test fundamental physics, to measure fundamental constants or even to look for physics beyond QED. An essential ingredient for such experiments is a narrow-linewidth, frequency-stabilized light source, tunable and powerful enough to implement a Doppler-free technique and detect the molecular transition with a good signal-to-noise ratio. Moreover, dealing with molecular transitions, a key spectral region is the Mid-IR, where the strongest vibrational bands of simple molecules can be found. Indeed, the lack of suitable sources and key optical components has represented until now a severe limit for this kind of experiments in the 1–10 µm spectral region. Common spectroscopic methods working above 5 micron wavelength suffer from at least one of these problems: they are feasible only in a narrow spectral range; the laser power available for spectroscopy is limited; the frequency accuracy is poor. To overcome these limitations, we implemented a setup for high-resolution spectroscopy that can be applied in the whole 1–10 µm range. The setup combines the accuracy of a metrological Mid-IR source and the spectral resolution achievable with molecular beams. Our source is based on a quantum cascade laser (QCL), which provides tens of mW optical power, and on a coherent source relying on difference-frequency (DF) generation in a nonlinear crystal. As I will discuss, the latter is linked to the Cs frequency standard and provides high accuracy, which is transferred to the QCL by a phase-lock loop. We measured a vibrational transition in a highly-excited metastable state of CO around 6 µm with 11 digits of precision [35]. The main contribution to the molecular linewidth (900 kHz) was given by residual Doppler breadening.

The core of this thesis is dedicated to the spectral characterization of this source and to the improvement of the resolution of the spectrometer down to the limit given by transit time broadening. These two goals are strictly connected, as we will see. In order to overcome the limit to spectral resolution given by residual Doppler broadening, I modified the experimental setup to reduce the molecules velocity spread. Along z, the molecular beam propagation axis, it depends upon the dimensions and relative distance of the two pulsed UV lasers used to prepare the molecules in the excited metastable state (excitation laser) and to ionize them for detection after interaction with the QCL (ionization laser). I focused as much

as possible these two lasers and made the molecules and the QCL almost collinear, with a small angle of 3.1 degrees, so that the relevant velocity component for the Doppler broadening was the one along the molecular beam axis. This allowed a better selection of the velocity of the molecules and allowed to reduce the Doppler broadening by one order of magnitude, down to 80 kHz.

At the same time, I worked on the improvement of QCL stability. Working on the reduction of the molecular linewidth, I realized that the loop used to phase-lock the QCL to the DF radiation wasn't working at its best, leading to a not optimal laser spectral profile. Substantial improvements in the QCL phase-lock effectiveness led to an enhancement of the QCL power channelled into the DF mode from about 40% up to 70%, a value in line with the best results in literature. Under these new conditions, we expect that the QCL laser replicates the narrow-linewidth feature of its reference DF radiation.

As a final result, we were able to measure molecular transitions with a full width at half maximum of 177 $\pm$ 10 kHz, thus improving the spectral resolution of our spectroscopic apparatus by almost one order of magnitude. We are now almost limited by transit-time bradening.

The high spectral resolution of these measurements allowed also to provide a good estimation of the laser spectral linewidth. Indeed, considering the expected contributions to the line broadening coming from residual Doppler broadening, transit time and inhomogeneity of the magnetic field, an upper limit to the QCL linewidth in optimal locking conditions of few tens of kHz can be set. This estimation is much more precise than that achievable with more standard methods for lasers in our spectral region. As I will discuss in the text, alternative methods can be used to measure the laser linewidth or, better, the laser frequency noise spectral density. Unfortunately, these methods are often not easily implementable in the Mid-IR due to technical or physical limitations, making measurement of frequency noise spectrum of stable lasers a big challenge.

As an example, I measured the source frequency noise power spectral density using the mode of a calcium fluoride whispering gallery mode microresonator which acts as an optical frequency discriminator to convert frequency fluctuations into measurable amplitude fluctuations. Laser spectral linewidth has been calculated via numerical integration. This method proved to be effective in recording the frequency noise spectral density of our source in free-running conditions, but it demonstrated to be unsuited to properly measure the noise of the source in phase-locking conditions because of high dark noise contributions, as I will discuss in the text. Therefore, using this method, I could only measure an upper limit of 700 kHz for the laser linewidth.

Contents

List of Figures VIII

1 Introduction 1

2 Experimental setup 11
2.1 Molecular beam . . . 11
2.2 Excitation laser . . . 15
2.3 Detection laser . . . 15
2.4 Mid-IR frequency generation in OP-GaP . . . 17
2.4.1 Quasi-Phase-Matching and Orientation-Patterned crystals . 17
2.5 6 µm DF generated radiation in OP-GaP . . . 18
2.6 Locking chain . . . 21
2.6.1 Optical frequency standard . . . 21
2.6.2 Optical frequency Comb . . . 22
2.6.3 Near IR lasers phase lock . . . 22
2.6.4 The virtual beatnote method . . . 24
2.6.5 DF linewidth estimation . . . 25
2.6.6 QCL-DFG phase lock effectiveness . . . 25

3 Laser Spectral Characterization 33
3.1 General Noise Theory . . . 33
3.1.1 General properties of noisy signals . . . 33
3.1.2 Laser linewidth and FNPSD . . . 34
3.1.3 Spectral lineshape . . . 37
3.2 Interferometric techniques . . . 39
3.3 Frequency-Amplitude noise conversion . . . 42
3.3.1 Cavities . . . 42
3.3.2 Molecules . . . 43
3.3.3 Line broadening of molecular transitions . . . 44
3.3.4 Sub-Doppler techniques . . . 47
3.4 Molecular beams . . . 47

4 Characterization of the Mid-IR radiation 51
4.1 FNPSD measurement with a WGMR 52
4.2 Laser linewidth measurement on a CO molecular beam 55
4.2.1 Vibrational transition absorption linewidth 56
4.2.2 Line width determination 67

5 Conclusions and Future Perspectives 71

A Knife-edge method 73

References 77

List of Figures

1.1 Transition $a^3\Pi_1 : v = 0, j = 1, + > \rightarrow v = 1, j = 1, - >$. The blue solid line is a Voigt profile fit of the experimental data (red dots). . 5
1.2 Doppler shift compensation 7
1.3 Repeated measurements of the transition line center 9
2.1 C-211 PSV Pulsed Supersonic Valve, from R. M. Jordan Co., Inc. . 12
2.2 Energy level diagram of the CO molecule 13
2.3 A schematic rapresentation of the experiment 14
2.4 Experimental setup for the production of 206 nm radiation 16
2.5 DF generation laser setup 19
2.6 Mid-IR radiation generated as a function of the pump power, for different values of the focusing lens L1. 20
2.7 Metrological grade 6 µm radiation 23
2.8 An overview of the experimental setup for the DFG 6 µm generation. 27
2.9 Beat notes of the different phase-lock loops 28
2.10 Virtual beatnote locking scheme 29
2.11 Phase noise of the free-running QCL (black), of the pump laser (green) and of the DF radiation (red). In the inset, the frequency-noise PSD of the DF radiation is shown. 30
2.12 Phase Lock effectiveness 31
3.1 *1-sided* FNPSD of a quantum cascade laser emitting at 4.3 µm. . . . 38
3.2 A Mach Zehnder interferometer 40
3.3 FNPSD measurement with a frequency-to-amplitude converter . . . 49
4.1 An upper view of the toroidal CaF_2 WGMR. It has 3.6 mm diameter, a FSR of about 19 GHz at 5.8 µm and both input and output beams are coupled via evanescent wave through two Al_2O_3 (sapphire) prisms. 52
4.2 WGMR experimental setup 53
4.3 FNPSD of the 5.8 µm QCL in free-running (black trace) and locked (red trace) conditions 54
4.4 A schematic view of the quasi-collinear configuration. 56
4.5 Excitation (a) and ionization (b) UV lasers waist measurement . . . 57
4.6 Molecular distribution in the z-v_z plane of the phase space in the experiment 58

4.7 Molecular distribution in the v_y-v_z plane of the phase space in the experiment . . . 59
4.8 Simulated Zeeman splitting of the transition $a^3\Pi_1 : |v = 0, j = 1, + > \rightarrow |v = 1, j = 1, - >$ . . . 61
4.9 Zeeman splitting of the $\Delta M = 0$ transitions . . . 62
4.10 Measured $\Delta M = 0$ splitting as a function of the magnets distance> 63
4.11 Permanent magnets field simulation . . . 64
4.12 Transition $a^3\Pi_1 : |v = 0, j = 1, +, 0 > \rightarrow |v = 1, j = 1, -, 0 >$, magnetic field of 875 G. . . . 65
4.13 Excited state population as a function of the Mid-IR laser frequency in a moderate magnetic field regime . . . 66
4.14 The interaction time is set precisely at 20 µs, during which molecules at an average speed of 835 m/s cover 16.7 mm. Our simulation indicates that a moderate magnetic field of about 4.5 G can be, within 20 mm, as regular as 50 mG. . . . 67
4.15 Frequency scan of the QCL over the rovibrational molecular transition 68
A.1 A Gaussian beam propagating along the direction z, with a divergence θ_0 a beam waist w_0 and Rayleigh distance z_R. . . . 74
A.2 Knife edge method experimental setup . . . 75
A.3 A typical recording of the measured power as a function of the blade position along the x axis . . . 76

Chapter 1

Introduction

I would like to remark that part of the work described in this chapter has also been published in [35].

The field of ultracold molecules is quickly growing. Biatomic molecules like SrF [5] and CaF [1, 70], dimers formed by pre-cooled atoms [48, 57] and a polyatomic molecule, SrOH [38], have been already cooled to sub-mK temperatures. Despite the encouraging progress in this field, however, molecule cooling is still a challenging task. Because of several differences, including a higher temperature, the precision of molecular spectroscopy experiments is lower than for their atomic counterpart by more than three orders of magnitude. The main obstacles for molecular cooling arise from the complex internal structure of molecules that makes a closed, two-level system, virtually impossible.

However, the complex internal structure can be exploited for various interesting experiments. For example, molecules can have *enantiomers*. An enantiomer pair is formed by two molecules being one the mirror image of the other, not superposable by a simple reorientation. The Earth biochemistry is based on L-amino acids and D-sugars. A possible explanation for this asymmetry relies on the weak nuclear interaction: it is a non-conserving P interaction [40, 72], and in chiral molecules it is predicted to induce shifts in the energy levels having a different sign for the two enantiomers [33, 59, 41] which, however, have not yet been detected experimentally.

High resolution spectroscopy on cold molecules can shed light on several other aspects of fundamental physics, like the electron dipole moment (EDM) of fundamental particles [19]. According to the Standard Model, the electron charge distribution should not be perfectly spherical. This implies an electron EDM different from zero, although it is predicted to be smaller than $10^{-38} e \cdot cm$ [13]. Extensions of the SM, however, predict a higher value [55], near to the actual tabletop-experiments detection limits.

The most stringent limit on EDM has been set with an experiment performed on a molecular ThO beam [19]: the internal effective electric field inside a polar molecule like ThO can be as high as tens of GV/cm, orders of magnitude higher

than any controlled field created in a laboratory, and one of the highest known among molecules and atoms. The energy associated with a dipole in an electric field is proportional to the field strength, so that an internal electron of a polar molecule is predicted to induce a significant energy shift, if compared with the EDM-induced shift of an electron in an "external" electric field. To date, the upper limit for the EDM is $1.1 \times 10^{-29} e \cdot cm$ [19]. This implies the existence of new supersymmetric particles with a mass of more than TeV/c^{-2} [55, 10]. High resolution spectroscopy experiments on cold molecules, in this case, compete with particle accelerator facilities.

Another interesting application of precision molecular spectroscopy is the determination of the Boltzmann constant. Fundamental units tend to be defined avoiding reliance on manufactured objects. On the 20th May 2019, the Kelvin will be redefined: the former definition of 1/273.16 of the thermodynamic temperature of the triple point of water will be replaced by taking a fixed numerical value for the Boltzmann constant k_B: 1.380 649 $\times 10^{-23}$ when expressed in the unit kg m^2 s^{-2} K^{-1}.

Although the most precise measurement of k_B comes from an accurate measurement of the speed of sound in Argon [54], having a relative uncertainty of 0.71 $\times 10^{-6}$, an independent measurement can be performed with a spectroscopic technique, the Doppler Broadening Thermometry (DBT). The first measurement was performed by Chardonnet and co-workers [22] on a vibrational transition of $^{14}NH_3$ kept in a water-ice bath at 273.15 K. From the determination of the Doppler width of the absorption line, a value as accurate as 2×10^{-4} has been calculated. Similar experiments have been performed on $H_2{}^{18}O$ [47], on a vibrational transition at about 1.39 µm, with a precision of 2.4 $\times 10^{-5}$.

Given the renewed interest in their precise determination, the search for variations of fundamental constants becomes a fundamental issue and represents another question that can be addressed with high resolution molecular spectroscopy. The first to care about possible variation of fundamental phyisical constants was probably Dirac in the 30s [25]. Although the SM does not predict their dependence upon time, space, or matter density, it does not strictly predict their constancy, either. This issue is of fundamental importance. First of all the scientific method is based on the idea that measurements are reproducible in different times and spaces. Moreover, there are many evidences [51, 64, 61] that the universe is expanding at an accelerating rate. From this observation a new form of energy, the dark energy, has been postulated. One of the hypotesis formulated for dark energy is the dynamical action of a scalar field [58]. It has been shown that this field must interact with matter, implying a variation of the fundamental constants [16, 9].

To date, the strictest constrain on the variation of a fundamental constant, the proton-to-electron mass ratio, μ, has been obtained in a molecular spectroscopy experiment: the current higher limit on the fractional temporal variation $\dot{\mu}/\mu = (-3.8 \pm 5.6) \times 10^{-14} \mathrm{yr}^{-1}$ has been measured comparing a vibrational transition in SF_6

with the fundamental hyperfine transition in Cs [65]. Astrophysical observations provide another independent instrument: from the comparison of H_2 Lyman and Werner bands measured in a laboratory and in systems from 12.4 billion years ago, a variation of $\Delta\mu/\mu = (-9.5 \pm 5.4_{\text{stat}} \pm 5.3_{\text{syst}}) \times 10^{-6}$ has been observed [4]. Radio-telescope-based observations on a methanol line yielded, with a similar approach, $\Delta\mu/\mu = (-0.0 \pm 1.0) \times 10^{-7}$ [3]. Matter density dependence has been tested with astrophysical measurements within our galaxy again using methanol lines, yielding $\Delta\mu/\mu = (2.2 \pm 0.4_{\text{stat}} \pm 0.3_{\text{syst}}) \times 10^{-8}$ [43]. Comparing microwave transitions of the methylidyne radical (CH) measured in a lab and in astronomical sources from our galaxy, a variation of the fine structure constant, $\Delta\alpha/\alpha = (0.3 \pm 1.1) \times 10^{-7}$, has been found [69].

A classical technique to produce cold molecular samples are molecular beams. They were first reported in 1911 by Dunoyer [27]. In 1922 with the Stern and Gerlach's experiment [31] they became a consolidated starting point for many scientific experiments. To produce a molecular beam, it is sufficient to let a gas mixture expand from an high-pressure to a low-pressure region through a nozzle. The initial enthalpy of the gas is converted into forward velocity. This process lowers the temperature of the molecules. The mean velocity of the molecular beam depends on the composition of the gas mixture, in particular on the average molecular weight. Typically, molecular beams can have average velocities ranging from 300 to 1000 m/s.

Typical densities in a molecular beam close to the nozzle are in the range of $10^{11}/\text{cm}^3$, decaying with the second power of the distance from the source. The low internal temperature of a few K [50] and the low number of collisions in the sample make molecular beams particularly well suited for spectroscopic experiments.

The speed of a molecular beam mainly depends upon the molar mass of the species in the beam. It is very hard to reduce the beam speed below 300 m/s even by seeding the species of interest in a heavy carrier gas, like xenon. Recently, helium-buffer-gas sources have achieved an initial speed of the order of 150 m/s. With such speeds, the interaction time with the light when doing spectroscopy is accordingly limited, leading to an uncertainty in the measurement known as transit time broadening. Moreover, although Doppler broadening is strongly reduced in a beam, it is still a consistent source of uncertainty for high resolution experiments.

In the Mid-IR, molecular spectra exhibit a complex structure made of a significant number of absorption lines, that correspond to molecular vibrations. This structure is almost unique for every molecule. For this reason, the Mid-IR portion of a molecular spectrum is known as the molecular *fingerprint region*. These lines often correspond to fundamental modes, which means that their linestrenghts are orders of magnitude higher than those we can find in the visible/near IR.

Quantum cascade lasers (QCLs) are available in the range from 4 to 20 µm [46]. In certain spectral ranges W-level output powers have been recorded [45]. These devices generally show MHz-wide free-running linewidth, but a thorough analysis

of their noise properties demonstrated that the intrinsic linewidth of a QCL can be much narrower [11, 7, 6]. Further improvements on the stabilization of chip temperature and current made possible phase locking of a quantum cascade laser at 10 µm to a CO_2 laser stabilized onto a frequency standard: a linewidth of 10 Hz with a reported stability of 10^{-14} at 1s and accuracy of 3×10^{-12} was achieved [66]. To date, the best result in terms of linewidth was achieved by Amy-Klein and co-authors, with a linewidth as stable as 2×10^{-15} and an accuracy of 10^{-14}. They obtained this result transferring the stability and accuracy of the primary frequency standard, coming from a metrological institute, to a QCL through an OFC [2].

A fundamental ingredient that made this result possible is the development of hundreds of km-long fiber links from the national metrological institutes (NMI) like LNE-SYRTE in France, NPL in the UK, AGH in Poland, PTB in Germany and INRIM in Italy, to several laboratories. When referencing local oscillators to quartz-oscillators disciplined by Rb-GPS clocks, the stability is limited to parts in 10^{-13} and the absolute accuracy to 10^{-12} [49]. Fiber link technology allowed for an improvement of several orders of magnitude both in the stability and accuracy of referenced lasers [8].

Ultra-stable optical radiation referenced to the national primary frequency standard is provided to the European Laboratory for Non-linear Spectroscopy (LENS) in Florence by the italian Metrological Institute (INRIM), via a 642 km-long optical fiber link. The optical link actually connects, along its path, several research centers, whose different research fields reflect the wide application range of this facility: from the Institute for Radioastronomy in Medicina (514 km from Turin) to the Space Geodesy Center in Matera (1684 km), passing from the financial district in Milan, the National Institute of Optics in Sesto Fiorentino and Arcetri (around 682 km) and in Pozzuoli (1306 km). The final part of the connection to the Space Geodesy Center in Matera (1684 km) is already in operation and under characterization. At present, the italian fiber link is the longest National link in Europe. Generally, the frequency transfer is obtained with a frequency instability of 3×10^{-19} and an accuracy of 5×10^{-19} over 1000 s [14].

At the beginning of my PhD, I worked at a high-resolution measurement of a vibrational transition on metastable carbon monoxide in the Mid-IR [35]. My contribution to that work is related to the production of Mid-IR radiation by difference frequency generation in an orientation patterned (OP) GaP crystal, to the implementation of the virtual beatnote scheme for the phase lock of the two near-IR lasers, and to the final measurements of the vibrational transition frequency. To introduce the framework in which my work is set and to show how it can bring to important improvements of the precision, I will briefly show here the main results of that measurement.

For this experiment, we produced a molecular beam by expanding a mixture of 20 % CO in Kr at a backing pressure of 2 bar through the nozzle of a pulsed solenoid valve (Parker Hannifin Corp., modified General Valve series 99), which is

kept at 140 K and operates at 10 Hz. After a 1-mm skimmer, the collimated beam has a velocity of 318 m/s. A pulsed UV laser at 206 nm excited CO molecules from the ground state to the $a^3\Pi_1$, $v = 0, J = 1$ metastable state. A Mid-IR laser propagating perpendicular to the molecular beam drove the vibrational transition to the $v = 1, J = 1$ state and finally, the molecules were detected by resonance enhanced multi photon ionization (REMPI). We locked our optical frequency comb to the signal provided by the NMI to refer Mid-IR radiation to the frequency standard.

The stability and robustness of this setup allowed for rapid scans yielding high signal-to-noise ratios. A 25-minutes long scan yielded a Doppler-broadened absorption profile with a FWHM of 900 kHz, as the one shown in 1.1, which is already about two orders of magnitude narrower than the best value reported in the literature [23]. We acquired 22 scans over a few days for a total measurement time of 9 hours. This set of data allows to determine the line center of the chosen vibrational transition on the metastable excited state, 51399115447 ± 3 kHz, with an improvement of the total uncertainty of more than 4 orders of magnitude on ref. [23], the only previous determination. The relative uncertainty of 6×10^{-11} is mainly due to systematic effects that will be discussed more in detail later on.

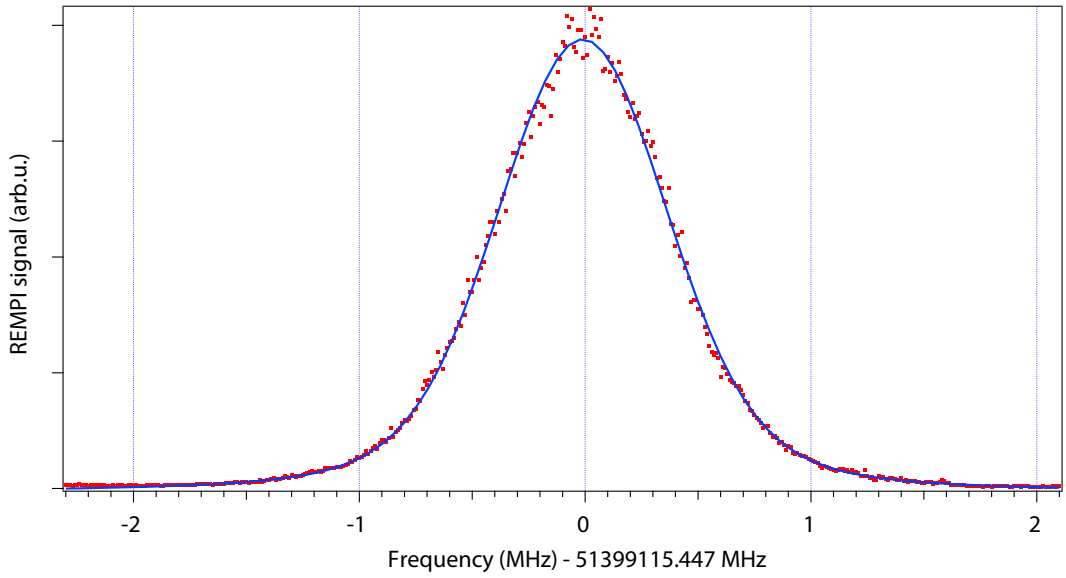

Figure 1.1: Transition $a^3\Pi_1 : v = 0, j = 1, + > \rightarrow v = 1, j = 1, - >$. The blue solid line is a Voigt profile fit of the experimental data (red dots).

While the accuracy is currently limited by fluctuations of the excitation UV laser, as it will be shown in a while, the precision of this absolute measurement is limited by the Doppler broadened line profile. It would be natural to go for an intrinsic Doppler-free spectroscopic measurement but, unfortunately, the spectral

region around 6 µm suffers from a severe lack of optical devices. In particular, the poor quality of optical isolators and the low sensitivity of photodiodes, above all, prevented us from implementing a two photons or a saturated absorption experiment.

To avoid any undesired Doppler shift that would introduce an undesired systematic error in the line center measurement, we retro-reflected the Mid-IR radiation with a a corner cube so that the molecules interacted twice with the QCL radiation that drives the vibrational transition to the $\nu = 1$, J = 1, - state.

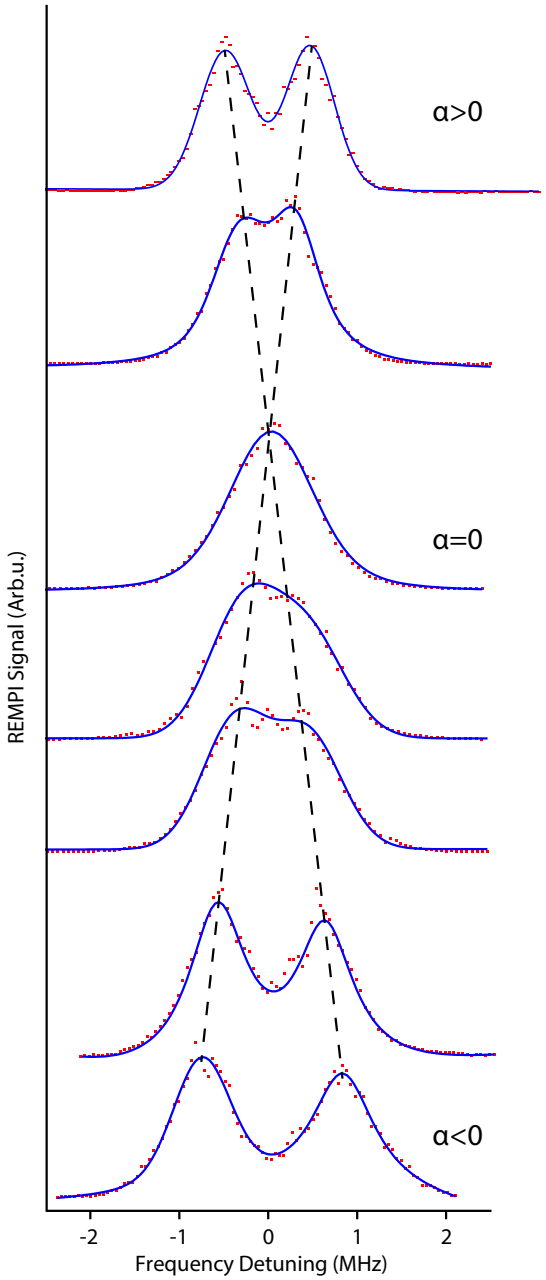

Figure 1.2: Recordings of the vibrational transition measured using both antiparallel beams. The frequency of the Mid-IR laser is scanned while the REMPI signal is recorded. Each point represents an average over multiple acquisition cycles. All fitting curves are double Voigt profiles. The different graphs represent different values of the angle α: from the first to the last graph, the angle was moved from positive to negative sign.

The two anti-parallel laser beams induced Doppler shifts equal in magnitude but

opposite in sign (Figure 1.2). Thus, when the molecular beam and the Mid-IR laser beam were not perpendicular, we observed a symmetric splitting of the absorption line. We recorded the magnitude of the splitting vs. the angle between the laser and the molecular beam, and, finally, we settled at the position corresponding to the minimal splitting. The remaining systematic uncertainty is due to imperfect parallelism of the counter-propagating Mid-IR beams. This has been independently measured by means of a HeNe laser over a distance of 10 m, and it resulted to be better than 10^{-4} rad, which corresponds to a final uncertainty on the transition frequency of 2.6 kHz.

In addition to Doppler shift, Zeeman and Stark effect could induce a frequency shift of the absorption line. While stray electric fields are shielded by the vacuum chamber, the magnetic field was compensated by 3 pairs of coils in a quasi-Helmholtz configuration. Selection rules for the $a^3\Pi_1 : v = 0, j = 1, + > \rightarrow v = 1, j = 1, - >$ CO vibrational transition only allow $\Delta M = 0, \pm 1$. The Zeeman shift of the $\Delta M = \pm 1$ components is of the order of 500 kHz/Gauss, whereas the $\Delta M = 0$ lines are shifted by about 12 kHz/Gauss. By cancelling the Zeeman shift on the $\Delta M = \pm 1$ transitions, we estimate that the residual Zeeman shift on the $\Delta M = 0$ transition is smaller than 1 kHz. We repeated the zeroing procedure several times between the scans and we found no variation of the compensating magnetic field. This contributes to the statistical uncertainty, together with the uncertainty in the alignment of the beams, for which the procedure is described above, and with the fluctuations in the population of metastable CO molecules.

We estimate the Stark and second-order Zeeman shifts due to stray fields to be lower than 10 Hz. Since we prepare and detect the molecules with focused ns-pulse long lasers at precisely-known times and positions, we know the speed of the molecules, 318.5 ± 2 m/s. Thus, we calculate the second-order Doppler shift, +29.4 ± 0.4 Hz, and we subtract it from the measured frequency. The remaining systematic uncertainty is due to the Cs fountain standard accuracy [42] and to fibre link phase slips [17], both smaller than 100 mHz. Therefore, the total systematic uncertainty is estimated as 2.6 kHz.

The distribution of the experimental measurements (Figure 1.3) has a Gaussian shape with a standard deviation of 7.9 kHz. The set of 22 scans yields a total statistical uncertainty of 1.7 kHz. Repeated measurements are not consistent with each other: the main reason for the spread of the experimental data, I believe, is the instability of the excitation UV laser. Energy fluctuations or drifts can affect the number of molecules in the $a^3\Pi_1$ state during each scan. Furthermore, the UV source has 30 MHz residual frequency fluctuations, even if it is long-term stabilized on an iodine cell. This effects can actually induce the fitting routine to erroneously interpret them as a shift of the absorption line center.

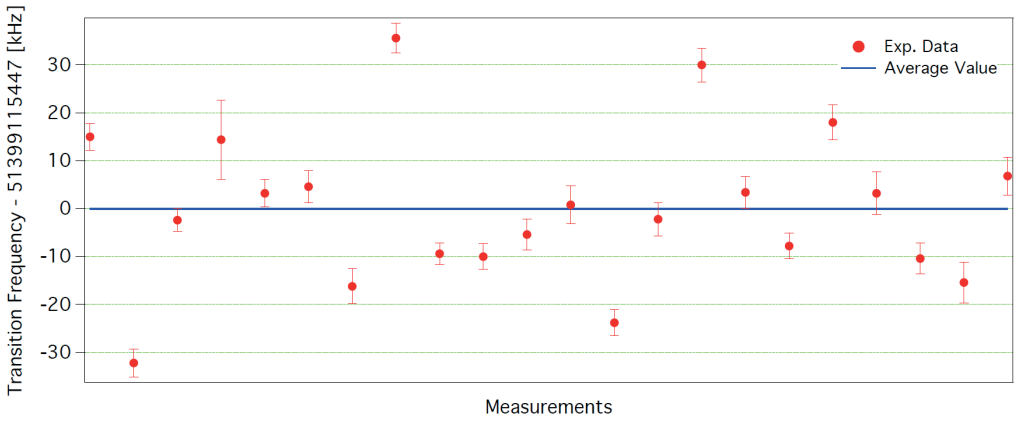

Figure 1.3: Repeated measurements of the transition line center. These independent measurements were taken over a period of a month. The error bar of each point is given by the standard deviation on the line center, coming from each line profile fit. The solid line is the average value, 51399115447 kHz: the standard deviation of this measurement set is 7.9 kHz, while the standard deviation of the mean is 1.7 kHz.

Although we expect the contribution to the line broadening coming from the QCL finite linewidth to be negligible, a direct measurement of the Mid-IR source linewidth is helpful. We will show in the following that in the Mid-IR spectral region, in particular above 5.5 µm, traditional spectral analysis methods are very hard to be implemented. Indeed, each of them presents different problems related to the relative underdevelopment of optical components, e.g. optical isolators. Nonetheless, for all the reasons outlined in the first part of this chapter, the Mid-IR is still a fascinating spectral region for molecular high resolution spectroscopy experiments, and it is worth to make efforts to find some unconventional solution to the source spectral characterization challenge. With this thesis work I have improved the measurement of the transition linewidth by almost one order of magnitude.

Chapter 2

Experimental setup

I would like to remark that part of the work described in this chapter has also been published in [34].

We implemented a setup for high resolution spectroscopy in the Mid-IR on a molecular beam of metastable carbon monoxide. The fundamental of the vibrational transition in the $a^3\Pi$ state of the CO molecule is around 6 µm. The absorption profile is very narrow, having a natural lifetime of 2.63 ms [32].

The optical setup consists, first, of a pulsed UV source that prepares the sample in the metastable state. Then an IR laser drives the vibrational transition, and finally a second UV laser is used for detection via resonance enhanced multi photon ionization (REMPI), that is a state selective measurement. This laser, resonant with an intermediate state, ionizes molecules by a two photon absorption process.

I will give here a detailed description of the molecular beam and the laser setup, paying particular attention to the Mid-IR light source.

2.1 Molecular beam

We produce a molecular beam by pulsing a mixture of 20% CO in Ne into vacuum through a supersonic valve PSV C-211 from R. M. Jordan Co., Inc., with a nozzle diameter of 0.5 mm and a repetition rate of 10 Hz (Figure 2.1). Working at room temperature, this valve is able to provide gas pulses with a nominal duration (FWHM) of tens of microseconds. The gas expands into a vacuum chamber that is kept at a pressure of about 10^{-5} mbar by means of a 520 l/s turbomolecular pump backed by a membrane pump. The molecular beam enters a second chamber through a skimmer with a diameter of 1 mm. Pressure in the second chamber is further lowered to 10^{-7} mbar by means of two 260 l/s turbomolecular pumps backed by the same membrane pump. After the supersonic expansion and the passage through the skimmer, the CO molecules are distributed over the lowest rotational levels of $\nu = 0$ in the ground electronic state and the beam divergence

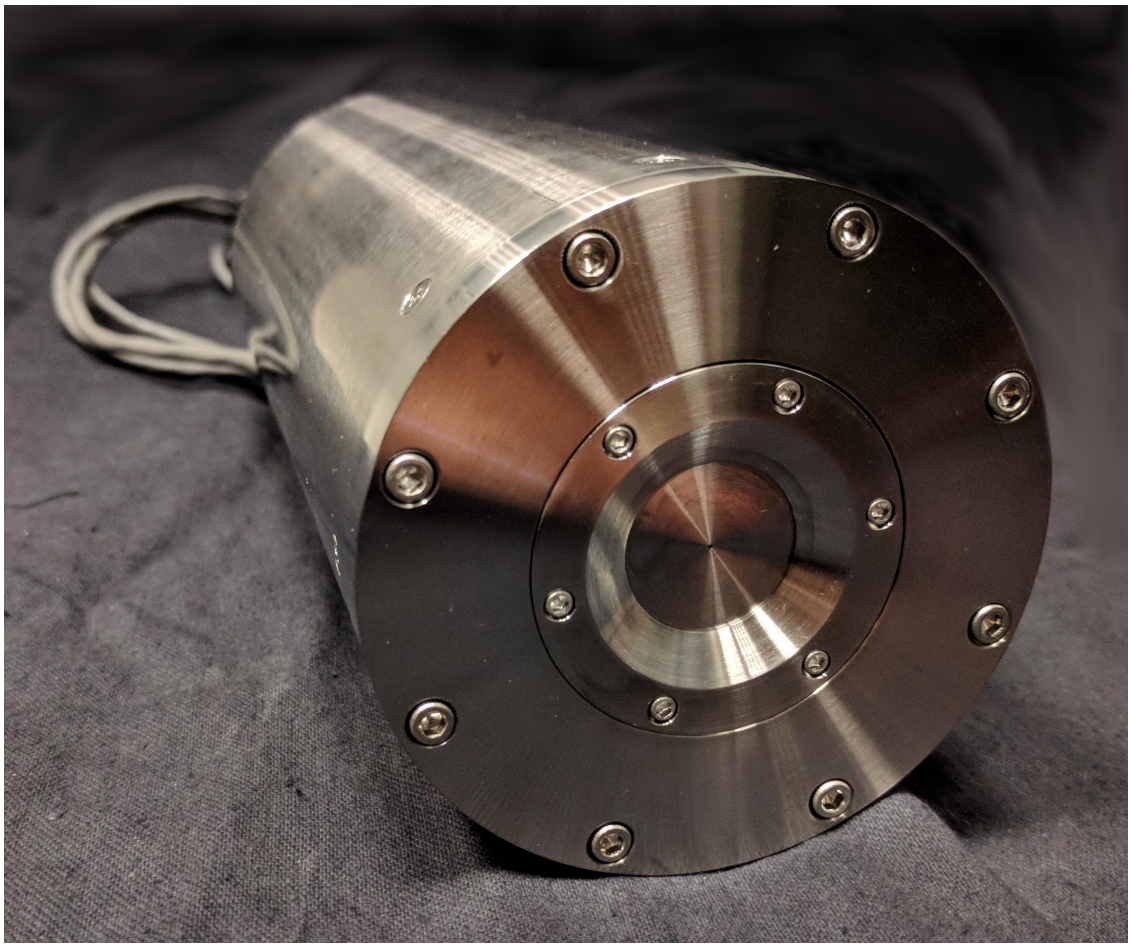

Figure 2.1: C-211 PSV Pulsed Supersonic Valve, from R. M. Jordan Co., Inc. A current pulse of up to 5000 A and 20 µs duration passes in opposite directions in two adjacent conductors, generating a magnetic force that compresses a spring, allowing the gas to pass through the nozzle and expand into the vacuum chamber.

is drastically reduced. The rotational temperature is of a few K. CO molecules are excited from their electronic ground state to the $a^3\Pi_1$, $\nu = 0, J = 1$ metastable state by about 1 mJ of light at 206 nm, produced by a pulsed OPO ($\sim$ 10-ns pulses). The vibrational transition is excited by a QCL emitting at $\sim 6\,\mu$m interacting with molecules in two different configurations: it can either be perpendicular, or quasi-parallel to the molecular beam. In the latter case, the interaction region is $\sim$ 80 mm long, about the center of the second chamber. The Mid-IR laser transfers the molecular population from the $a^3\Pi_1$, $\nu = 0, J = 1$ to the $a^3\Pi_1$, ν=1, J=1 states. Excited molecules are selectively detected with a second ns laser, which ionizes them via the $b^3\Sigma^+$ electronic state in a two-photon process. Ions are generated between two electrodes that accelerate them into a microchannel plate (MCP) detector. The

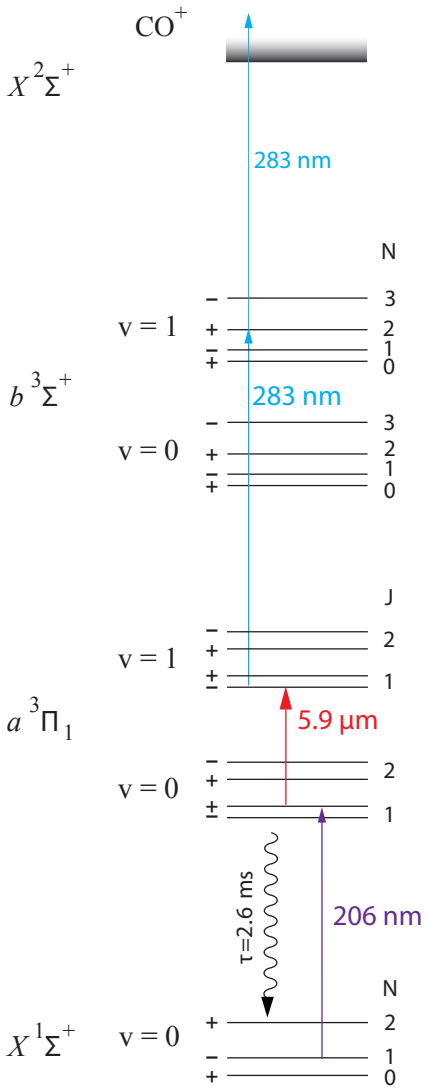

Figure 2.2: Energy level diagram of the involved states of CO. The excitation laser at 206 nm excites molecules from the electronic ground state to the metastable $a^3\Pi_1$: $|v = 0, J = 1, +\rangle$ state. Then, a Mid-IR laser at 5.9 µm drives a vibrational transition, bringing molecules to the $a^3\Pi_1$: $|v = 1, J = 1, -\rangle$ state. Detection occurs via REMPI, thanks to a two photon process induced by a 283 nm pulsed laser that ionizes molecules via the intermediate state $b^3\Sigma^+ : |v = 1, N = 2, +\rangle$.

time of flight detector is oriented along the molecular beam direction (z axis, see Figure 2.3) with a 0.5 mm diameter aperture on the first electrode. The aperture

collimates the molecular beam, selecting only molecules with a narrow velocity spread in the x-y plane.

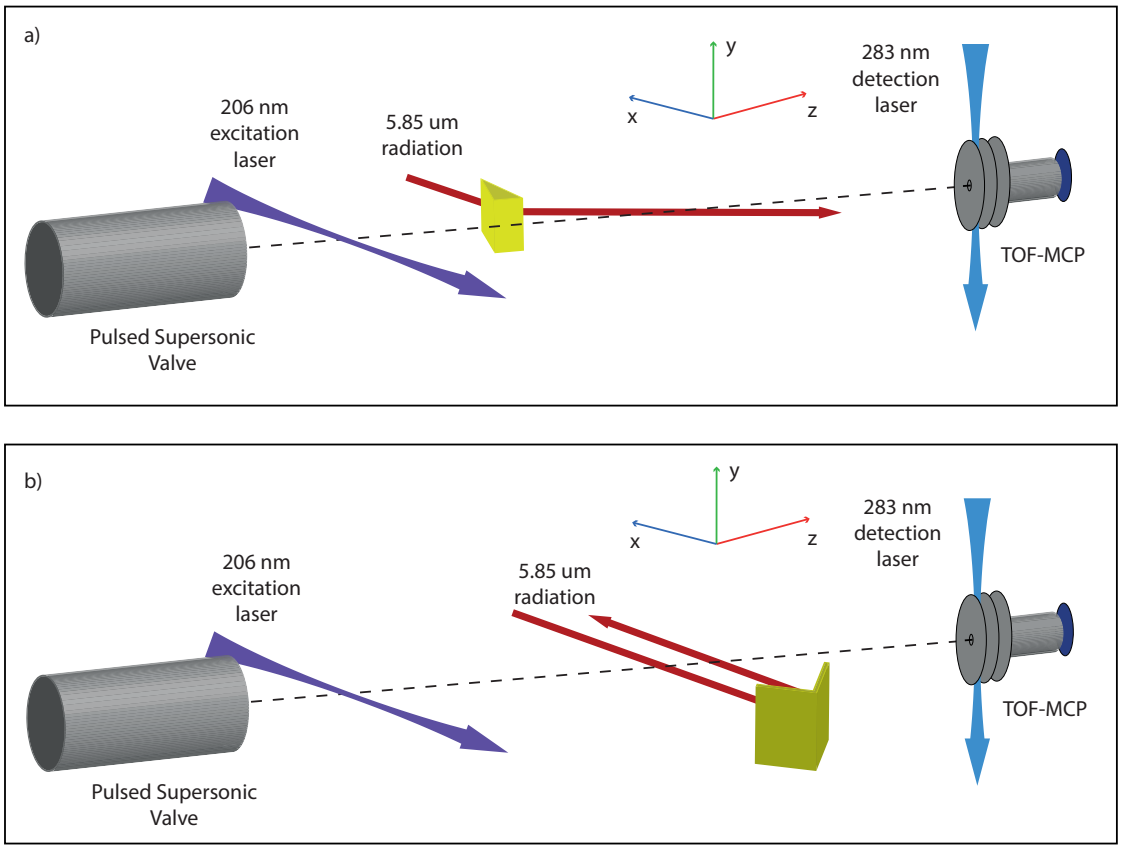

Figure 2.3: A schematic rapresentation of the experiment: a supersonic beam of ground-state CO is produced by pulsing a mixture of CO in neon into vacuum with a Jordan valve operated at 10 Hz repetition rate. The source chamber is separated from the main vacuum chamber by a skimmer with an opening of 1 mm in diameter. After the skimmer, CO molecules are excited to the $a^3\Pi_1$, $v = 0, J = 1$ metastable state by about 1 mJ of light at 206 nm. In the middle of the main vacuum chamber, the molecules interact with the Mid-IR light. The Mid-IR beam and the molecular beam can be a) overlapped under an angle of 0.054 rad ($\sim$ 3 degrees) or b) perpendicular each other. Finally, the molecules are detected with a second ns laser, which ionizes them selectively in a two-photon process. Ions are generated between two electrodes that accelerate them on a microchannel plate detector. Both pulsed lasers intersect the molecular beam perpendicularly.

2.2 Excitation laser

To transfer the population from the electronic ground state to the metastable $a^3\Pi_1$, $v = 0, J = 1$ state, we excite molecules with a 206 nm, 10 ns duration, laser pulse. We use the green light of a frequency doubled 5 ns pulsed Nd:YAG laser at 532 nm (Spectra Physics, Quanta Ray Pro-230) with 10 Hz repetition rate. A beam splitter sends 20% of this light to a BBO crystal that doubles the frequency generating pulses at 266 nm. The remaining part pumps an OPO: in a 4-mirror cavity two KTP crystals produce signal radiation at 917 nm and at 1267 nm. Only the shorter wavelength is resonant with the cavity. The OPO cavity is seeded by a 917 nm cw diode laser (Toptica Photonics AG, DL 100 PRO) to control the generated radiation frequency and to stabilize the cavity length. A small periodic modulation is applied to the piezo on which one of the four mirrors is mounted, providing an error signal for a lock-in amplifier. The lock-in determines the deviation from the resonance and a feedback signal is sent to the piezo to tune the cavity length on a multiple of the seeding wavelength. 917 nm and 266 nm wavelength pulses are then overlapped onto a second BBO crystal to generate sum frequency radiation. The whole system produces up to 2 mJ, 10 ns UV pulses, with 206 nm wavelength and 150 MHz bandwidth.

While 917 nm radiation is frequency stabilized thanks to the seeded OPO cavity, 266 nm radiation is directly affected by frequency fluctuations from the Nd:YAG pump. Therefore, part of the 532-nm radiation is sent to a temperature controlled iodine cell. Absorption is measured with a differential photodiodes scheme and the laser is locked to the side of the I_2 transition centered at 18789.289 cm^{-1}

2.3 Detection laser

Excited molecules are detected via Resonance-Enhanced Multiphoton Ionization (REMPI). This technique consists in ionizing molecules with a multi photon process, in which at least one step is resonant with an intermediate state. We use a tunable pulsed dye laser (NarrowScan, Radiant Dyes Laser & Accessories GmbH). Two cuvettes with a solution of Fluorescine 27 in methanol are pumped by a frequency doubled Nd:YAG 10 Hz pump laser (InnoLas Photonics GmbH, SpitLight 1200) at 532 nm. A grating allows to finely tune the emission frequency, which has a linewidth of the order of 0.03 cm^{-1}. The emission spectrum of Fluorescine 27 ranges from 541 to 571 nm; this radiation is then frequency doubled with a BBO crystal. In our detection scheme we ionize molecules via a two-photon process, enhanced by the transition $a^3\Pi_1 : |v = 1, J = 1, - > \rightarrow b^3\Sigma^+ : |v = 1, N = 2, + >$ (Figure 2.2). The laser wavelength, after frequency doubling in BBO, is 278.9 nm.

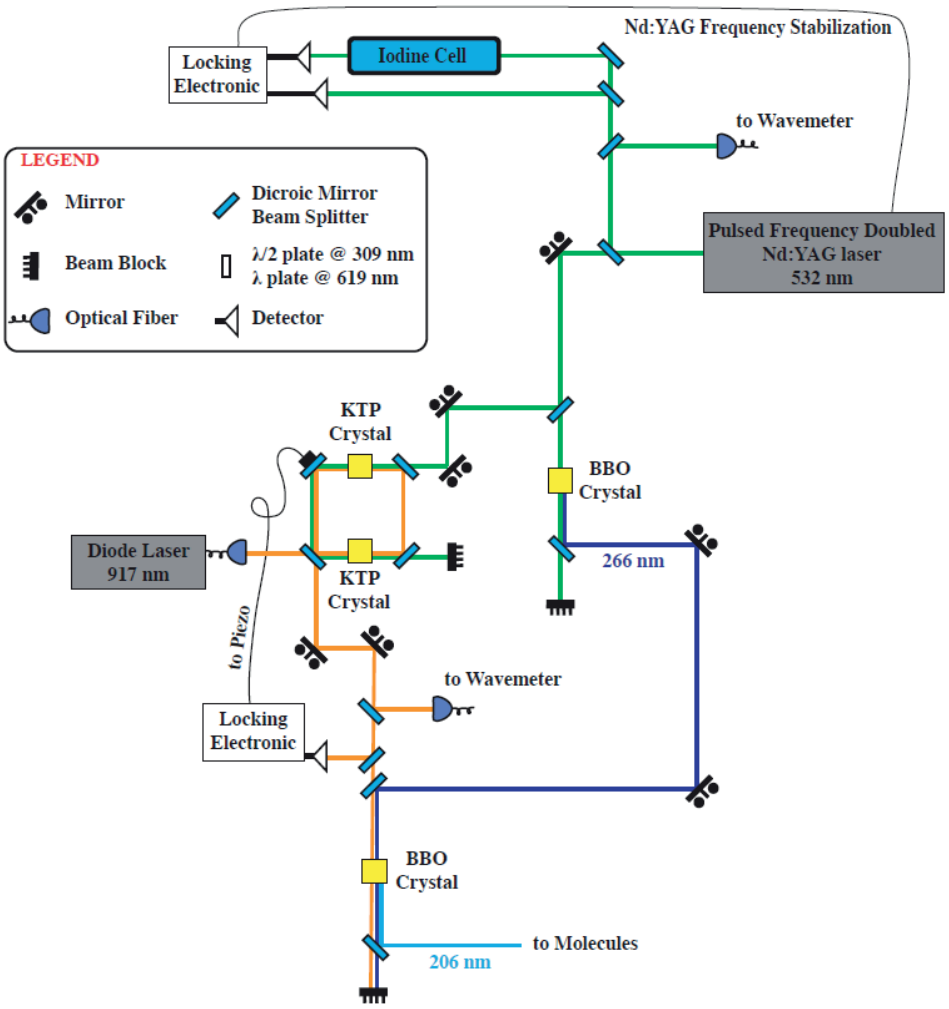

Figure 2.4: Experimental setup for the production of 206 nm radiation. Our source is a frequency doubled Nd:YAG pulsed source. Frequency is stabilized onto an iodine absorption line, and the output power is split in two arms. A BBO crystal doubles the frequency to produce up to $\sim$ 5 mJ of 266 nm wavelength radiation, while in the other arm an OPO produces tens of mJ of radiation at 917 nm. In a second BBO crystal sum frequency generation from radiation at 266 nm and 917 nm produces up to 2 mJ UV pulses at 206 nm.

2.4 Mid-IR frequency generation in OP-GaP

2.4.1 Quasi-Phase-Matching and Orientation-Patterned crystals

Continuous-wave (cw) optical parametric oscillators (OPOs) combine single-frequency and powerful emission [60]. However, cw OPOs have only been demonstrated at wavelengths below 5 µm, where oxide birefringent materials ($LiNbO_3$, $KTiOPO_4$...) are transparent. Non-oxide materials, such as $AgGaSe_2$, $LiInSe_2$, and $CdSiP_2$ [53], show a larger residual absorption loss compared to oxide materials and, therefore, only with silver gallium sulfide ($AgGaS_2$) genuine cw emission could be demonstrated at 2.5 µm [26].

An alternative method to produce narrow-linewidth, widely tunable, μW to mW level Mid-IR coherent radiation, is difference frequency generation (DFG). Yet again, commercial birefringent crystals such as $LiNbO_3$ and $LiTaO_3$ are transparent only below 5 µm. For longer wavelengths, phased-matched DFG suffer from spatial walk-off, which dramatically reduces the nonlinear interaction length. Nonetheless, usual DFG-based phase matching techniques can only be used in anisotropic crystals. Moreover, several isotropic materials exhibit large values of the d-coefficient, little absorption in the Mid-IR and other desirable properties, if compared to the anisotropic ones.

III-V compound semiconductors such as GaAs and GaP belong to the cubic crystal system. They do not exibit birefringence so that, to satisfy the total momentum conservation *quasi-phase-matching* is necessary. A periodic structure in the nonlinear medium gives an additional momentum contribution, so that total momentum is conserved and there is a positive net flow from the pump to the signal and idler. We will address here the three waves involved in the nonlinear process as pump, signal and idler beam for the shorter, middle and longer wavelength, respectively. As long as the phase between the pump and the signal is less than π, energy flows from the first to the second beam. When the phase difference exceeds π, energy starts to flow back from the signal to the pump. The length over which this happens is said coherence length. In a quasi-phase-matched structure the crystal axes are flipped at any coherence length, so that energy continues to flow from the pump to the signal beam, in principle, along the entire crystal length. Note that the involved beams can in principle have the same polarization and can travel through the crystal in arbitrary directions, including collinear propagation: this makes DFG in quasi-phase-matched crystals free from spatial walk-off, a severe limit for DFG over birefringence phased-matched crystals.

Hydride vapor phase epitaxy (HVPE) is the most reliable technique to grow a GaP crystal with orientation-patterned layers: starting from a GaP substrate of 100 nm, a silicon layer of 5 nm is grown. Then, after a smoothing layer of AlGaP, a layer of inverted GaP is grown. This layer is patterned with photolithography,

and then all the grown layers are etched away until the first GaP layer is exposed. The crystal is then first grown in a molecular beam epitaxy chamber (MBE) for 200 nm, then grown until a thickness of few hundred of microns is achieved with HVPE. Crystals with a grating period of few tens of microns can be grown with such a method.

2.5 6 µm DF generated radiation in OP-GaP

We used a single-frequency Nd:YAG laser (λp = 1064.5 nm, Mephisto MOPA, Coherent Inc, $\Delta\nu$ ∼10 kHz, hereafter called "pump") and an extended-cavity tunable diode laser (λs = 1301.1 nm, DL 100, Toptica Photonics AG, $\Delta\nu \sim$ 100 kHz, hereafter called "signal"). Up to 65 µW of single-frequency idler at λi = 5.85 µm were generated from ∼10 W of pump and ∼40 mW of signal in a QPM OP-GaP crystal. An OP-GaP crystal with length l_c = 24.6 mm and antireflection coated at the three wavelengths on both facets (reflections at the three wavelengths is below 1%) was characterized. We received this custom crystal from a collaboration with BAE Systems, Inc. The crystal carries a 400 µm thick melt-grown substrate, over which the OP layer extends for an additional 400 µm thickness. The overall thickness of the chip is ∼ 1.5 mm, with a ∼ 6 mm wide OP layer carrying a 50% duty cycle periodic domain reversal (grating period Λ = 24 µm). The sample is housed in a massive copper block oven whose temperature is regulated by a P-I servo-controller, and the oven is mounted on a $XYZ - \Theta\Phi$ positioner for DFG efficiency optimization. The phase-matching temperature was found to be around T= 43°C.

An effective first-order QPM nonlinear coefficient $d = (2/\pi)d_14 = 17(3)$ pm/V has been evaluated from the absolute measurement of DFG conversion efficiency versus focusing, and these results are in agreement with the cw Gaussian beam DFG theory (DFG setup is shown in Figure 2.5). The pump and signal laser beams are nearly TEM_{00}. They are coaxially focused in the OP-GaP crystal using a lens, L1, with a focal length of 50 mm. A variable telescope on the pump path allows to match the beam waist of the pump to that of the signal and to superimpose the two waists inside the crystal longitudinally during idler power optimization. After the crystal, the idler beam is separated from the near-IR pump and signal beams, using a coated Ge window, and refocused onto a thermo-electrically cooled HgCdTe photodetector (VIGO system, PVI-4TE-5/ MIP-DC-10M) using a couple of lenses, L2 and L3, with 50 mm focal length. The detector absolute responsivity was calibrated by simultaneously measuring the power of a QCL at 5.85 µm in a range ∼ 2 - 70 µW with a calibrated radiometer. Figure 2.6 displays the absolute Mid-IR power generated just after the crystal as a function of the pump power, for a fixed signal wave power $P_s \sim$ 40 mW. Each curve corresponds to a focusing condition, i.e., to a value of the focusing lens L1. The maximum idler power $P_i \sim$

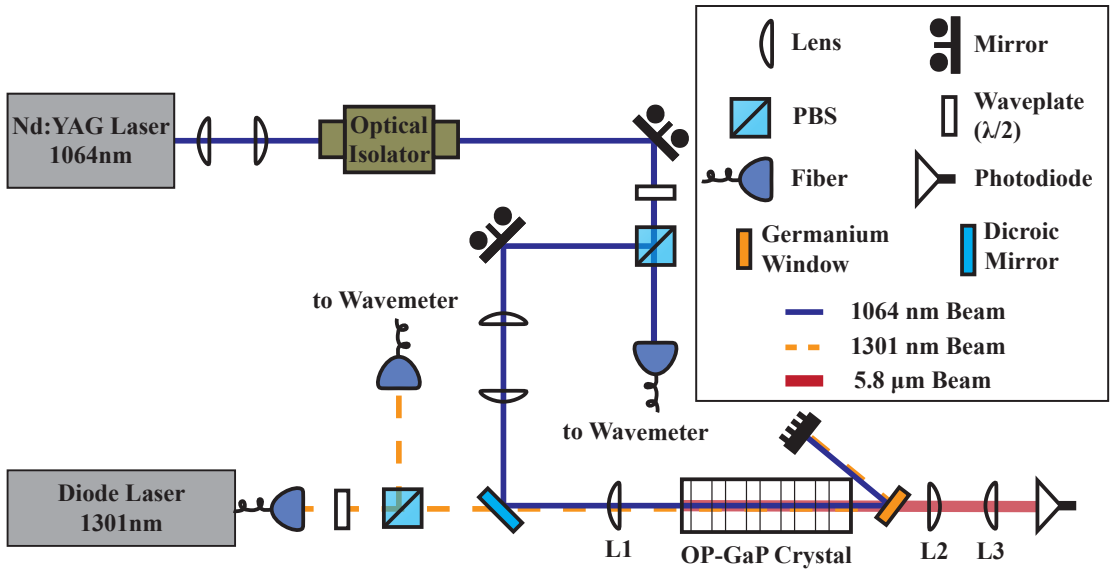

Figure 2.5: Experimental DFG laser setup. After the Ge window, L2 (f_0 50 mm) collects the idler, and L3 focuses it on the 200 µm active area of the HgCdTe detector. L2 and L3 are made of CaF_2.

65 µW is generated at $P_p \sim 10$ W at the strongest focusing (f = 50 mm), although the curve for f = 75 mm almost overlaps the f = 50 mm curve, meaning that these focal lengths must be around the optimum to saturate the DFG efficiency. The limited transparency of GaP at 1064 nm results in the heating of the crystal; the thermo-optic effect consequently changes the refractive index, affecting the QPM conditions. This is then responsible for two observed effects. First, at the largest powers, the pump beam heats the crystal by several degrees above the oven temperature, shifting the crystal temperature out of the QPM condition. In our measurements, we took into account this process by adjusting the oven temperature, so that each data point in Figure 2.6 corresponds to the optimal QPM condition, once thermal equilibrium is reached. Second, the finite thermal conductivity of GaP yields a transverse temperature gradient. This affects the QPM condition in a spatial-dependent fashion. While the QPM condition is well satisfied for weak pump powers, for substantial thermal load it cannot be satisfied throughout the whole beam volume. This accounts for the observed idler power saturation at larger pump powers, whereas a linear behavior would be expected from the Gaussian beam DFG theory, with slope $\Lambda P_i/(P_p P_s)$, known as the conversion efficiency [73]. The linear efficiency saturation observed for the two strong focusing data can be related to the limited thickness (400 µm) of the patterned layer. Indeed, the far-field divergence angle of each wave is $\delta = \lambda/\pi n \omega_0$. For the pump and signal, one finds that in all four focusing configurations, the beams are well inside the patterned layer over the whole length of the crystal. However, due to its longer wavelength, this is not the

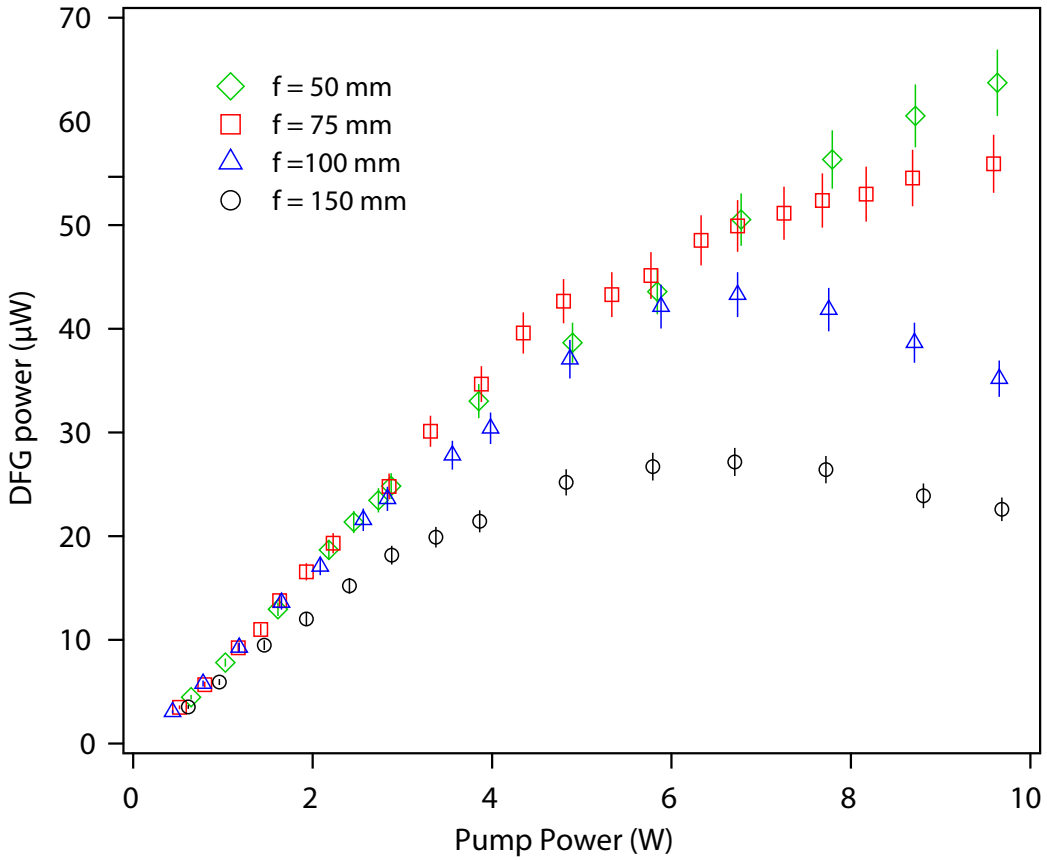

Figure 2.6: Mid-IR radiation generated as a function of the pump power, for different values of the focusing lens L1.

case for the idler wave, having a mean diameter at the output facet evaluated to be 980 and 686 µm with f = 50 and 75 mm, respectively. For the two looser focusing cases, instead, the idler mode diameter remains within the 400 µm thickness of the patterned layer. Thus, for strong focusing, part of the generated idler expands outside the OP layer into the bulk region where the absorption is larger and QPM is no longer satisfied. Consequently the difference between the idler's phase and the sum phase of the pump and signal is not strictly identical within and outside the QPM layer, thus affecting the overall phase coherence of the DFG process along the crystal at strong focusing compared to the looser focusing cases where all three waves remain quasi-phase-matched over the whole crystal length. The way strong focusing affects saturation of the generated DFG power could be checked by using a sample with identical length, but with a thicker OP layer (e.g., 1000 µm).

In order to boost the Mid-IR power, a temperature stabilized quantum cascade laser (Alpes Lasers SA) is phase-locked to the DFG light and used for the spectroscopic measurement. The laser output is split in two beams: more than 90% of

the total power is collimated by means of a pair of positive lenses and sent towards the molecular beam. The remaining power, few tenths of mW, is combined in a non polarizing beam splitter with the radiation coming from the OP-GaP crystal: the resulting beat note is detected by a thermo-electric cooled HgCdTe photodiode. Such a signal is used to feed a PLL that stabilizes the QCL by modulating its current with a bandwidth of 300 kHz.

2.6 Locking chain

In this section we describe the locking chain that links the Mid-IR radiation, generated in the OP-GaP crystal, to the primary frequency standard provided from the Italian National Metrological Institute (INRIM) over a 642-km-long optical fibre link. We obtain Mid-IR radiation with an estimated linewidth of few kHz over 1 ms timescale, a long term stability (1×10^{-14} at 1 s) and accuracy (2×10^{-16} over the same timescale) that reflects reliably the performance of the Cs fountain at the basis of the frequency chain.

2.6.1 Optical frequency standard

Our optical reference at 1542 nm is a fibre laser in Torino whose frequency is kept at 194.399996 THz by a dual lock scheme: a fast Pound-Drever-Hall lock (bandwidth $>$ 60 kHz) to a high-finesse Fabry–Perot cavity [18] and a slow phase–lock (25 mHz bandwidth) to a hydrogen maser using an optical frequency comb, to correct for the cavity long-term instability. The stability of this laser is 3×10^{-15} at 1 s. Periodic comparisons of the hydrogen maser with a cryogenic Cs fountain primary frequency standard ensures that the frequency of the 1542-nm laser is known with an accuracy of 2×10^{-16} [42]. This optical signal is sent to the laboratory at LENS via a 642-km-long fiber link, where 9 bidirectional erbium-doped fibre amplifiers have been installed to partly compensate for the 190-dB optical losses [14]. The optical phase is stabilized using the Doppler noise cancellation scheme (see Ref. [71]). At LENS, a diode laser is phase-locked to the incoming radiation on a bandwidth of 100 kHz, boosting the optical power at a suitable level for referencing a local frequency comb. A complete metrological characterization of the fiber-delivered frequency signal can be found in Ref. [17]. While GPS dissemination limits the typical fractional frequency uncertainty to 10^{-13} on a day average [44], frequency dissemination by fiber link allows to achieve a short-term Allan deviation of 1 $\times10^{-14}$ at 1 s and an ultimate accuracy on the frequency transfer of 5 $\times10^{-19}$ at 1000 s integration time [17].

2.6.2 Optical frequency Comb

We transfer the stability and accuracy of the frequency standard to the Mid-IR using a commercial optical frequency comb (OFC) working between 1 and 2 µm. It can either be stabilized against the ultrastable optical reference at 1542 nm coming from INRIM, in Turin, or against a RF reference at 10 MHz. This reference is provided by a Rb/GPS-disciplined quartz clock as stable as 6×10^{-13} and having an accuracy of 2×10^{-12} at 1 s.

When the the optical signal is used as reference (Figure 2.7), the repetition rate frequency f_{rep} of the OFC is phase-locked to the 1542-nm light using an intra-cavity electro-optic modulator. The achieved locking bandwidth is approximately 300 kHz, and the lock frequency is properly chosen so that the repetition rate is 100 MHz when the incoming radiation is at the nominal frequency value. The carrier-envelope offset frequency f_0 is stabilized at a value of 20 MHz to a RF frequency standard. The phase noise of the optical comb is limited by the optical reference that is delivered over the fiber link. In particular, in the acoustic region the fiber-induced phase noise is not completely suppressed due to the limited bandwidth of the Doppler noise cancellation loop. In fact, this is inversely proportional to the round-trip time of the light in the fiber [71] and it amounts to about 40 Hz in our link [14].

2.6.3 Near IR lasers phase lock

The power for each comb tooth is of the order of 100 nW, on average. We split the comb output into two arms to measure the beatnotes with the pump and the signal lasers. For this, we use a dichroic mirror that separates the two spectral regions with over 95% efficiency. For a good SNR on the detector, collimation of the laser beam is important. To minimize power losses, we use a telescope on the comb beam before the dichroic mirror, although the refraction index difference at the two frequencies yields an imperfect collimation. We isolate the teeth needed for each beatnote using two gratings mounted in Littrow configuration, followed by apertures to further improve selectivity.

The PLL electronics we developed requires the SNR of the input RF to be better than 30 dB in 100 kHz bandwidth. Tweeking of the OFC amplifier yields SNR of the order of 25-30 dB. By measuring each beatnote with two InGaAs photodiodes used in differential configuration, we improve the SNR by about 10 dB, reaching a best-case condition of 40 dB SNR in 100 kHz bandwidth.

The diode laser is phase-locked to the pump to stabilize the difference frequency $\nu_{\mathrm{DF}} = \nu_{\mathrm{pump}} - \nu_{\mathrm{signal}}$, where ν_{pump} and ν_{signal} are the absolute frequencies of the two lasers. Here and in the following we use ν for optical frequencies and f for radiofrequencies. The frequency difference between the two lasers is bridged using the OFC as transfer oscillator, with the so-called *virtual beatnote* scheme [68, 30].

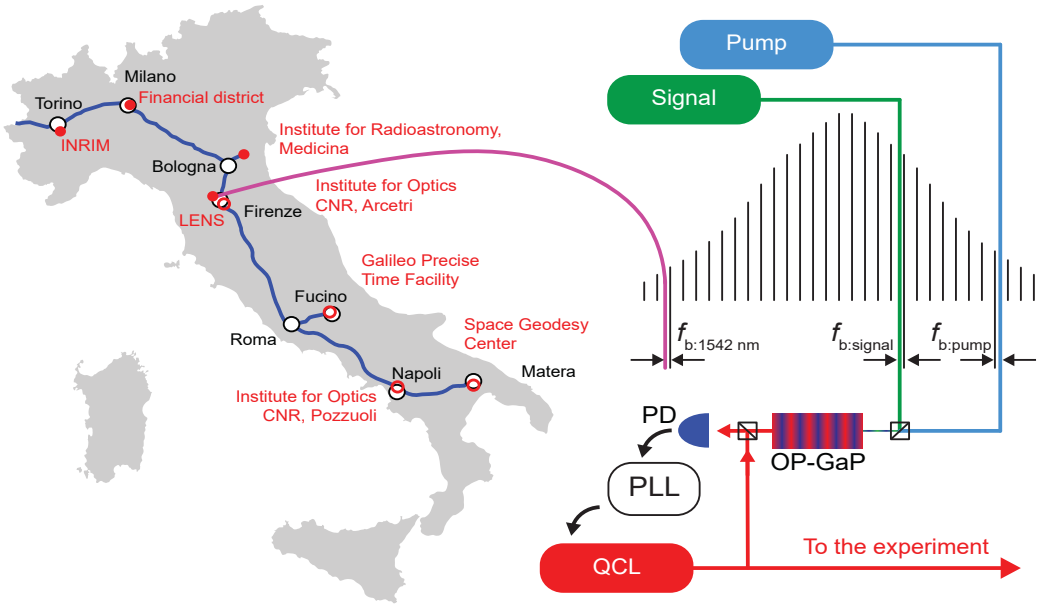

Figure 2.7: Metrological grade 6 µm radiation: a reference laser at 1542 nm is sent from the National Institute for Metrological Research in Torino to our laboratory at LENS, via a 642-km-long fiber link. Optical losses are compensated and the fiber-induced phase noise is suppressed with a Doppler noise cancellation scheme. At LENS this signal is used to reference an optical frequency comb, that is used to reference the pump and the signal diode lasers. An OP-GaP crystal produces up to 70 µW of Mid-IR radiation at 6 µW. This tiny amount of radiation is enough to phase-lock a quantum cascade laser emitting in the same spectral region, so that the linewidth is strongly narrowed and the frequency results directly referred to a primary frequency standard.

An overview of the experimental setup is shown in Figure 2.8.

In figure 2.9 some typical recordings of the beat notes between different lasers are shown. The plot (a) shows the beat note between the comb and the regenerated reference light at 1542 nm. A PLL stabilizes the beat note frequency at 64 MHz to maintain the repetition rate of our comb at 100 MHz. Panel (b) shows the beat note between a comb tooth and the 1064 nm laser. In this case, the beat note is stabilized at 130 MHz and it is broad because of the low locking bandwidth of about 500 Hz. On graphs (c) and (d) the virtual beat note between the 1064 nm and the 1300 nm laser and the beat note between the QCL and the DFG radiation

are shown. The smoothed sidebands around the carrier correspond to the servo bumps. From these we infer a locking bandwidth of 300 kHz in (a) and (d) and 200 kHz in (c). In (b) the servo bumps are not visible because of the limited resolution bandwidth and the loose locking of the pump laser to the comb.

2.6.4 The virtual beatnote method

This procedure is thoroughly described in Ref. [68] and is a well-established method in many laboratories. For a more intuitive understanding, we can first think of a simplified case in which the DF of two lasers is locked using a comb whose f_{rep} is perfectly fixed. The free parameters in this case are the frequencies of the two lasers, ν_{pump} and ν_{signal}, and the comb's offset f_0. Since the DF is assumed to be too large to be counted directly, each laser is beaten against the closest tooth of the OFC, n_{pump} and n_{signal}, yielding $f_{\text{b:pump}} = n_{\text{pump}} f_{\text{rep}} + f_0 - \nu_{\text{pump}}$ and $f_{\text{b:signal}} = n_{\text{signal}} f_{\text{rep}} + f_0 - \nu_{\text{signal}}$, and a PLL keeps the difference

$$f_{\text{b:pump}} - f_{\text{b:signal}} = f_{\text{rep}}(n_{\text{pump}} - n_{\text{signal}}) - (\nu_{\text{pump}} - \nu_{\text{signal}}) \tag{2.1}$$

constant by acting on the frequency of either laser, say the signal. In our setup we beat the pump and the signal laser respectively with the teeth $n_{\text{pump}} = 2816363$ and $n_{\text{signal}} = 2302371$. We note that the value $f_{\text{b:pump}} - f_{\text{b:signal}}$ is all the PLL needs, whereas knowledge of which of the free parameters is drifting is irrelevant. Thus, the pump could in principle run unlock but this is unpractical, since the photodiodes and the filters have a limited bandwidth. Further, to avoid unnecessary action on the pump's driver to follow instabilities in f_0, the frequency is usually locked using $\overline{f}_{\text{b:pump}}$, defined as $\overline{f}_{\text{b:pump}} = f_{\text{b:pump}} + f_0$. Once $\overline{f}_{\text{b:pump}}$ has been generated with an analog mixer, the same can be done for the signal and the DF for the PLL is thus generated as $\overline{f}_{\text{b:pump}} - \overline{f}_{\text{b:signal}}$, which is identical to equation (2.1).

If a real OFC is used instead, where the stability of f_{rep} is finite, one immediately sees from equation (2.1) that the difference of the beat-notes is not a good signal for the PLL because the term $f_{\text{rep}}(n_{\text{pump}} - n_{\text{signal}})$ is not constant anymore. A conceptual difficulty arises by the fact that a variation of $\overline{f}_{\text{b:pump}} - \overline{f}_{\text{b:signal}}$ could either be due to a drift in the pump's or signal's frequency, or to a drift of f_{rep}. The appropriate correction to apply to the signal's frequency to keep DF constant would be a shift of equal size in the first case, but a shift scaled by $n_{\text{signal}}/n_{\text{pump}}$ in the latter case, because of the stretchable-ribbon-like behavior of OFCs. A simple solution is available if the pump has a good short-term stability and can thus be loosely locked to a comb's tooth. Then, the PLL for the signal can be closed on

$$\overline{f}_{\text{b:signal}} - \frac{n_{\text{signal}}}{n_{\text{pump}}} \overline{f}_{\text{b:pump}} \tag{2.2}$$

with a much tighter lock, i.e with a wider bandwidth. In our setup this signal is generated with a 32-bit Direct Digital Synthesizer (DDS) and a mixer, and is

used as the error signal for the phase–lock loop (PLL) of the diode laser with a bandwidth exceeding 200 kHz. An overview of the electronics used for the virtual beatnote scheme is shown in Figure 2.10.

Once all the lasers are properly locked, the stability of the DF radiation depends on that of the pump laser. Indeed, according to the DDS technique, the difference frequency is given by

$$\nu_{\mathrm{DF}} = \nu_{\mathrm{pump}} - \nu_{\mathrm{signal}} = (1 - \frac{n_{\mathrm{signal}}}{n_{\mathrm{pump}}})\ \nu_{\mathrm{pump}} \tag{2.3}$$

The phase noise power spectral density (PNPSD) of the DF, $\mathrm{PNPSD}_{\mathrm{DF}}$, is expected to reproduce that of the pump rescaled by the factor $(1-\frac{n_{\mathrm{signal}}}{n_{\mathrm{pump}}})^2$, which in our case is $\simeq 0.033$, according to

$$\mathrm{PNPSD}_{\mathrm{DF}} = (1 - \frac{n_{\mathrm{signal}}}{n_{\mathrm{pump}}})^2\ \mathrm{PNPSD}_{\mathrm{pump}} \tag{2.4}$$

For further details regarding PNPSD and laser linewidth, please refer to the Section 3.

2.6.5 DF linewidth estimation

According to equation (2.4), the DF phase noise can be estimated from the PNPSD of the pump. Figure 2.11 shows the pump PNPSD (green trace) and the expected phase noise of the DF radiation (red trace). For frequencies above 15 kHz the DF noise is dominated by the background due to electronic noise (thinner red trace). In the inset, the DF radiation frequency noise PSD is also shown. Laser phase and frequency noise will be described more in details in the following (section 3). From a numerical integration of the frequency noise PSD according to [28], we calculate a linewidth of 2.3 kHz (FWHM over 1 second timescale) for the DF radiation. This is expected to match the linewidth of the QCL when locked to the DF light. In the figure, the phase noise of the free-running QCL is also shown for comparison (black trace). In the former analysis we have assumed that the phaselock loops are driven by a zero-noise frequency reference. In reality, all the PLL and local oscillators used in the locking chain are referenced to a local GPS-disciplined rubidium-based reference that has a relative instability of $\delta\nu_{10\,\mathrm{MHz}} \sim 1 \times 10^{-12}$. Taking into account all the different elements referred to this local oscillator, we can calculate a contribution to the final instability of the Mid-IR radiation of few parts in 10^{-18}, which is negligible with respect to the instability of the optical link.

2.6.6 QCL-DFG phase lock effectiveness

To evaluate the effectiveness of a phase lock, a commonly measured quantity is the parameter η. Given a beatnote with a power spectrum $\mathrm{P}(\nu)$ centered around

the carrier frequency ν_0, η is defined as the fraction

$$\eta = \frac{P(\nu_0)}{\int_{-\infty}^{+\infty} P(\nu - \nu_0)\, d\nu}. \tag{2.5}$$

η is commonly used as a figure of merit for the for the phase lock [56]. If $\Delta\phi$ is the loop phase error, we denote the ensemble or time average as $\langle\rangle$ and the root mean square as $\langle\Delta\phi^2\rangle$. If $\langle\Delta\phi^2\rangle \ll 1$, then

$$\eta = e^{-\langle\Delta\phi^2\rangle}. \tag{2.6}$$

From a numerical integration of the different portions of the spectrum of the beatnote between QCL and DF radiation shown in Figure 2.12, we obtain $\eta = 0.7$, so we can assess that about 70% of the QCL power is channelled into the DF mode. This value is in line with those we achieved with locked QCLs in previous works with different electronic locking schemes [15, 29]. In this condition, we expect that the QCL absolute frequency is determined with the same accuracy as the DF radiation, and that its linewidth does not deviate significantly from that of the DF light.

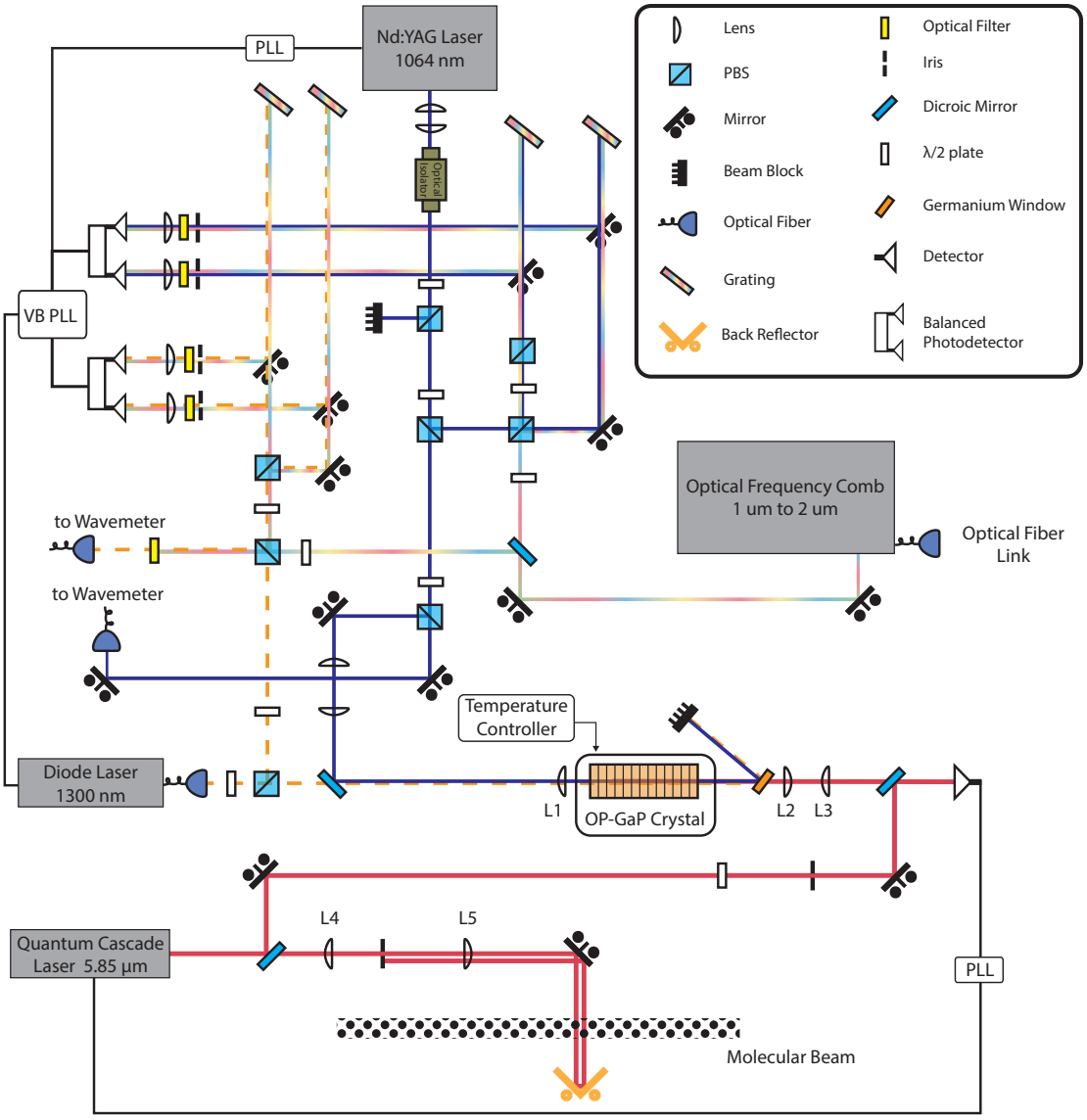

Figure 2.8: An overview of the experimental setup. The difference of the frequencies of two lasers, one at 1064 nm (pump) and the other at 1301 nm (signal), is kept fixed by locking both lasers to the OFC, and radiation at the difference frequency (DF), i.e. around 5.8 µm, is generated in a 24.6-mm long OP-GaP crystal. This radiation is used to lock the frequency of a room-temperature DFB-QCL that delivers up to 35 mW of Mid-IR light. The beat-note is produced on a thermo-electric cooled HgCdTe photodiode with a bandwidth of tens of MHz. Such a signal is used to feed a PLL that stabilizes the QCL by modulating its current with a bandwidth of 300 kHz.

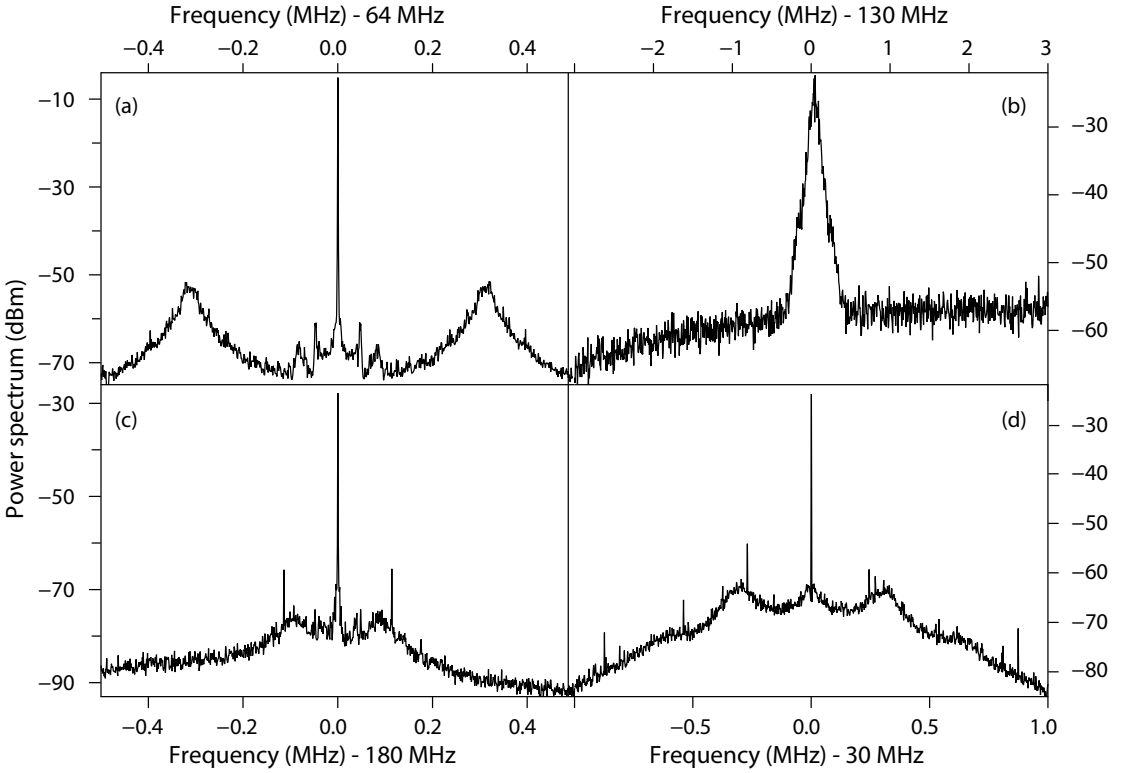

Figure 2.9: Beat notes of the different phase-lock loops acquired by means of a spectrum analyzer. (a): beat note between the comb and the reference laser at 1542 nm. Beat note between comb and pump (b) and between virtual beat note and signal (c). (d): beat note between the generated DFG and the QCL. All spectra are acquired with 10 Hz resolution bandwidth, except the data shown in (b) for which the resolution bandwidth is 300 Hz.

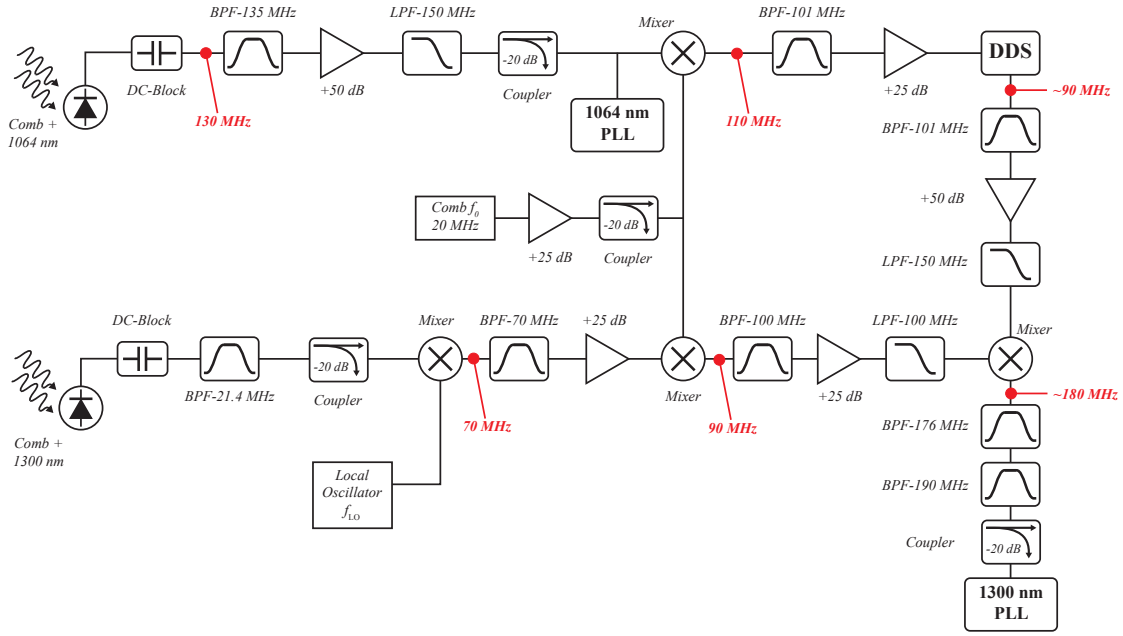

Figure 2.10: Scheme of the electronics used to implement the virtual beatnote locking. Band-pass and low-pass filters are indicated as BPF and LPF, followed by the central frequency and the cut-off frequency, respectively. The main frequencies in various positions are indicated in red.

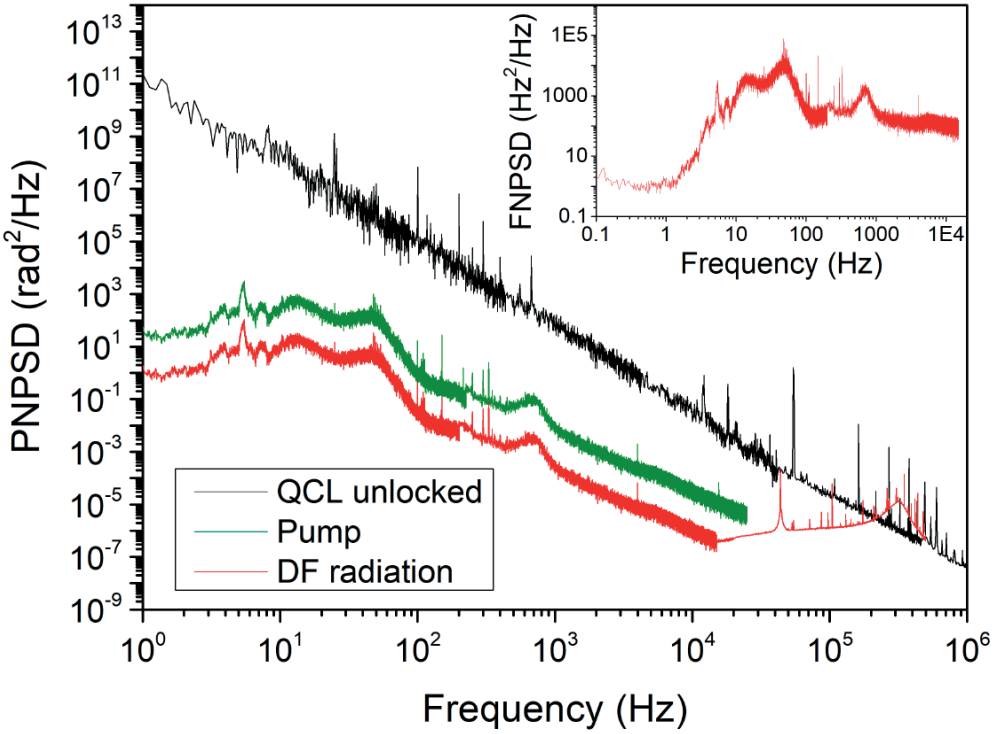

Figure 2.11: Phase noise of the free-running QCL (black), of the pump laser (green) and of the DF radiation (red). In the inset, the frequency-noise PSD of the DF radiation is shown.

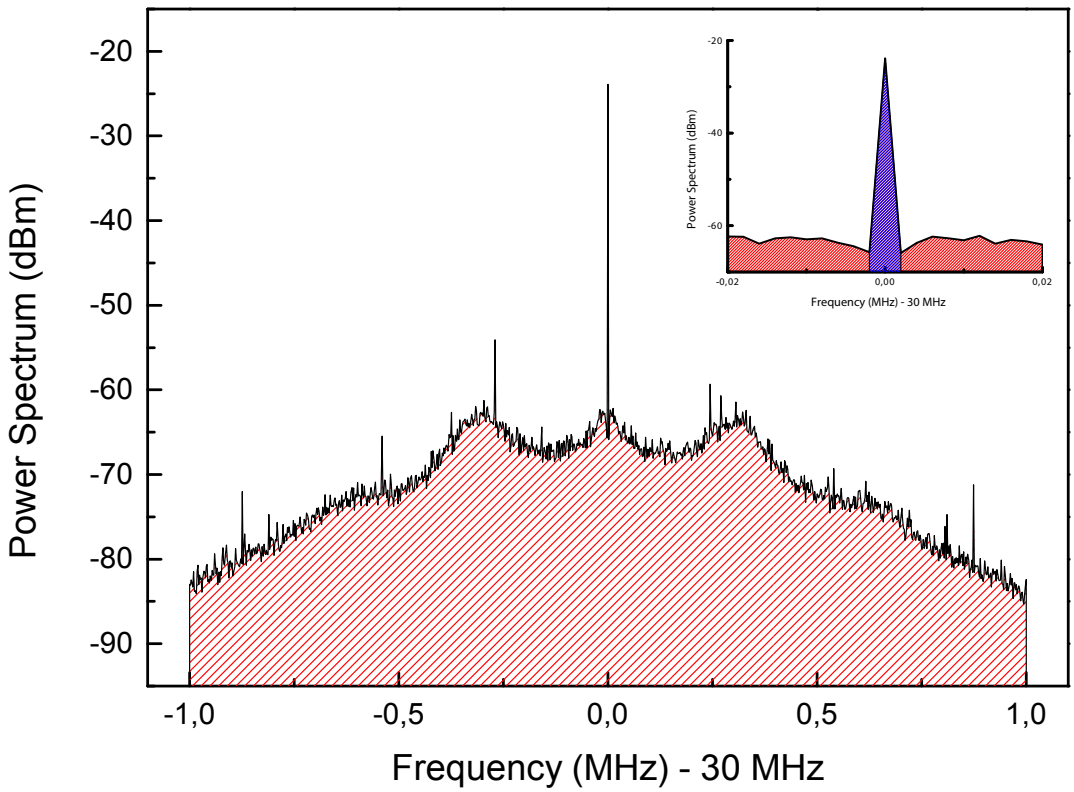

Figure 2.12: Beatnote between the generated DFG and the QCL. These data have also been reported in Figure 2.9 (d). In the inset a zoom of the central portion of the beatnote spectrum is shown. To calculate the effectiveness of the phase lock we integrated the area under the carrier P(0) (in blue) and the total area (shaded red) under the beatnote power spectrum. The ratio between these two quantities, $\eta = 0.7$, gives a quantitative measurement of the effectiveness of the phase lock.

Chapter 3

Laser Spectral Characterization

The spectrum of a laser source, even when it emits only on a single mode, is never perfectly monochromatic. Fluctuations of the optical phase cause rapid variations of the instantaneous frequency, and are thus responsible for the spectral broadening of the emitted radiation. The laser intensity profile $I(\nu)$ has a certain spectral distribution, and its full width at half maximum (FWHM) is usually referred to as laser *linewidth*. Phase vatiations fundamentally depend on spontaneously emitted photons, and the effect of this process on the laser linewidth can be quantified in terms of frequency noise power spectral density (FNPSD). Technological limits, such as mirrors instability in gas or dye lasers, or current and temperature fluctuations in semiconductor lasers, commonly provide the major contribution to laser line broadening.

In this chapter, we will first introduce the relationship between phase fluctuations and laser linewidth, then we will give a brief review of consolidated spectral characterization techniques. For all of them, critical points will be remarked: the technological limits of optical devices in the 5.5–9 µm frequency range, such as the very poor quality of optical isolators or the low sensitivity of photodiodes, does not allow us to perform sub-Doppler measurements and allows only "rough" FNPSD direct measurement. In the final section of this chapter we will introduce and discuss the basic idea beyond the method we used to overcome the limits of traditional approaches.

3.1 General Noise Theory

3.1.1 General properties of noisy signals

A noisy signal, such as the laser power or frequency, can be expressed as

$$P(t) = \langle P \rangle + \delta P(t), \tag{3.1}$$

with a constant and a time-dependent part (with zero mean value). If we consider noise-generating processes to be stationary and ergodic, the mean value, indicated here with $\langle\rangle$, can either denote the ensemble average or the average with respect to time

$$\langle P \rangle = \lim_{t' \to \infty} \frac{1}{t'} \int_{t_0}^{t_0+t'} P(t)\, dt. \tag{3.2}$$

According to equation (3.2), the average is indipendent of t_0. Noise fluctuations in the time domain can be described in terms of the autocorrelation function

$$\rho_P(\tau) = \langle \delta P(\tau) \delta P(t-\tau) \rangle\,, \tag{3.3}$$

while in the frequency domain they can be evaluated in terms of the noise power spectral density (NPSD), according to the Wiener-Khinchin theorem:

$$\mathrm{NPSD}_P(\nu) = \int_{-\infty}^{+\infty} \rho_P(\tau) e^{-i2\pi\nu\tau}\, d\tau = \lim_{t' \to \infty} \frac{1}{t'} \left| \int_0^{t'} \delta P(t) e^{-i2\pi\nu t}\, dt \right|^2. \tag{3.4}$$

The ergodicity hypothesis (equation (3.2)) has been exploited in the last passage. The Wiener-Khinchin theorem states that the autocorrelation function and the $\mathrm{NPSD}_P(\nu)$ form a Fourier pair. Therefore, the inverse Fourier transform gives back $\rho_P(\tau)$ as a function of the $\mathrm{NPSD}_P(\nu)$.

3.1.2 Laser linewidth and FNPSD

The electrical field emitted by a single-mode laser can be expressed as $Re[E(t)e^{i2\pi\nu_0 t}]$, where ν_0 is the carrier frequency and

$$E(t) = \sqrt{S(t)} e^{i2\pi\phi(t)} \tag{3.5}$$

is a slowly-varying field amplitude. In the present discussion we ignore the fluctuations in S, so that $S(t) = \langle S \rangle$. It is now worth considering the instantaneous frequency $\dot{\phi} = d\phi/dt$, that represents the deviation from the carrier ν_0. Following this notation, the frequency of the laser radiation is expressed, at the time t, as $\nu(t) = \nu_0 + \dot{\phi}(t)$. We define the differences

$$\delta\phi(t) = \phi - \left\langle \dot{\phi} \right\rangle t \tag{3.6}$$

$$\delta\dot{\phi}(t) = \dot{\phi} - \left\langle \dot{\phi} \right\rangle \tag{3.7}$$

so that the latter has zero mean value. In analogy with equation (3.1), $\dot{\phi}$ is written as a mean value plus a time varying part. Its noise fluctuations can be described, in time and frequency domain, by the autocorrelation function

$$\rho_{\dot{\phi}}(\tau) = \left\langle \delta\dot{\phi}(\tau) \delta\dot{\phi}(t-\tau) \right\rangle, \tag{3.8}$$

and by the frequency noise power spectral density

$$\mathrm{NPSD}_{\dot{\phi}}(\nu) \equiv \mathrm{FNPSD}(\nu), \tag{3.9}$$

respectively. The Wiener-Khinchin theorem relates these two quantities so that, in analogy with equation (3.4), FNPSD can be written as:

$$\begin{aligned} \mathrm{FNPSD}(\nu) &= \int_{-\infty}^{+\infty} \rho_{\dot{\phi}}(\tau) e^{-i2\pi\nu\tau}\, d\tau = \\ &= \lim_{t'\to\infty} \frac{1}{t'} \left| \int_0^{t'} \delta\dot{\phi}(t) e^{-i2\pi\nu t}\, dt \right|^2 . \end{aligned} \tag{3.10}$$

According to this definition, FNPSD includes contributions from both positive and negative frequencies. It is usually referred to as a *2-sided* frequency noise power spectral density and is measured in $\mathrm{Hz}^2/\mathrm{Hz}$. However, by definition, the FNPSD of a real signal is an even function. Therefore, it is also common to restrict the analysis to positive frequencies only, defining the *1-sided* frequency noise power spectral density as

$$\mathrm{FNPSD}_{1s} = 2 \cdot \mathrm{FNPSD} \qquad \text{for } \nu \geq 0, \tag{3.11}$$

which is still measured in $\mathrm{Hz}^2/\mathrm{Hz}$. From now on, we will refer to the 2-sided power spectral density when we write FNPSD.

We consider now the phase difference for a certain delay τ, $\Delta\phi = \delta\phi(t) - \delta\phi(t-\tau)$. This quantity can be easily observed in an interferometric set up and its mean square can be written in terms of FNPSD as [21]

$$\left\langle \Delta\phi^2 \right\rangle = \left\langle [\delta\phi(t) - \delta\phi(t-\tau)]^2 \right\rangle = \tau^2 \int_{-\infty}^{+\infty} \mathrm{FNPSD}(f) \frac{\sin^2(2\pi f\tau/2)}{(2\pi f\tau/2)^2}\, df. \tag{3.12}$$

Recalling equation (3.6), the slowly varying field amplitude can be written as

$$E(t) = \sqrt{\langle S \rangle} e^{i2\pi[<\dot{\phi}>t + \delta\phi(t)]}. \tag{3.13}$$

The field autocorrelation function is then

$$\langle E(t) E^*(t-\tau) \rangle = \langle S \rangle\, e^{i2\pi \langle \dot{\phi} \rangle \tau} \left\langle e^{i2\pi\Delta\phi} \right\rangle. \tag{3.14}$$

We express the term $\left\langle e^{i2\pi\Delta\phi} \right\rangle$ as a function of its probability density distribution $p(\Delta\phi)$:

$$\left\langle e^{i\Delta\phi} \right\rangle = \int_{-\infty}^{+\infty} p(\Delta\phi) e^{i2\pi\Delta\phi}\, d(\Delta\phi). \tag{3.15}$$

The main contribution to phase variations comes from the spontanous emission of photons, a large number of indipendent events. Therefore, according to the central limit theorem, $\Delta\phi$ follows a Gaussian probability density distribution:

$$p(\Delta\phi) = \frac{1}{\sqrt{2\pi \left\langle \Delta\phi^2 \right\rangle}} e^{-\frac{1}{2}\frac{\Delta\phi^2}{\langle \Delta\phi^2 \rangle}}, \tag{3.16}$$

so that the mean value of the exponential term in equation (3.14) can be written as

$$\left\langle e^{i2\pi\Delta\phi} \right\rangle = e^{-\frac{1}{2}\left\langle 4\pi^2\Delta\phi^2 \right\rangle}. \tag{3.17}$$

The field autocorrelation function becomes then

$$\langle E(t)E^*(t-\tau)\rangle = \langle S\rangle\, e^{i2\pi\left\langle\dot{\phi}\right\rangle\tau} e^{-2\pi^2<\Delta\phi^2>}. \tag{3.18}$$

Once the field autocorrelation function is known, the Wiener-Khinchin theorem relates it to the power spectrum $W_E(\nu)$

$$\begin{aligned} W_E(\nu) &= \int_{-\infty}^{+\infty} \langle E(t)E^*(t-\tau)\rangle\, e^{-i2\pi\tau\nu}\, d\tau = \\ &= \langle S\rangle \int_{-\infty}^{+\infty} e^{i2\pi\left\langle\dot{\phi}\right\rangle\tau} e^{-2\pi^2<\Delta\phi^2>} e^{-i2\pi\tau\nu}\, d\tau. \end{aligned} \tag{3.19}$$

If we now define $\Delta\nu = \left\langle\dot{\phi}\right\rangle - \nu$ and recall the equation (3.12), the power spectrum becomes

$$W_E(\Delta\nu) = \langle S\rangle \int_0^{+\infty} d\tau \cos(2\pi\tau\Delta\nu) e^{-Z(\tau)} \tag{3.20}$$

with

$$Z(\tau) = 4\int_{1/T}^{+\infty} \mathrm{FNPSD}_{1s}(f) \left[\frac{\sin\pi f\tau}{f}\right]^2 df, \tag{3.21}$$

where T is the timescale on which the FNPSD is acquired. In fact, we should integrate the quantity in equation (3.21) from $\nu = 0$ to infinity, obtaining a divergent integral. However, if we assume that the FNPSD measurement cannot be done for an infinite time, we note that frequencies below the $1/T$ limit are not affecting the measured FNPSD and, hence, the power spectrum.

This result is completely general: equations (3.20) and (3.21) are valid independently of the method used for measuring the FNPSD.

In real life experiments it is not rare to measure phase noise PSD instead of frequency noise. According to equation (3.4), PNPSD is defined as the Fourier transform of the phase autocorrelation function $\rho_\phi(\tau)$:

$$\mathrm{PNPSD}(\nu) = \lim_{t'\to\infty} \frac{1}{t'} \left| \int_0^{t'} \delta\phi(t) e^{-i2\pi\nu t}\, dt \right|^2. \tag{3.22}$$

We demonstrated earlier that the FNPSD can be written as

$$\mathrm{FNPSD}(\nu) = \lim_{t'\to\infty} \frac{1}{t'} \left| \int_0^{t'} \delta\dot{\phi}(t) e^{-i2\pi\nu t}\, dt \right|^2. \tag{3.23}$$

That, given the well known properties of the Fourier transform, is equal to

$$\begin{aligned} \mathrm{FNPSD}(\nu) = \lim_{t'\to\infty} \frac{1}{t'} \left| (-i2\pi\nu) \int_0^{t'} \delta\phi(t) e^{-i2\pi\nu t}\, dt \right|^2 = \\ = (2\pi\nu)^2 \mathrm{PNPSD}(\nu). \end{aligned} \tag{3.24}$$

PNPSD is measured in $\mathrm{rad}^2/\mathrm{Hz}$.

3.1.3 Spectral lineshape

The direct measurement of the frequency noise power spectral density is the most complete way to characterize a laser spectrum: it gives a complete knowledge of the noise contributions for different Fourier frequencies and can be used to identify the different noise processes affecting the overall line profile. Moreover, by means of an integration [28], it can be used to retrieve the shape of the laser frequency spectrum and the value of its linewidth over the desired timescale. FNPSD(f) can be expanded in a power series [67], where the main contributions come from the constant and the $1/f$ term

$$\mathrm{FNPSD}_{1s} = h_0 + h_{-1}\frac{1}{f}, \tag{3.25}$$

with coefficients h_0 and h_{-1}, respectively. As a matter of fact, many diode and quantum cascade lasers exhibit this behaviour, with white and flicker noise being the two main causes of spectral line broadening. As an example, in Figure 3.1 is reported the FNPSD_{1s} of a quantum cascade laser emitting in the Mid-IR: at low frequencies it is clearly visible a $1/f$ trend, while for higher frequencies the FNPSD tends towards a constant value, independent from frequency (white noise). Therefore, it is worth to discuss the contributions to the spectral line shape of white and $1/f$ frequency noise.

White frequency noise

If only a white frequency noise contribution is considered, the $\mathrm{NPSD}_{\dot\phi} = \mathrm{FNPSD}$ is indipendent of frequency. Recalling equation (3.12)

$$\begin{aligned}\left\langle \Delta\phi^2 \right\rangle &= \tau^2 \int_{-\infty}^{+\infty} \mathrm{FNPSD}\frac{\sin^2(2\pi\nu\tau/2)}{(2\pi\nu\tau/2)^2}\, d\nu = \\ = \tau^2 \cdot \mathrm{FNPSD} \cdot \frac{1}{\pi\tau}\int_{-\infty}^{+\infty} \mathrm{sinc}^2(2\pi\nu\tau/2)\, d(2\pi\nu\tau/2) &= \\ = \tau \cdot \mathrm{FNPSD}&\end{aligned} \tag{3.26}$$

According to eqs. (3.14) and (3.26), the autocorrelation function of the field amplitude can be written as

$$\langle E(t)E^*(t-\tau)\rangle = \langle S\rangle\, e^{i2\pi\langle\dot\phi\rangle\tau} e^{-2\pi^2\tau\cdot\mathrm{FNPSD}}. \tag{3.27}$$

The Fourier transform of the the field amplitude autocorrelation function gives the power spectrum:

$$W_E(\nu) = \frac{\langle S\rangle}{2}\frac{1}{i\left(\nu - \left\langle\dot\phi\right\rangle\right) + \pi\mathrm{FNPSD}} + \text{c.c.} \tag{3.28}$$

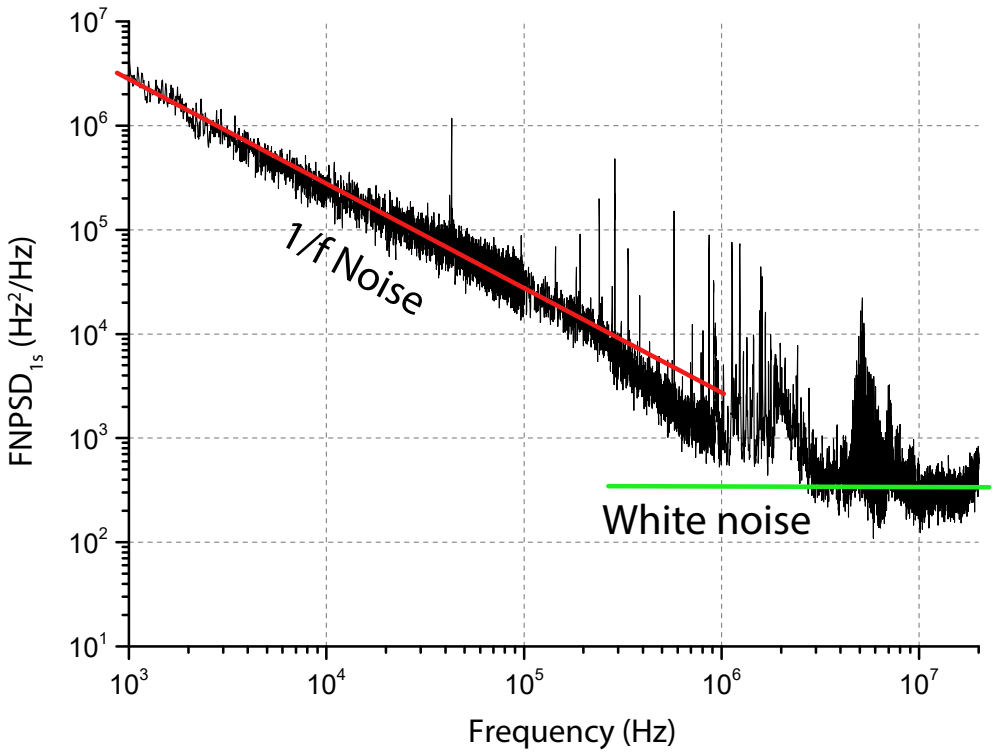

Figure 3.1: *1-sided* FNPSD of a quantum cascade laser emitting at 4.3 µm. FNPSD has been measured using a molecular absorption line in strong absorbance regime as a frequency-to-amplitude noise converter. $1/f$ and white frequency noise are the main contribution respectively below and above 1 MHz.

This spectrum has a Lorentzian profile, centered around $\langle\dot{\phi}\rangle$ with a full width half maximum

$$\Delta\nu = 2\pi\text{FNPSD} = \pi\text{FNPSD}_{1s} = \pi h_0. \tag{3.29}$$

Note that the actual laser spectrum is the spectrum of the complex amplitude, whereas we deal here only with the slowly-varying amplitude $E(t)$ (see equation (3.5)).

$1/f$ frequency noise

As many other devices, at low frequencies QCL's and diode's frequency noise exhibits a $1/f$ behaviour. To investigate the contribution of this kind of noise to the spectrum line shape, we neglect the Lorentzian broadening contribution due to white frequency noise and suppose:

$$\text{FNPSD} = h_{-1}\frac{1}{f} \tag{3.30}$$

Since the FNPSD(f) is an even function, equation (3.12) can be written as

$$\left\langle \Delta\phi^2 \right\rangle = \frac{2h_{-1}}{\pi^2} \int_0^{+\infty} \frac{\sin^2(\pi f \tau)}{f^3}\, df. \tag{3.31}$$

At $f = 0$ this integral would yield an infinite variance of the phase change. But since the measurement time t^* cannot be infinite, this problem is avoided: the lower frequency can be exactly zero only for an infinite $\langle \Delta\phi^2 \rangle$ measurement time, whereas for a finite t^* the lower integration limit is a frequency f_l, proportional to the inverse of t^*. With this expedient one can integrate [67] the quantity in equation (3.31), calculate the field autocorrelation function and from its Fourier transform, finally, obtain the power spectrum

$$W_E(\nu) = \frac{\langle S \rangle}{2} \frac{1}{\sqrt{\pi}\sigma_\nu} e^{-(\langle \dot{\phi} \rangle - \nu)^2/\sigma_\nu^2}. \tag{3.32}$$

The variance σ_ν^2 is given by [67]

$$\sigma_\nu^2 = \frac{3.56}{2\pi} h_{-1}. \tag{3.33}$$

The $1/f$ frequency noise contribution broadens the emission spectrum, having a Gaussian shape with a FWHM

$$\Delta\nu = 2\sqrt{\ln 2}\sigma_\nu \sim 1.25\sqrt{h_{-1}} \tag{3.34}$$

Most of the commercial IR laser sources exhibit a spectral profile affected both by $1/f$ and "white" frequency noise, that can be well described by a Voigt profile being the convolution between the Gaussian and the Lorentzian contributions calculated above.

3.2 Interferometric techniques

One of the most intuitive way to convert phase or frequency fluctuations of a laser source into some measurable quantity is to observe the interference fringe pattern at the output of an interferometer. The beatnote of a laser with itself can give enough information to calculate the laser linewidth: this technique is known as *self heterodyne*. Consider a Mach Zehnder interferometer (Figure 3.2), where a modulator has been introduced in one of the two arms, shifting the angular frequency ω by a quantity ω_s . The transmitted field at the output of the interferometer will be

$$E_T(t) = A(e^{i\omega_s t} E_L(t) + E_L(t - \tau)). \tag{3.35}$$

Therefore, the transmitted intensity will be

$$P_T(t) = |A^2|\{|E_L(t)|^2 + |E_L(t - \tau)|^2 + 2Re[e^{i\omega_s t} E_L(t) E_L^*(t - \tau)]\}. \tag{3.36}$$

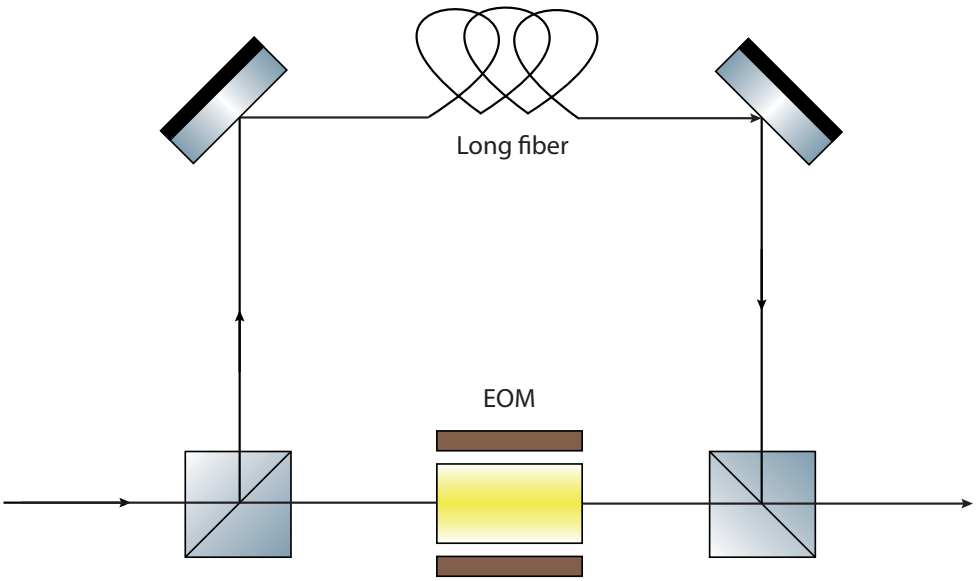

Figure 3.2: In a Mach Zehnder interferometer, the laser beam is split in two arms. A long fiber induces a certain delay τ while in the other arm a modulator shifts the laser frequency by ω_s. From the analysis of the interferometer output with an RF-spectrum analyzer it is possible to measure the laser linewidth. This technique is known as self-heterodyne.

If we neglect the intensity noise and note that the frequency shift can be interpreted as a phase difference $\phi_0 = \omega_s t$ between the two arms, we can write the power as

$$P_T(t) = P_{T_0}[1 + \cos(\omega_s t + \Delta\phi(t, \tau))] \tag{3.37}$$

where P_{T_0} is a constant reference power and

$$\Delta\phi(t, \tau) = \phi(t) - \phi(t - \tau) \tag{3.38}$$

is the phase change. Fluctuations on the phase change are transferred to the output power of the interferometer. The autocorrelation function and the spectrum of the interferometer output power can be determined for any delay [52], but it is worth showing what happens in the situation of short or long induced delays. For this purpose we introduce a parameter that quantifies the maximum possible delay between two components of the emitted optical field that can still interfere. If we suppose only white frequency noise affecting the laser source, the FNPSD is

independent of frequency and we can define a coherence time t_c as:

$$\text{FNPSD} = 2/t_c. \tag{3.39}$$

This definition is not unique and many other can be found in literature. For $\tau \ll t_c$, $\Delta\phi(t,\tau) \ll 1$ and thus $\cos\Delta\phi(t,\tau) \sim 1$, $\sin\Delta\phi(t,\tau) \sim \Delta\phi(t,\tau)$. Equation (3.37) becomes

$$P_T(t) = P_{T_0}[1 + \cos\omega_s t + \Delta\phi(t,\tau)\sin\omega_s t]. \tag{3.40}$$

Power is distributed in a central frequency ω_s and sidebands due to the phase change $\Delta\phi(t,\tau)$. From a simple measurement on an RF-spectrum analyzer of the output power of an interferometer, it is thus possible to calculate the spectral density of the phase change, and thus the FNPSD [36]. This method can be used to calculate linewidths in the sub-kHz range.

For $\tau \gg t_c$, let's consider again equation (3.37). If we neglect the dc-component of the output power of the interferometer, we have

$$P_T(t) \sim P_{T_0}\cos\left(\omega_s t + \Delta\phi(t,\tau)\right). \tag{3.41}$$

We now compare the spectrum of the interferometer output with the spectrum of the laser emitted field, the real part of E(t) (equation (3.13))

$$Re[E(t)] \sim \cos\left[2(\pi\left\langle\dot{\phi}\right\rangle + \Delta\phi)\right] \tag{3.42}$$

The frequency fluctuations of the interferometer output are described by the spectral noise density of the phase change, $\text{NPSD}_{\Delta\phi}$ while the FNPSD gives informations about the frequency noise of the laser electrical field. Comparing these two quantities, it can be demonstrated that [37]

$$\text{NPSD}_{\Delta\phi} = 2\text{FNPSD} \quad \text{for} \quad \tau \gg t_c. \tag{3.43}$$

If a laser is mainly affected by white frequency noise, therefore, the spectral linewidth is proportional to the FNPSD (see equation (3.29)), and then is just twice the spectral width of the interferometer output. This method only requires a long enough fiber to induce a sufficient delay between the two arms, and an RF-spectrum analyzer.

This measurement method is widely used for sources ranging from the visible to the IR, but again, the effectiveness of the measurement depends on the rise-time and sensitivity of the detectors used: measuring the radio frequency beat note of two laser beams superimposed on a fast photo diode is hindered by the relatively large background noise of electrooptical devices in the Mid-IR. Moreover, for a laser in the Mid-IR it could be tricky to introduce a delay $\tau \geq t_c$. As an example, let us consider a diode laser mostly affected by white frequency noise and whose narrow linewidth is expected to be 100 kHz or less. From equation (3.29), we

can deduce that a delay of the order of microseconds must be induced into one of the inteferometer arms. Optical fibers usually introduce 5 μs/km delay, so that a km-long fiber is needed to obtain the required delay. In the near-IR this does not represent a limitation, whereas in the Mid-IR commercial fibers or even specific Zirconium Fluoride (ZrF_4) or Indium Fluoride (InF_3) fibers show, above 5.5 micron wavelength, losses of 3 dB/m or more.

3.3 Frequency-Amplitude noise conversion

In addition to interferometric techniques, another direct measurement of a laser frequency noise power spectral density can be obtained converting frequency fluctuations into detectable intensity variations. To do so, it is possible to use the slope of a molecular absorption line or the mode of an optical resonator. An experimental setup like the one in Figure 3.3 (a) is required: the laser frequency is finely tuned on the slope of the molecular absorption line (or cavity mode), the yellow area in Figure 3.3 (b). The slope here is almost linear, therefore any frequency fluctuation is almost linearly converted into an amplitude fluctuation, measured by a photodiode. Sending the photocurrent to an RF-spectrum analyzer it is possible to measure the laser FNPSD.

For a precise measurement, the converter must introduce a negligible noise, while providing a gain factor suitable for a good detection. In addition, the detector must feature low-noise and high speed to allow the signal to emerge above the background given by the electronic or the laser amplitude noise. Unfortunately, Mid-IR detectors have typically worse performances in terms of noise level and responsivity than near-IR detectors. This is particularly true for the region between 5.5 and 9 µm: below 5.5 µm high sensitive InSb photovoltaic detectors can be found, with very low noise levels and good noise equivalent power (NEP). In the 9–10 µm range, due to the presence of CO_2 lasers, good components and instrumentation have been developed. But in the 5.5–9 µm range, the choice of the optical discriminator is crucial: the narrower the laser, the steeper the slope required (Figure 3.3). For this reason, the best candidates for frequency-to-amplitude noise conversion are, in principle, sub-Doppler molecular absorption lines or high finesse optical cavity modes.

3.3.1 Cavities

In a classical Fabry-Perot (F-P) configuration, the width of a cavity mode can be expressed as the ratio between the free spectral range and the finesse. To have a high frequency-to-amplitude noise conversion factor, the cavity should have very narrow modes, a condition that requires either high Finesse or a small free spectral range. High finesse means high mirror reflectivity, that is usually poorer in the

Mid-IR than in the visible and near-IR regions. Optical cavities with a small free spectral range, on the other hand, have the major drawback of mechanical instability because of their considerable lenght: this would introduce an external noise at low frequencies in the output signal that depends on the cavity length variations. Furthermore, when dealing with quantum cascade lasers, the optical feedback coming from a F-P resonator can be a serious limit.

Among the newest tools for Mid-IR optics, an important role is played by crystalline whispering gallery mode resonators (WGMRs). These devices do not present some of the typical drawbacks of F-P resonators. They exploit total reflection inside the material, which makes them independent of optical coatings, and have the advantage of being made of materials, like fluoride crystals, that are highly transparent over an extremely broad spectral range. CaF_2 resonators, for example, are transparent from the UV to the Mid-IR, and Q-factors as high as 10^{10} in the near-IR and 10^8 in the Mid-IR have been measured [63, 39]. Thermal stabilization is not an issue, thanks to their typical small dimensions (toroidal resonators have, typically, diameters of millimiters).

These devices have found application in nonlinear frequency generation and sensing, among other applications, and can be a valid alternative to high-finesse Fabry-Perot resonators for Mid-IR laser frequency stabilization, or linewidth narrowing [20, 12].

3.3.2 Molecules

An optical cavity is not the only option for an efficient frequency-to-amplitude noise conversion. If a strong molecular absorption line falls into the laser frequency tuning range, it can be used, in analogy with cavity modes (Figure 3.3), to measure the laser FNPSD. Many ideal candidates can be found in the so-called "fingerprint region". Absorption lines in this region of the molecular spectrum often exhibit noticeable linestrenghts, and this is a great advantage for sensing and also for noise measurements: when working in high absorbance regime, the slope angular coefficient (i.e.,the conversion efficiency) is maximized. It is therefore mandatory to use a strong transition for this kind of measurements.

In addition to the high number of available absorption lines, using molecules as frequency-to-amplitude noise converter has an even more appealing trait: rovibrational transitions in the Mid-IR have typical natural linewidths of the order of tens-hundreds of Hz. It is thus tempting to exploit such sharp spectral features to characterize very narrow laser sources. This requires to significantly reduce the additional contributions causing linewidth broadening, as discussed below.

3.3.3 Line broadening of molecular transitions

Consider an absorption line of a certain molecular spectrum: if the molecule is excited from a state with energy E_k to an upper state having energy E_i, the absorbed intensity $I(\nu)$ will be distributed around a central frequency $\nu_0 = (E_i - E_k)/h$. The function $I(\nu)$ around ν_0, in analogy with a monochromatic laser emission spectrum, is usually referred to as *line profile*. If ν_1 and ν_2 are the frequencies for which $I(\nu_1) = I(\nu_2) = I(\nu_0)/2$, then $\delta\nu = \nu_2 - \nu_1$ is the FWHM, or *linewidth*. The region between ν_1 and ν_2 is usually named *Kernel* of the line, while the remaining part outside this interval are named *line wings*. To avoid 2π factors in the equations, the FWHM is often written in terms of angular frequency $\omega = 2\pi\nu$, so that the linewidth becomes $\delta\omega = 2\pi\delta\nu$. The relative width, however, is the same

$$\left|\frac{\delta\nu}{\nu}\right| = \left|\frac{\delta\omega}{\omega}\right| = \left|\frac{\delta\lambda}{\lambda}\right| \tag{3.44}$$

also in terms of wavelength $\lambda = c/\nu$.

In the following, a brief overview will be given of the effects that contribute to the broadening of the line profile.

Natural linewidth

Heisenberg's uncertainty principle, more precisely the time-energy inequality, sets the lower limit for any transition linewidth: if an excited state has a lifetime τ_f, its energy can be determined only with an uncertainty $\Delta E_f \sim \hbar/\tau_f$. The same argument holds for the lowest energy state of the transition, so that $\Delta E = \sqrt{\Delta E_i^2 + \Delta E_f^2}$ and the frequency of the transition $\omega_{fi} = (E_f - E_i)/\hbar$ has a total uncertainty given by

$$\delta\omega_{fi} = \sqrt{(1/\tau_i^2) + (1/\tau_f^2)}, \tag{3.45}$$

or, in terms of frequency ν,

$$\delta\nu_{fi} = \frac{1}{2\pi}\sqrt{(1/\tau_i^2) + (1/\tau_f^2)}. \tag{3.46}$$

The same result can be obtained if we use for the excited molecule a damped harmonic oscillator model. In addition it can be shown, following this argument, that the line profile follows a Lorentzian distribution with FWHM still given by equations (3.45) and (3.46).

Doppler broadening

Consider a molecule with a velocity $v = \{v_x, v_y, v_z\}$ relative to the laboratory frame. Let's suppose that ω_0 is the central frequency of an absorption line, in the

molecule coordinate system. For an observer in the laboratory frame, this line is Doppler shifted:

$$\omega = \omega_0 + \boldsymbol{k} \cdot \boldsymbol{v}. \tag{3.47}$$

For the observer, the absorption frequency is increased if the molecule moves along the laser propagation direction($\boldsymbol{k} \cdot \boldsymbol{v} > 0$), while is decreased if they have opposite directions ($\boldsymbol{k} \cdot \boldsymbol{v} < 0$). If we define the positive z- direction to be the light propagation direction, and $\boldsymbol{k} = \{0,0,k_z\}$, we have

$$\omega = \omega_0(1 + v_z/c). \tag{3.48}$$

At a temperature T, the number of molecules in an energy level E_i with a velocity component between v_z and $v_z + dv_z$ is given by the Maxwell-Boltzmann distribution

$$n_i(v_z)dv_z = \frac{N_i}{v_p\sqrt{\pi}} e^{-(v_z/v_p)^2} dv_z, \tag{3.49}$$

where $N_i = \int n_i(v_z)dv_z$ is the molecule density in the level E_i, $v_p = (2k_BT/m)^{1/2}$ is the most probable velocity, m is the mass of a single molecule and k_B is the Boltzmann constant. Considering the equation (3.48), and the relationship $dv_z = (c/\omega_0)d\omega$, the previous equation can be written as

$$n_i(\omega)d\omega = N_i \frac{c}{\omega_0 v_p\sqrt{\pi}} e^{-(\frac{c(\omega-\omega_0)}{\omega_0 v_p})^2} d\omega, \tag{3.50}$$

and gives the number of molecules with absorption frequencies between ω and $\omega + d\omega$. The absorbed radiant power is proportional to $n_i(\omega)d\omega$, so that the intensity profile of a Doppler broadened line is

$$n_i(\omega)d\omega = I_0 e^{-(\frac{c(\omega-\omega_0)}{\omega_0 v_p})^2}. \tag{3.51}$$

The full width half maximum of this Gaussian profile is

$$\delta\omega_D = 2\sqrt{\ln 2}\omega_0 v_p/c = \left(\frac{\omega_0}{c}\right)\sqrt{(8k_BT\ln 2)/m}. \tag{3.52}$$

In terms of frequency ν, having in mind equation (3.44), the linewidth can be written as

$$\delta\nu_D = 2\sqrt{\ln 2}\nu_0 v_p/c = \left(\frac{\nu_0}{c}\right)\sqrt{(8k_BT\ln 2)/m}. \tag{3.53}$$

Transit time broadening

Spectroscopy experiments in the mid infrared quite often are performed analyzing rovibrational transitions involving metastable states. Such transitions can have spontaneous lifetimes several orders of magnitude longer than the interaction

time among molecules and IR radiation. Supposing a monochromatic electrical field $E = E_0 cos(\omega_0 t + \phi)$ interacting for a time T with constant amplitude, the associated frequency spectrum can be obtained by its Fourier transform

$$A(\omega) = \frac{1}{\sqrt{2\pi}} \int_0^T x_0 \cos\omega_0 t e^{-i\omega t} dt. \tag{3.54}$$

In the limit of $T \to +\infty$ the result would be a delta function centered in ω_0, but for finite interaction times the spectral line intensity profile $I(\omega) = A^* A$ must be broader, in particular, for $(\omega - \omega_0) \ll \omega_0$, it becomes [24]

$$I(\omega) = C \frac{\sin^2[(\omega - \omega_0)T/2]}{(\omega - \omega_0)^2}, \tag{3.55}$$

with a full width at half maximum:

$$\delta\omega_{tt} = \frac{5.6}{T}, \tag{3.56}$$

so that

$$\delta\nu_{tt} \sim \frac{1}{T}. \tag{3.57}$$

In a molecular beam experiment, it is quite common to have molecules interacting with lasers perpendicularly. In this experimental condition, the interaction still stands for a finite time T, but the amplitude of the electric field cannot be considered constant. Suppose the field to be

$$E = E_0 e^{-r^2/w^2} cos(\omega t). \tag{3.58}$$

w is the radius of the beam where the amplitude drops of a factor $1/e$, so that $T = 2w/v$ where v is the molecules mean velocity. The Fourier transform of the field gives back, instead of equation (3.55),

$$I(\omega) = I_0 exp\left(-(\omega - \omega_0)^2 \frac{w^2}{2v^2}\right), \tag{3.59}$$

with a FWHM of

$$\delta\omega'_{tt} = 2.4 \frac{v}{w}, \tag{3.60}$$

or

$$\delta\nu'_{tt} = 0.4 \frac{v}{w}, \tag{3.61}$$

3.3.4 Sub-Doppler techniques

The Doppler broadening of a transition around 50 THz for a molecule with a mass of, say, 50 amu at room temperature is just below 100 MHz FWHM (see equation (3.52)). To narrow down the transition linewidth, it is necessary to implement some Doppler-free technique. Sub-Doppler spectroscopy schemes such as saturation or two-photon spectroscopy allow to overcome this limit. In the saturation spectroscopy scheme a strong pump and a weak probe propagate in opposite directions: if the two lasers are red (blue) detuned with respect to the molecular transition, the pump beam will interact with molecules moving towards (away) the laser, while the probe will interact with those moving away (towards). If, and only if, both lasers are resonant, they will interact with molecules having the same velocity class, those having velocity component equal to zero in the laser's propagation direction. The pump beam will populate the excited level, while scanning the probe laser frequency will produce a narrow dip in the absorption line: when a resonant photon from the probe beam interacts with an excited molecule, stimulated emission occurs, creating a dip in the absorption profile. The spectral width of this dip is not affected by Doppler broadening, since this signal comes from molecules with the same velocity.

Other techniques, such as the previously mentioned two-photon absorption, are based on different processes, but share with the saturation absorption a crucial aspect of the experimental scheme: they require overlapped, counter-propagating laser beams. For the Mid-IR source under analysis, this represents a serious limitation. QCLs are particularly sensitive to back-reflections and optical isolators, in the 6 µm spectral region, feature either very poor transmission or very poor isolation. Nontrivial schemes would be necessary, making use of polarizing optics and/or Brewster angle windows which, when possible, could however significantly reduce the available optical power.

3.4 Molecular beams

A possible solution to strongly reduce the Doppler line broadening, that circumvents optical feedback and other issues, is provided by molecular beams. In a setup like the one described in section 2.1 molecules are forced to travel along one definite direction and do not interact each other. Typical translational velocity distributions correspond to temperatures of a few K: this dense phase space distribution allows for a strong signal even when we select a subset of molecules with a very narrow velocity distribution. As an example, consider a molecular beam travelling in the z direction. The beam can be collimated by two narrow (tens of microns) slits, spaced by several tens of centimeters. The velocity spread in transversal directions can be drastically reduced, down to few m/s, according to our trajectory simulations. For a vibrational transition in the Mid-IR ($\omega_0 \sim 50$

THz), such a velocity spread ($v_p \sim 1$ m/s) would induce a Doppler broadening, according to equation (3.52), of hundreds of kHz.

Although in a molecular beam experiment the Doppler contribution to line broadening can be drastically reduced, there is a major drawback: unlike what happens in a traditional cell spectroscopy experiment, detection cannot be done via direct measurement of the optical power absorbed by the molecular sample, because of the extremely low number of molecules. Our molecular beam, for example, is obtained by pulsing a mixture of CO in Ne into a vacuum chamber through a supersonic valve at a repetition rate of 10 Hz. Each small cloud has a density of 10^{11} molecules per cm^3, meaning that the involved number of molecules is orders of magnitude less than those contained in a cell for a typical spectroscopic experiment. Therefore, there is no room for direct absorption measurements.

For instance, in our setup we implemented a state selective technique that ionizes vibrationally excited molecules and detects ions on a micro channel plate. Such a technique introduces an additional noise source in the output signal, i.e. amplitude and frequency fluctuations of the ionizing laser. As already pointed out in section 3.3, when using a molecular absorption line (or a high-Q cavity mode) stability of the FN-to-AN converter is required, so to avoid further noise contribution and effectively measure the FNPSD of the laser under analysis. Actually, it is not possible to rule out the noise contribution coming from this additional laser source. A different approach is required.

A possible way to measure laser linewidth is to record the population of the excited state while scanning the laser frequency through the resonance. The output signal will be the convolution between the finite laser linewidth and the molecular absorption profile: the most important required feature for this analysis is the sharpness of the spectral line, so that the spectral finite width of the output signal can be attributed mainly to the laser linewidth.

As we will show in the following chapters, under actual experimental conditions, it is possible to reduce the width of the absorption line down to 100–200 kHz, with the Doppler broadening being the main broadening contribution.

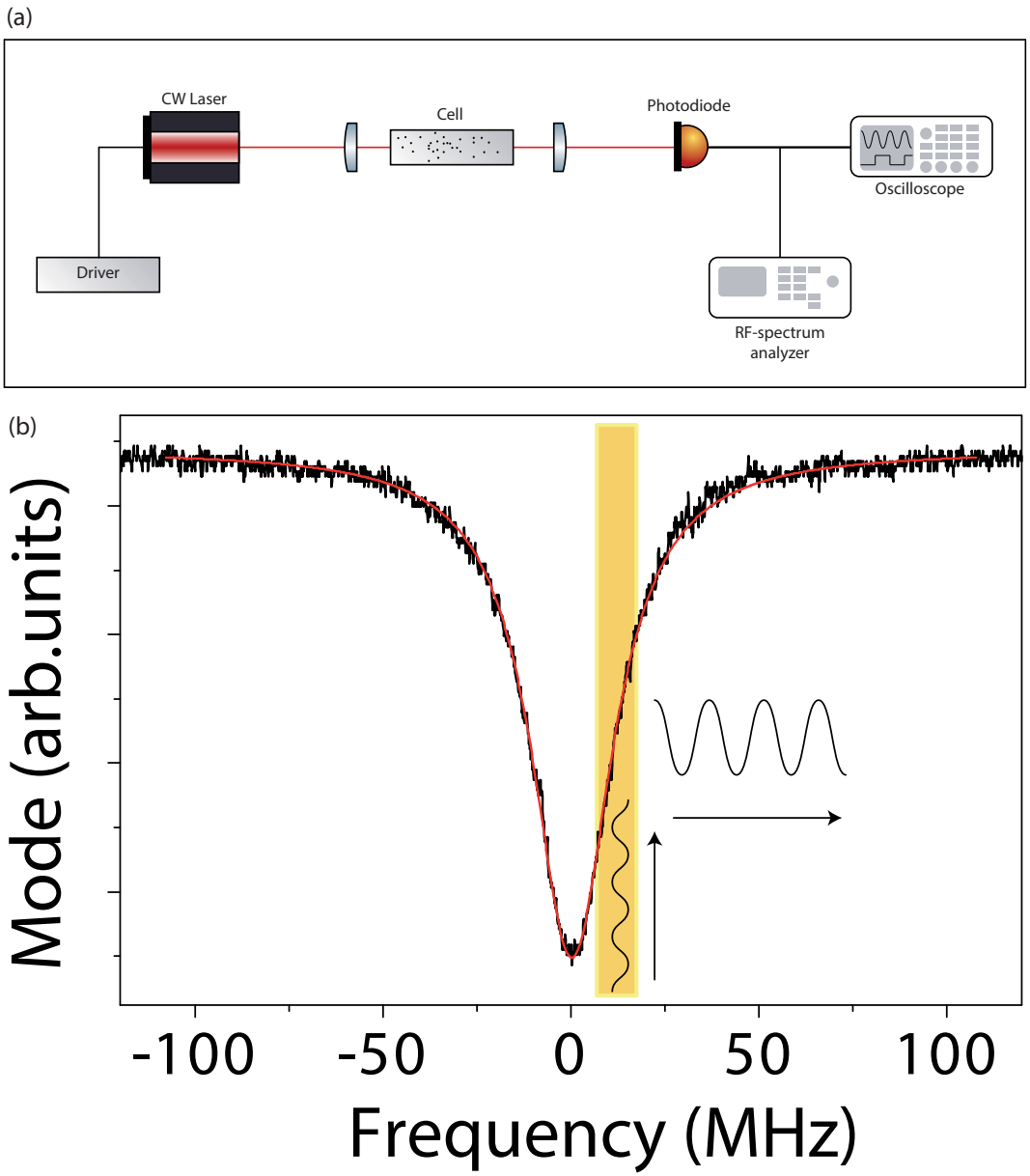

Figure 3.3: (a) FNPSD measurement with a frequency-to-amplitude converter: the laser frequency is tuned to half the slope of a molecular absorption line (or a cavity mode). The transmitted light is then collected and detected by a photodiode. Thanks to an RF-spectrum analyzer it is possible to measure the spectrum of the amplitude variations of the transmitted light. (b) At half the slope of the optical discriminator (yellow area), the conversion between frequency and amplitude fluctuations is almost linear. The higher the slope, the higher the conversion factor, the higher the resolution.

Chapter 4

Characterization of the Mid-IR radiation

As already mentioned in Section 3, there are several consolidated methods for the direct measurement of a laser linewidth, like self heterodyne or FNPSD measurements via conversion of frequency-to-amplitude fluctuations using the mode of a high-finesse cavity or a strong molecular absorption. Unfortunately, these techniques, when applied to a laser emitting above 5.5 µm, often present major drawbacks that prevent high resolution measurements. In a self-heterodyne setup, for example, a sufficient delay must be introduced between the two arms, but commercially-available optical fibers experience high losses in this spectral range. Or, when using a cavity mode as noise converter, one needs very steep flanks at the resonances to boost the conversion factor. This can be achieved either with a high finesse or with a small free spectral range. High finesse requires high mirror reflectivity, that can be hardly achievable in the infrared range. On the other hand, a cavity with a small free spectral range must be long, thus suffering from severe mechanical instabilities that would introduce noise at low frequencies. A common feature to Doppler-free spectroscopic techniques is that they require counter-propagating beams: the lack of efficient optical isolators in this spectral region makes this approach very hard, too.

The absorption from a molecular transition can be used instead of a resonator mode. In this case, strong absorption or sub-Doppler regimes are required to maximize the slope and thus the conversion factor. When dealing with lasers with limited tunability like distributed feedback QCLs it can happen (and this is our case) that strong absorptions from easily available gases cannot be found, thus making an efficient exploitation of this method impossible. Moreover, we address these issues with two different methods. The first one is a FNPSD direct measurement using a CaF_2 whispering gallery mode resonator that, thanks to its wide transparency range and its compact dimensions, does not suffer from drawbacks of classical Fabry-Perot cavities. The second linewidth measurement, following the

technique scketched in Section 3.4, exploits the molecular beam setup developed for high resolution spectroscopy, taking advantage of the narrow vibrational transition of carbon monoxide at 6 µm. This method yielded an upper limit of the laser linewidth almost an order of magnitude better than our previous result.

4.1 FNPSD measurement with a WGMR

To characterize the frequency noise of our Mid-IR source, we used a CaF_2 toroidal WGMR by *OEwaves, Inc.* It has a diameter of 3.6 mm (Figure 4.1) and two sapphire prisms allow evanescent wave coupling for both input and output beams.

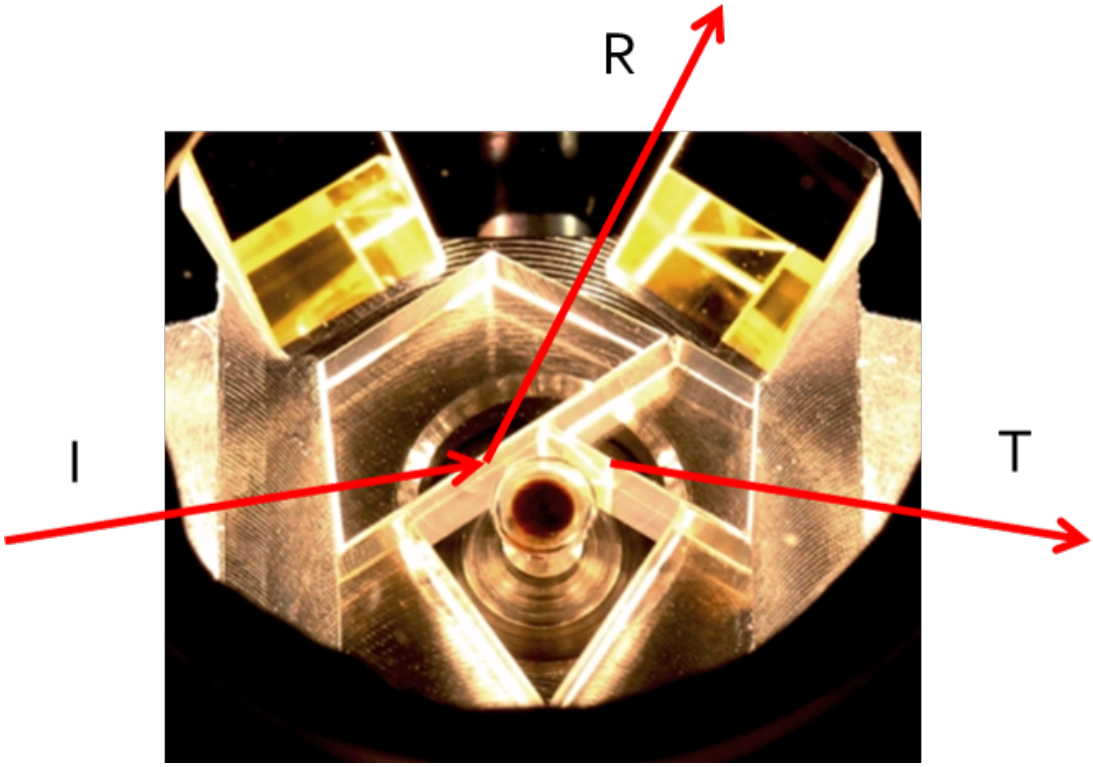

Figure 4.1: An upper view of the toroidal CaF_2 WGMR. It has 3.6 mm diameter, a FSR of about 19 GHz at 5.8 µm and both input and output beams are coupled via evanescent wave through two Al_2O_3 (sapphire) prisms.

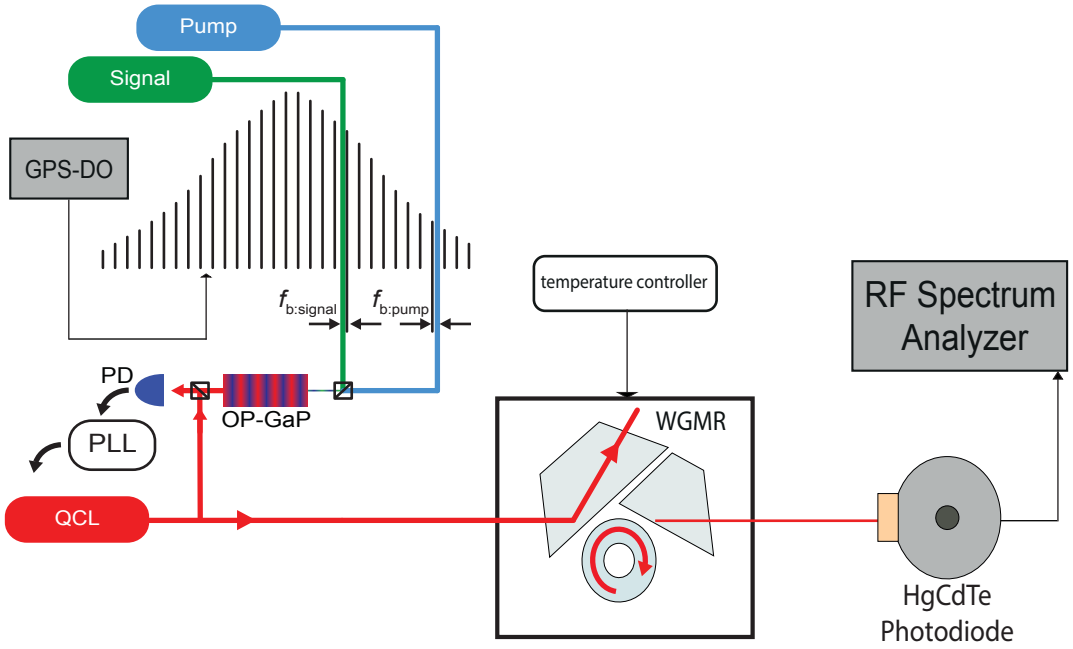

Figure 4.2: A sketch of the experimental setup. For the source spectral characterization, the optical frequency comb has been locked to a quartz oscillator disciplinated by a GPS as stable as 6×10^{-13} and with an accuracy of 2×10^{-12} at 1 s. Two near-IR lasers are locked to the closest comb's tooth, so that the frequency difference is stable and referenced. The 6 µm radiation is generated by difference frequency from this two near-IR lasers in an OP-GaP crystal. A quantum cascade laser is phase locked to this tiny amount of generated radiation (tens of μW). Light from the quantum cascade laser is then coupled into the WGMR. To tune and stabilize the selected resonator mode it is necessary to finely control the WGMR temperature. The output beam is then detected by a liquid-N_2-cooled HgCdTe photodiode, and the photocurrent is sent to a RF-spectrum analyzer.

This resonator has a free-spectral range of 19 GHz at 5.8 µm. The cavity mode can be tuned in frequency by several GHz by acting on the resonator temperature. In this way, a cavity mode that suits the frequency of the laser under investigation can be selected. The measured mode width at 5.8 µm is about 20 MHz FWHM, corresponding to a Q-factor of 3×10^6 and a finesse of about 1000. These values, although significantly worse than those recorded at 4.5 µm [20], due to the higher absorption of the material, are still noticeably high for this spectral region.

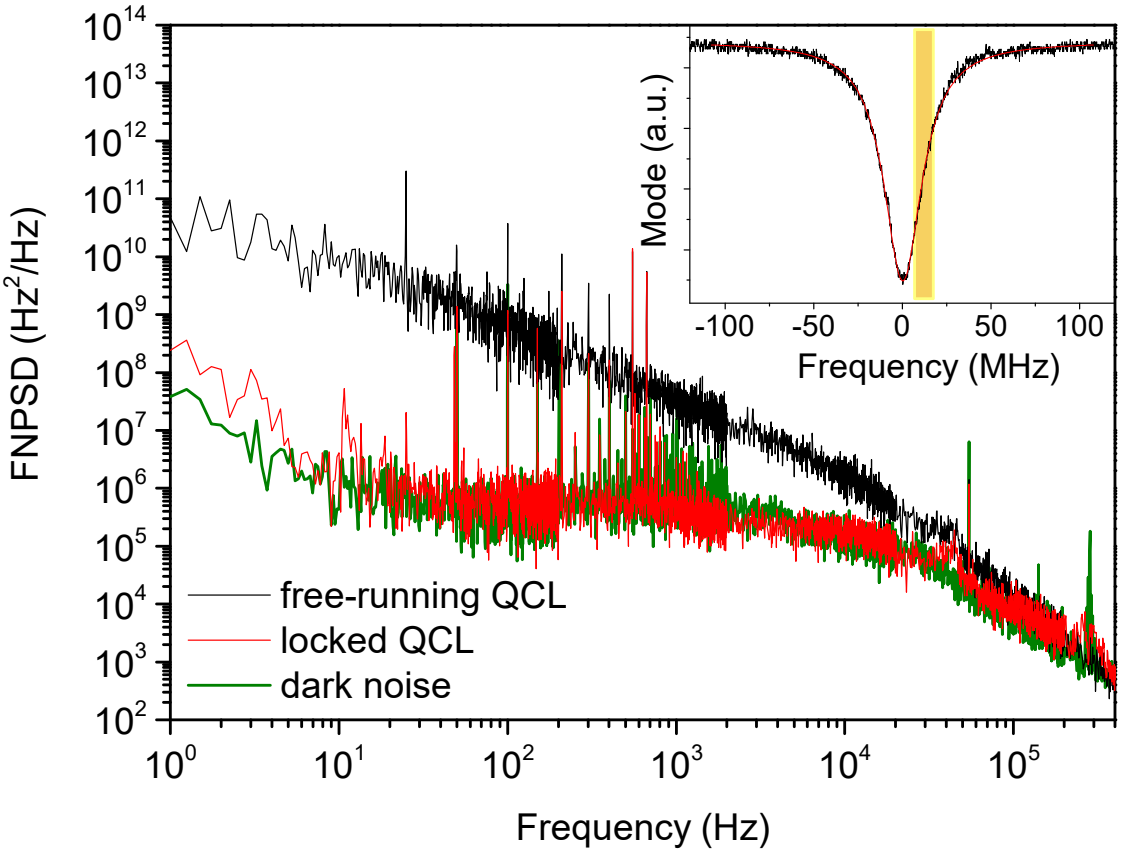

Figure 4.3: FNPSD of the 5.8 µm QCL in free-running (black trace) and locked (red trace) conditions. The green trace is the dark noise due to the detection electronics. Inset: transmission mode of the WGMR at 5.8 µm. A Lorentzian fit (red curve) is superimposed to the experimental trace, and the yellow bar shows the linear part of the slope used for noise measurements.

Figure 4.3 shows the FNPSD of the QCL both free running and phase-locked to the DF radiation, measured by using a WGMR as a frequency-to-amplitude converter. The inset shows the resonator mode, with a Lorentzian fit superimposed to the experimental trace, and the yellow area shows the linear part of the mode slope used as frequency-to-amplitude converter. The black trace in the figure is the FNPSD of the free-running QCL. The trace shows the dominating contribution due to flicker noise, in agreement with previous measurements. A numerical integration following ref. [28] gives a free-running linewidth of 2.1 MHz FWHM over 1 s timescale. The FNPSD of the locked QCL (red trace) cannot be significantly distinguished from the dark noise (green trace). Under these conditions, thus, our measurement can only set a rough upper limit for the linewidth of the locked QCL. After integration of the FNPSD signal for the locked QCL, we obtain a line width of about 700 kHz (FWHM over 1 s timescale). According to the calculations shown

in section 2.6.5, we expect a QCL linewidth about 2 orders of magnitude lower in locking conditions. At present, the limiting factor for this measurement is the detector noise. For the measurements shown in Figure 4.3, we used a liquid-N_2-cooled HgCdTe detector from Kolmar (KV104 series), with noise equivalent power NEP $= 2\times10^{-12}$ W/$\sqrt{\text{Hz}}$ and a bandwidth of about 100 MHz. We also have a Peltier-cooled detector from Vigo (PVI-4TE-6) with 10 MHz bandwidth and a similar NEP, but the noise measurements performed with the two detectors show no noticeable difference.The measurement could be possibly improved by increasing the power coupled to the micro-resonator, thus moving away from the background noise of the detector. In our present setup, the prisms used for evanescent-wave coupling (and extraction) of the light with the whispering-gallery modes of the resonator are made of sapphire, which has a very low transparency at 5.8 µm. BaF_2 prisms could be used instead of the sapphire ones. However, coupling large amount of optical power into the tiny volume of the modes, leads to large frequency instabilities and drifts of the modes, due to thermal effects and nonlinear processes, which should be avoided when a high stability is requested, as in frequency noise measurements. Therefore, it is not clear how much room for improvement there is in this direction.

4.2 Laser linewidth measurement on a CO molecular beam

Being unable to measure the linewidth of our source via conventional spectral analysis, we estimated the laser linewidth from the analysis of a molecular absorption line. This method is not a FNPSD measurement and the narrower the absorption line, the more precise the line width determination is. A careful evaluation of the molecular line broadening contribution is required, as well.

We measured the spectral linewidth of the Mid-IR radiation exploiting the sharp vibrational transition of metastable CO in a molecular supersonic beam. Carbon monoxide in the $a^3\Pi$ state has a strong vibrational transition at 5.85 µm. Following the method sketched in section 3.4, we scanned the laser frequency through the resonance, while recording the population of the excited state.

The experimental setup is sketched in Figure 2.3 (a), with the QCL propagation direction almost parallel to the molecular beam direction. While configuration (b) is suitable for Doppler shift compensation, I will show in the following that the quasi-parallel configuration allows us to minimize Doppler broadening of the absorption line.

The measured signal is the convolution between the laser linewidth and the molecular absorption profile: the most important required feature for this technique is the sharpness of the spectral line, so that the finite spectral width of the output signal can be attributed mainly to the laser linewidth.

4.2.1 Vibrational transition absorption linewidth

From our calculations (section 2.6.5), we expect the Mid-IR laser to be as narrow as a few kHz. We will now evaluate all the broadening contributions, summarized in section 3.3.3, that affect the molecular line absorption profile, and finally, the achievable spectral resolution.

Natural linewidth

The CO vibrational transition taken into account,

$$a^3\Pi_1 : |v = 0, j = 1, + > \rightarrow |v = 1, j = 1, - >, \tag{4.1}$$

involves two metastable states having 2.6 ms lifetime [32]. From equation (3.45) follows a natural linewidth of 66 Hz.

Doppler broadening

In this experimental configuration both excitation and ionization UV pulsed lasers intersect the molecular beam perpendicularly, while the Mid-IR laser and the molecular beam are overlapped under an angle of 0.054 rad ($\sim$ 3 degrees). We call z the direction of the molecular beam, x the vertical direction and y is given by the choice of a right-handed system of coordinates (Figure 4.4).

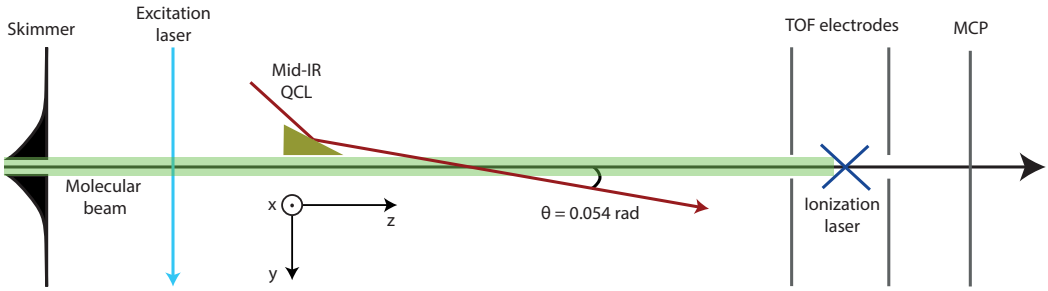

Figure 4.4: A schematic view of the quasi-collinear configuration. The molecular beam travels along the z axis and, with respect to the QCL propagation direction, makes an angle of 0.054 rad ($\sim$ 3 degrees). The relevant component of molecule velocity for Doppler effect is the one along the laser's propagation direction, so a 5% contribution coming from $\sin(\theta)$ must be added to the Δv_z simulated (Figure 4.7) and evaluated with the formula (4.2).

The v_z velocity interval selected by the two UV lasers depends on the shape of their beam profiles and on the time delay between them, according to the simple formula

$$\Delta v_z = \frac{2(r_{\text{excitation}} + r_{\text{ionization}})}{\Delta t} \tag{4.2}$$

where r are the radii of the two lasers in the region where they interact with the molecular beam. The characterization of the transverse spatial profile (Figure 4.5) of both excitation and ionization lasers has been performed with the knife-edge method (for details see Appendix A), while the time delay between the two is a parameter known within tens of ns.

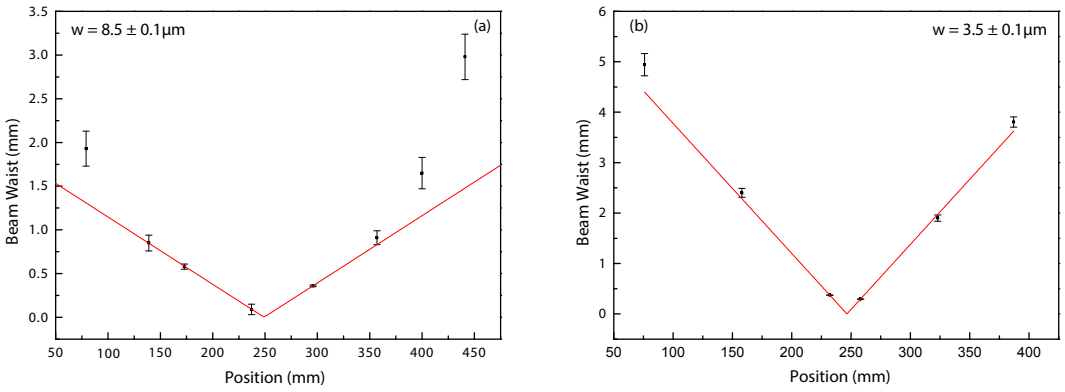

Figure 4.5: Excitation (a) and ionization (b) UV lasers waist measurement performed with the knife-edge method. Far from the waist position, the model (red curve) does not suitably reproduce the data. This is probably due to the spatial mode of the beams, that are far from being TEM_{00}. Anyway, it is still possible to give an upper limit to the beam waist of few microns and to give a first estimation of the waist position, while the fine alignment with the molecular beam has been done minimizing the spectral width of the output signal.

Figure 4.6 shows how the excitation laser selects a subset of molecules in the z-v_z phase-space plane among those present in the beam (a). The molecular cloud propagates toward larger z, with the rotation characteristic of free motion (b). By the time the molecules reach the ionization laser, their distribution is such that only a very narrow velocity interval is addressed by the laser and thus detected.

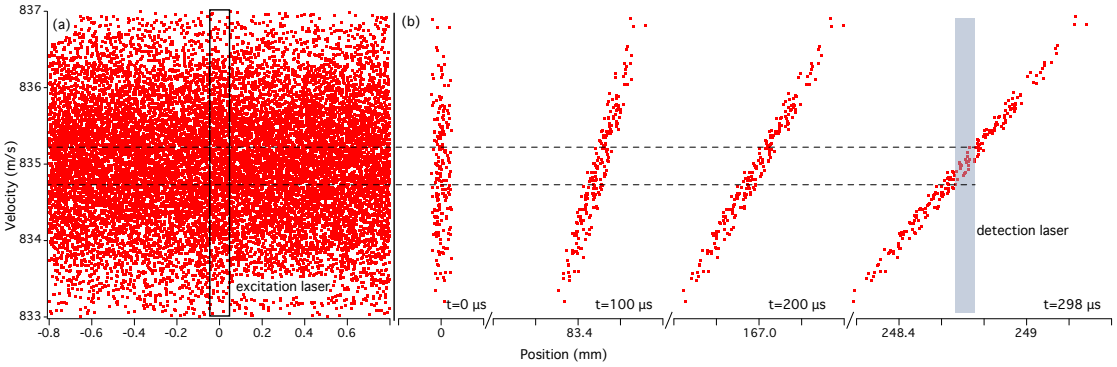

Figure 4.6: Molecular distribution in the z-v_z plane of the phase space in the experiment. (a) The excitation laser selects a set of molecules out of the initial distribution. (b) Time evolution of the molecular cloud until it reaches the ionization laser. Only molecules in a very narrow velocity range are detected.

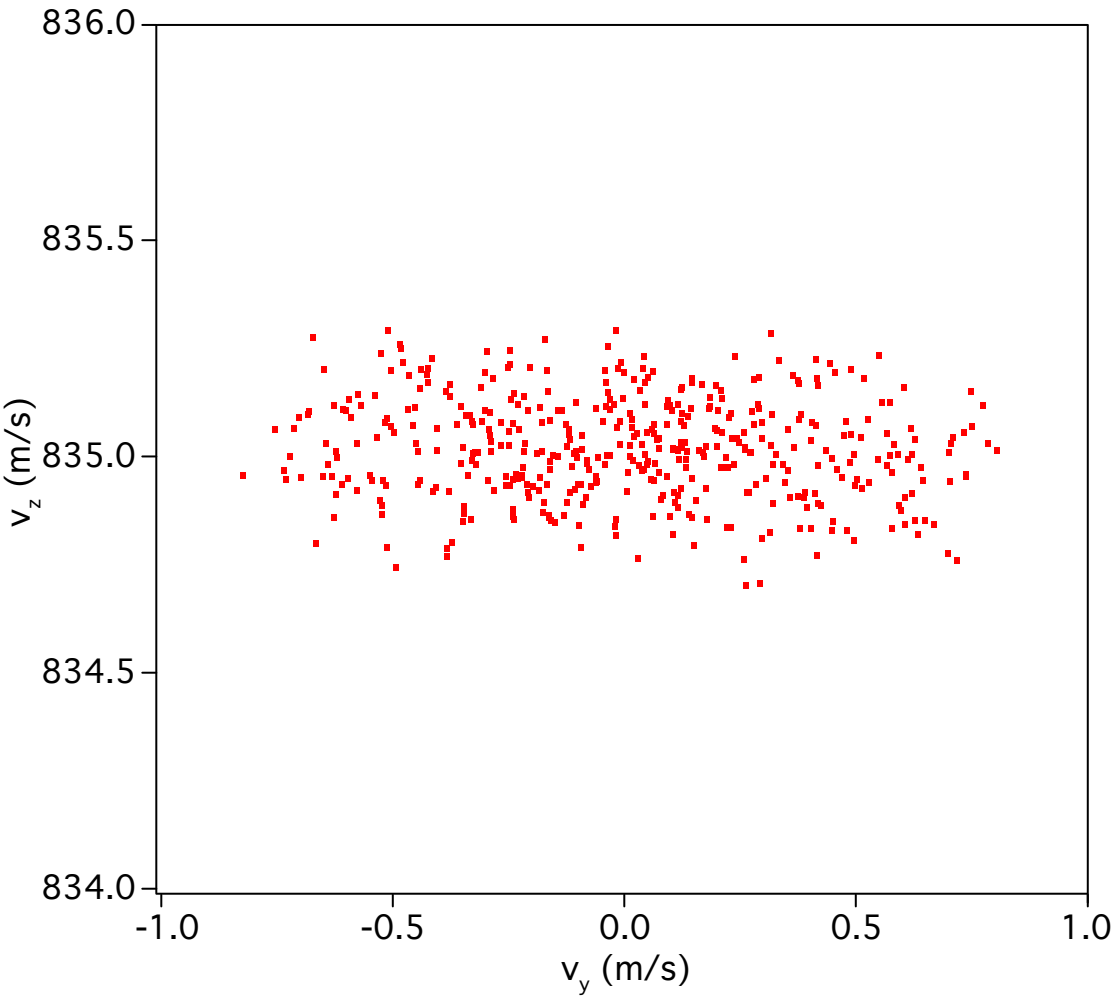

Figure 4.7: Molecular distribution in the v_y-v_z plane of the phase space in the experiment. The distribution shows that the v_z distribution is much narrower than v_y.

Figure 4.7 compares the v_y and v_z velocity components of the molecules that contribute to the signal under actual experimental conditions. This molecular distribution is due to the apertures that collimate the beam (in the x and y directions) and to the focused pulsed lasers (in the z direction). We see that the v_z component is four times narrower than the v_y component. In the previous configuration, (Figure 2.3 a), we were able to minimize any induced Doppler shift thanks to the retro-reflecting corner mirrors, while the quasi-collinear configuration allows us to exploit the potentially lower Doppler broadening. The relevant velocity component that contributes to Doppler broadening is the one along the molecular beam (plus a $\sim$5% contribution of the velocity in the plane of the laser and the molecular beam due to the θ angle, Figure 4.4). This yields a fourfold improvement in the resolution

for the quasi-collinear configuration, compared to 900 kHz Doppler broadening we measured [35]. For the actual setup, a Doppler broadening contribution of about 85 kHz has been estimated.

Transit time broadening

The Mid-IR beam and the molecular beam are overlapped under an angle of 0.054 rad($\sim$ 3 degrees), therefrom the interaction region is $\sim$ 80 mm long. Nonetheless, we limited the interaction time to 20 µs, corresponding to 16.7 mm interaction region for a molecular beam with $\sim$800 m/s velocity. We do this to reduce the magnetic field inhomogeneity, as it will be shown in the following. We achieve this with two equivalent methods: either we Stark-shift the transition out of resonance by applying a strong electric field, or we rapidly modulate the laser frequency; in the first case we apply 500 V voltage to two electrodes previously mounted in the middle of the second vacuum chamber, in the Mid-IR/molecules interaction region. Voltage rise and fall times are lower than 60 ns, thanks to two fast high voltage switches (Behlke hts 31-03-gsm), so that we can finely control the interaction time bringing the transition out of resonance. In the second case, the resonance condition is suppressed by working on the QCL, specifically acting on the local oscillator of the phase lock loop (see section 2.6). The frequency change of the generator can be considered to be instantaneous, for our characteristic timescale, and the phase lock loop is fast enough to "switch" on and off the transition, changing the laser frequency within tens of ns. The low pass filter of the phase lock loop between the referenced DF radiation generated in the OP-GaP crystal and the quantum cascade laser limits the loop bandwidth to 300 kHz, as it can be seen from the servo bumps in Figure 2.9 d). In both cases, the resonance condition is suppressed before and after the desired interaction time interval. We observe no difference in the measured signal between these two methods and, according to equation (3.56), the transit time broadening is thus limited to 45 kHz.

Magnetic field inhomogeneity

In principle, the higher the interaction time the lower the transit time broadening (and the higher the signal to noise ratio), but there is a major drawback. A long interaction time implies an extended interaction region, even though inhomogeneities of electrical or magnetic field have to be taken into account and considered as an additional source of line broadening: whereas the electric field is naturally shielded by the vacuum chamber, the magnetic field plays an important role because of the Zeeman shift of the involved states. On the $a^3\Pi_1$ electronic state of CO, we excite the vibrational transition from the upper component of the lambda doubling of $\nu = 0$, J = 1, positive parity, to the lower component of $\nu = 1$, J = 1, negative parity. Selection rules only allow $\Delta M = 0, \pm 1$. Transitions with $\Delta M = 0$

are less sensitive to the magnetic field, about 12 kHz/G, but are close together at low-to-moderate fields (Figure 4.8), whereas the Zeeman shift of the transitions with $\Delta M = \pm 1$ is about 500 kHz/G.

In this section, we report simulated and measured magnetic flux density using the G, a CGS unit. The proper SI unit is the Tesla (T),

$$1G = 1 \times 10^{-4} T \tag{4.3}$$

but, for an easier comparison with Zeeman splittings values reported in literature, we make this exception.

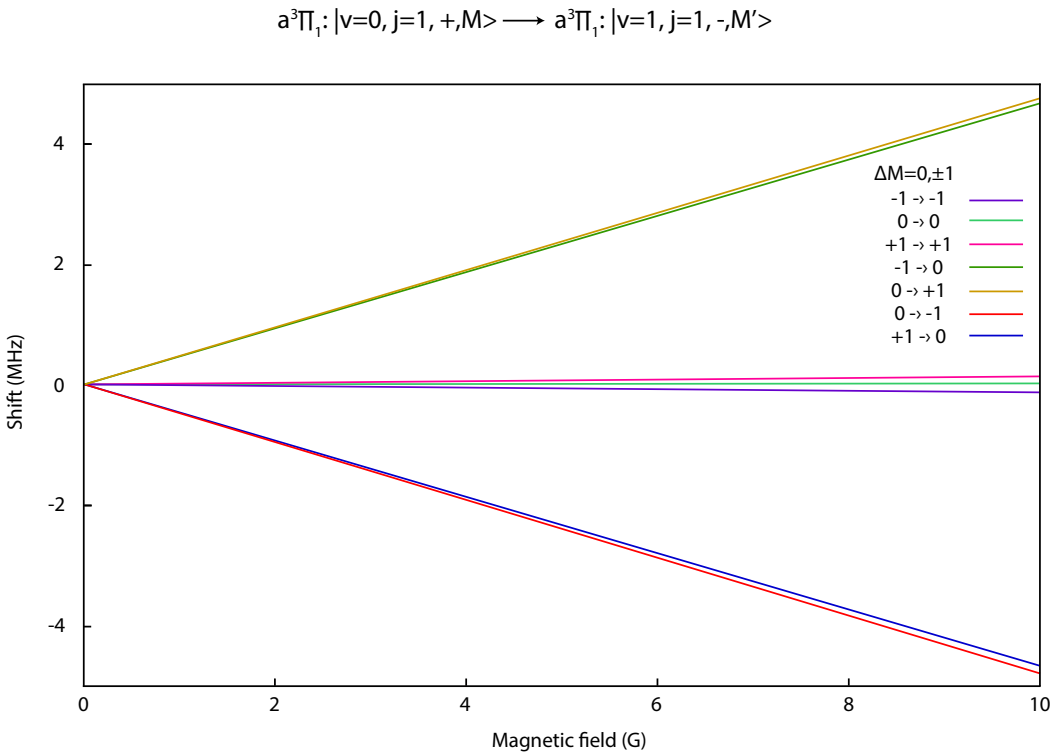

Figure 4.8: Simulated Zeeman splitting of the transition $a^3\Pi_1 : |v = 0, j = 1, + > \rightarrow |v = 1, j = 1, - >$. Transitions with $\Delta M \neq 0, \pm 1$ are forbidden by selection rules. The Zeeman shift of the $\Delta M = 0$ is about 12 kHz/G , whereas $\Delta M = \pm 1$ transitions experience a shift of about 500 kHz/G. Simulations from [62].

As suggested by simulations, our first idea was to apply a magnetic field strong enough to observe a signal coming from a single $\Delta M = 0$ transition. To have at least 1 MHz splitting between each line, we should generate more than 100 G in the interaction region, so the choice fell on two strong permanent magnets, two

parallelepipeds of 60x7x100 mm and a magnetization of 1.04×10^6 A/m, placed inside the vacuum chamber thanks to specifically designed holders. We measured the field in the interaction region by looking at the splitting between the three $\Delta M = 0$ transitions for a distance of 27, 40 and 66 mm between the two magnets (Figure 4.10). In good agreement with the simulations (Figure 4.8), the transitions $+1 \rightarrow +1$ and -1 $\rightarrow$ -1 experience a shift of about 12 kHz/G, while the central one is nearly insensitive to magnetic field.

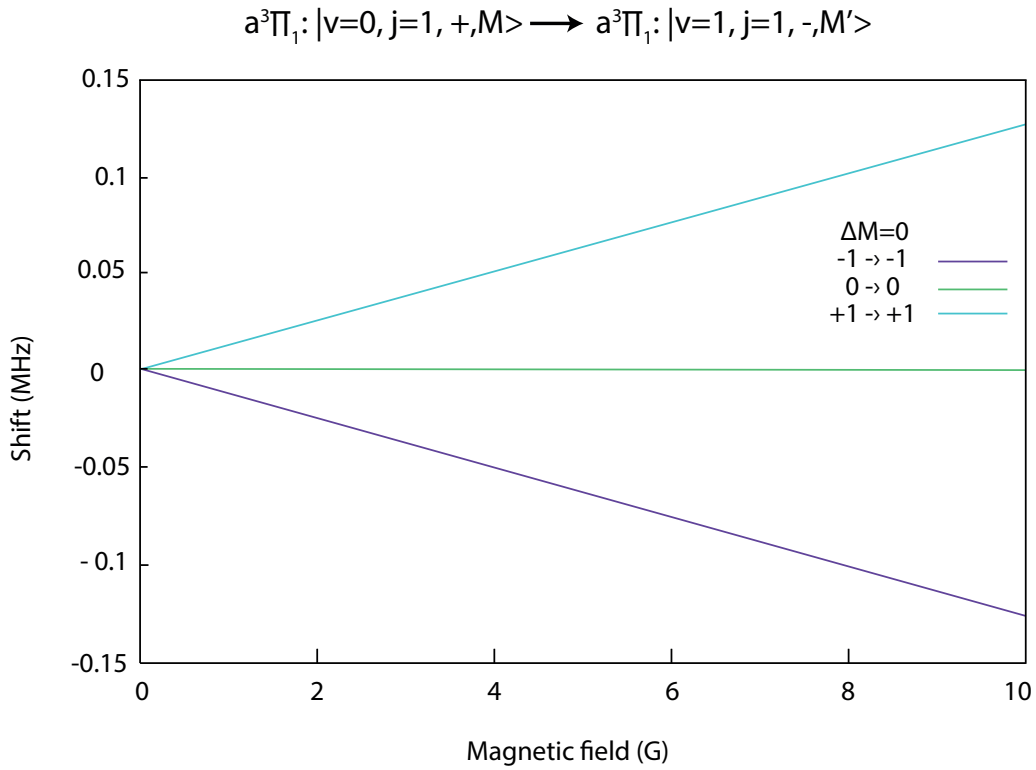

Figure 4.9: A detail of the simulated Zeeman splitting of the $\Delta M = 0$ transitions. $a^3\Pi_1 : |v = 0, j = 1, +, 0 > \rightarrow |v = 1, j = 1, -, 0 >$ is nearly insensitive to the magnetic field while $a^3\Pi_1 : |v = 0, j = 1, +, \pm 1 > \rightarrow |v = 1, j = 1, -, \pm 1 >$ experience both a shift of 12 kHz/G. Simulations from [62].

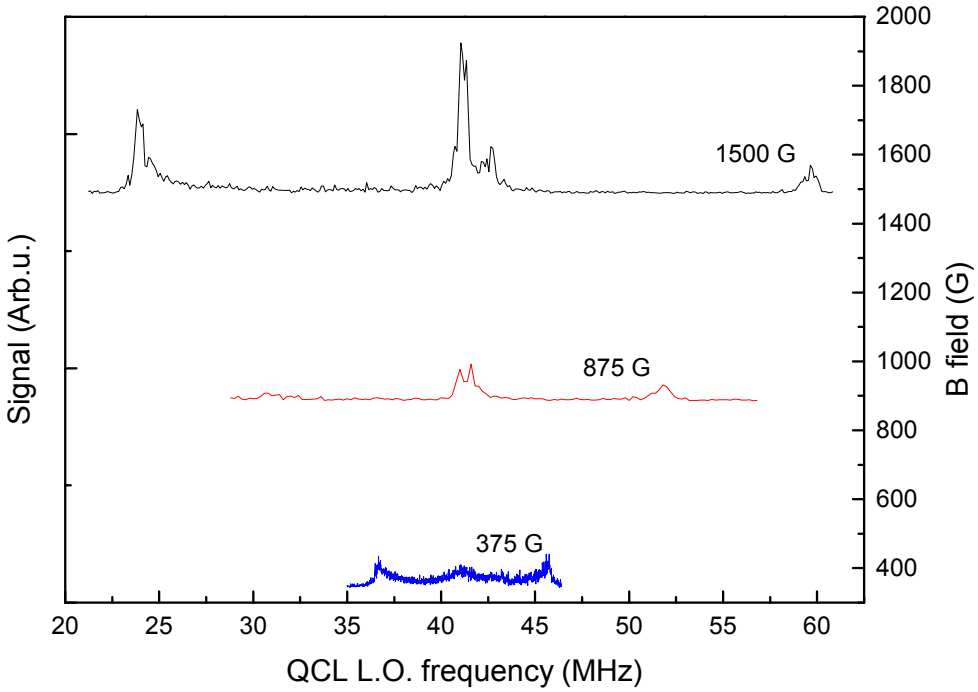

Figure 4.10: We measured the splitting between the $\Delta M = 0$ transitions for three different values of the magnets distance. According to our simulations, we measured a shift of 12 kHz/G for the two $\Delta M = \pm 1$ while the central peak experiences no shift.

The central peak corresponds to $0 \rightarrow 0$, a transition that should be forbidden by selection rules. We were not able to explain why we can actually measure this transition, and why, in the presence of an intense magnetic field (the trace acquired with 1500 G in Figure 4.10), it gives rise to the strongest signal.

We simulated the magnetic field with the finite element software COMSOL Multiphysics in the three different experimental configurations, 27, 40 and 66 mm distance. We were looking for the best compromise between field strenght, to have a sufficient spacing between transitions, and field regularity, to avoid broadening the absorption line profile by the Zeeman effect. It appears that the trade-off is obtained for 39 mm distance between the magnets, where we have a field as regular as 60 G (Figure 4.11) on 20 mm, a typical value for the interaction region lenght.

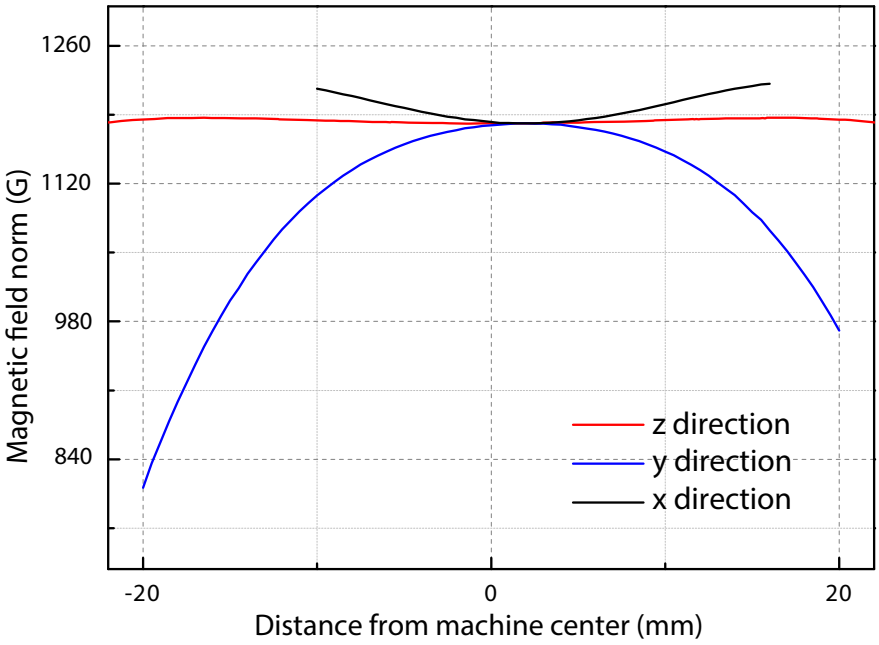

Figure 4.11: Finite element simulation of the magnetic field of two permanent magnets placed at 39 mm distance in the vacuum chamber.

The strong variation of the magnetic field in the interaction region induces in the two lateral peaks a significant broadening, because of their Zeeman shift. Our simulations assess that the central peak should not be broadened, but we measured (Figure 4.12) a signal having more than 800 kHz FWHM.

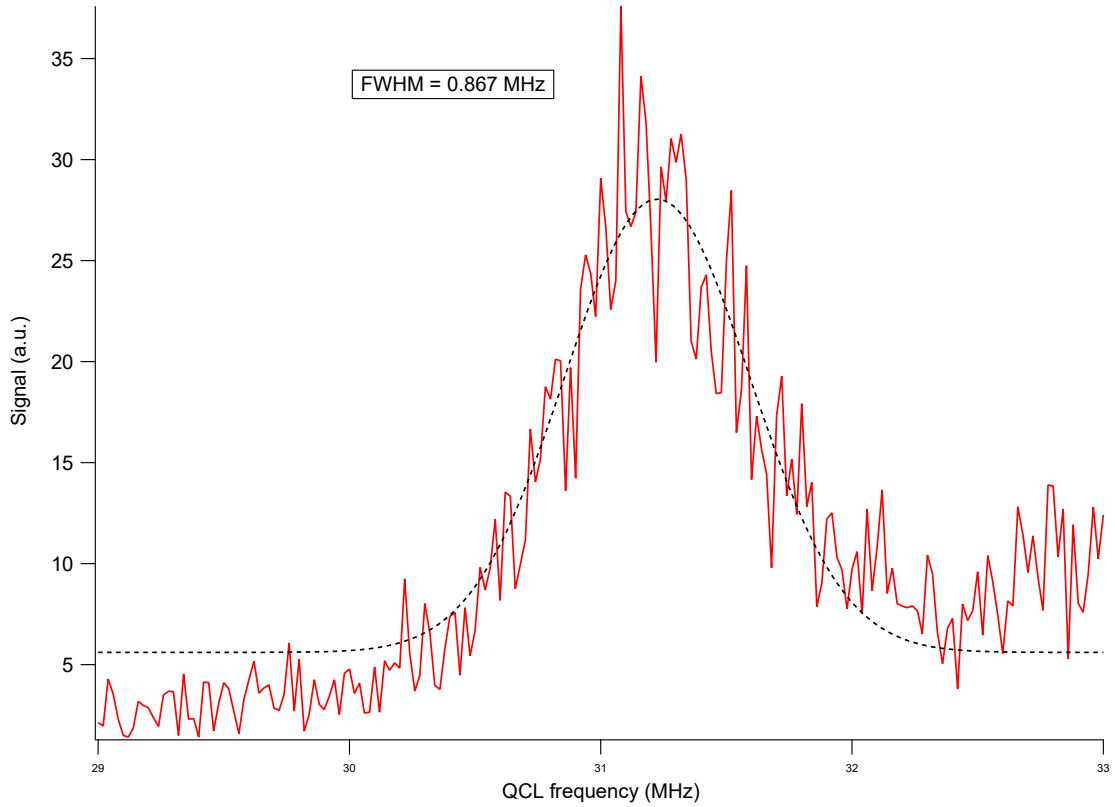

Figure 4.12: Transition $a^3\Pi_1 : |v = 0, j = 1, +, 0 > \rightarrow |v = 1, j = 1, -, 0 >$, with a magnetic field of 875 G in the interaction region. Despite the low SNR of this measurement, we measured a broadened peak with a FWHM of more than 800 kHz.

This broadened profile, together with the presence itself of this peak, that should correspond to a forbidden transition, convinced us to move towards more regular although less intense magnetic fields. We simulated the field of three pairs of coils, in a quasi-Helmholtz configuration. Each coil is made up of 20 windings of isolated copper wire and the pairs are placed right outside of the vacuum chamber along the x, y, and z axis. Our simulations indicate that for small magnetic fields we can control its strength within 50 mG (Figure 4.14) along the interaction region.

We measured the splitting of the $\Delta M = 0, \pm 1$ transitions for several values of the coils current and, in good agreement with the simulations, we can assess that, in a moderate magnetic field regime of 4.5 G, the $\Delta M = \pm 1$ transitions are split from $\Delta M = 0$ of about 2.5 MHz each (Figure 4.13).

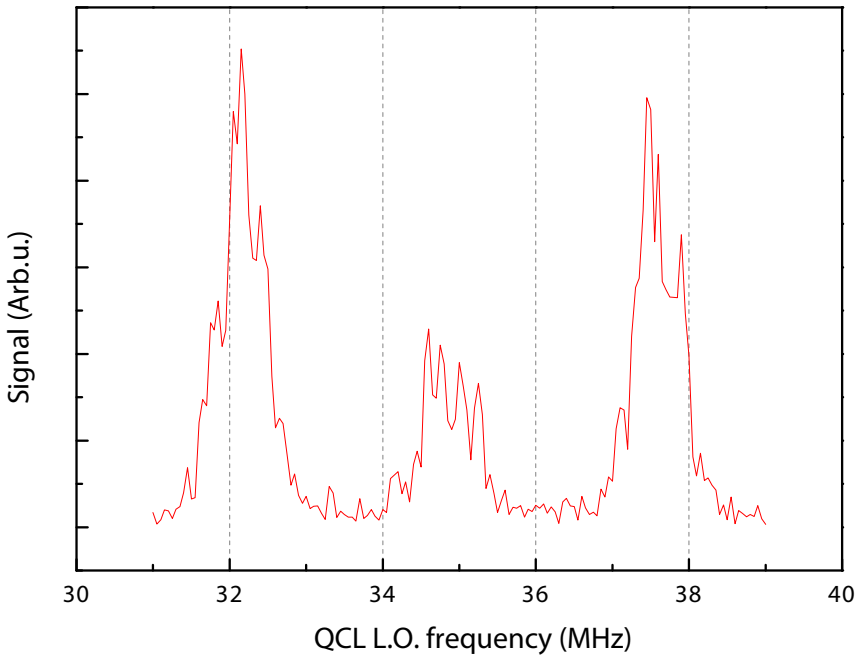

Figure 4.13: $|v = 1, j = 1, - >$ state population as a function of the Mid-IR laser frequency, in a moderate 4.5 G magnetic field regime. The field is generated by three couples of coils in quasi-Helmholtz configuration. The central peak corresponds to the three collapsed $\Delta M = 0$ transitions, while the others to the $\Delta M \pm 1$. The distance between the peaks is in good agreement with the Zeeman splitting predicted by our simulations.

The contribution of the 50-mG inhomogeneity in the magnetic field is well below the contribution from the Doppler effect, for all kinds of transitions. We chose to use a $\Delta M = +1$ transition because, at the moderate field strength of 4.5 G, it is well separated from all other transitions, whereas the $\Delta M = 0$ transitions are close to each other, making data interpretation more complex.

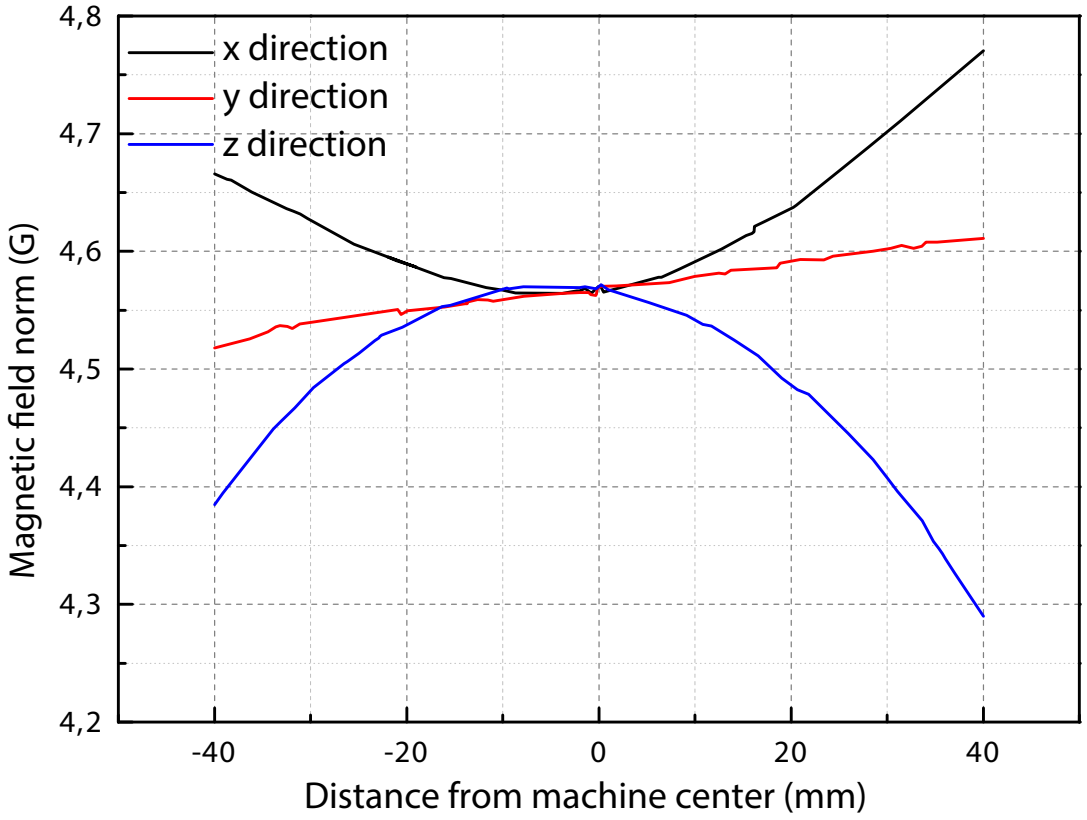

Figure 4.14: The interaction time is set precisely at 20 µs, during which molecules at an average speed of 835 m/s cover 16.7 mm. Our simulation indicates that a moderate magnetic field of about 4.5 G can be, within 20 mm, as regular as 50 mG.

4.2.2 Line width determination

In Figure 4.15 a high resolution scan of the Mid-IR laser frequency is reported over the $a^3\Pi_1 : |v = 0, j = 1, + > \rightarrow |v = 1, j = 1, - >$ CO rovibrational transition. The waist positions of the excitation and the ionization lasers have been finely aligned on the molecular beam by minimizing the width of the output signal. The signal is best fitted by a triple Lorentzian function, where the FWHM of the central peak is 177 $\pm$ 10 kHz. Overimposed to the experimental data and the fit, in Figure 4.15, is reported also the beat-note between the QCL and the DF radiation: we attribute the three peaks structure of the output signal to the $\sim$ 30 % optical power that is not channelled into the DF mode (Section 2.6.6). This hypothesis is sustained by the correspondence between the measured peaks distances and the distance between the beatnote and the servo bumps of the QCL-DF radiation phase lock.

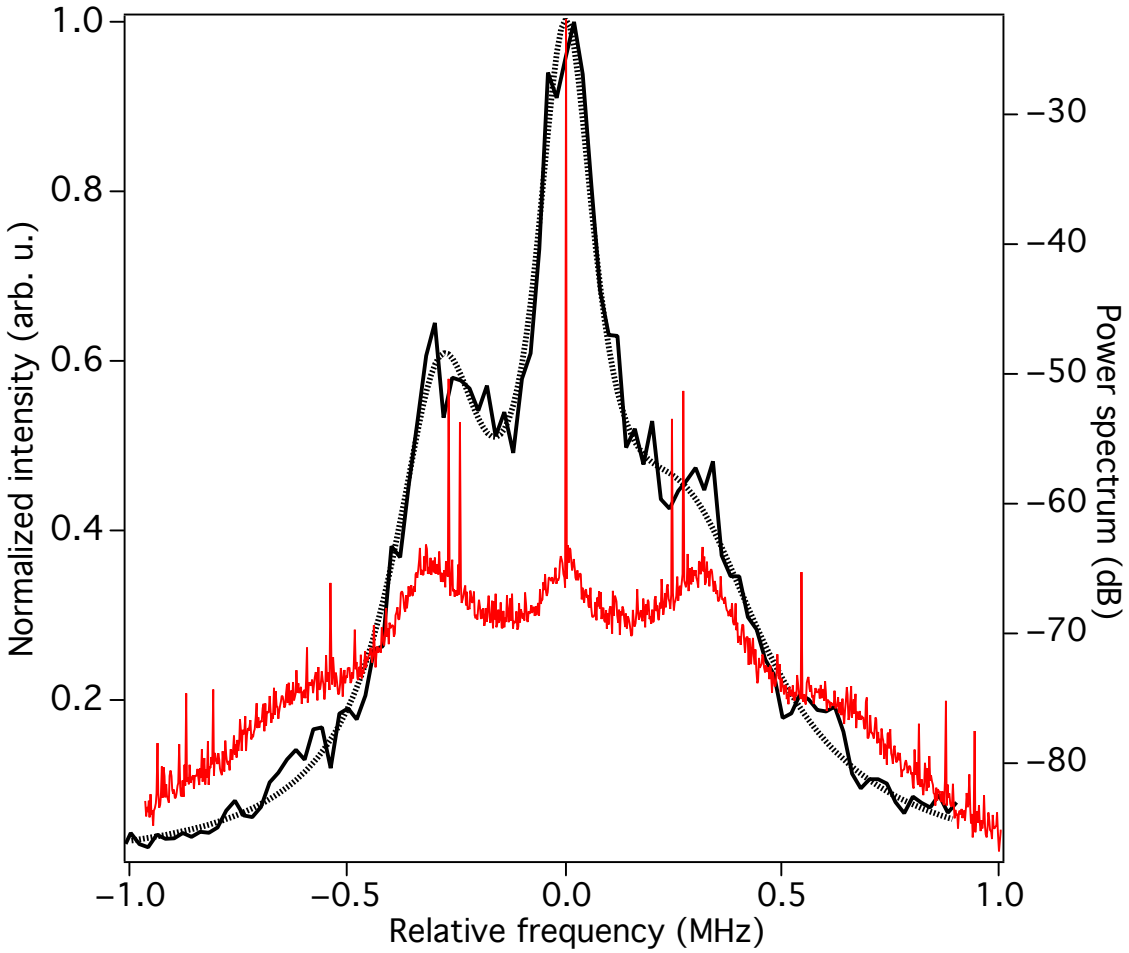

Figure 4.15: Frequency scan of the QCL over the rovibrational molecular transition. Solid black line: ion counts generated by resonant ionization from the vibrationally excited state. Dashed line: fit of a triple Lorentzian function. The best fit is obtained for a Lorentzian width of the central peak of 177 kHz. Solid red line: beat-note power spectrum between the QCL and the DF radiation, in locking conditions

A brief summary of all the main contributions to the line broadening is reported in table 4.1, together with an estimation of the laser linewidth. From a FNPSD measurement and from a numerical integration, the linewidth of the DF radiation results to be 2.3 kHz. We evaluated the effectiveness of the phase-lock of the QCL to this reference to be as high as 70%, thus we expect a QCL as narrow as few kHz. Although we are clearly still limited by the Doppler broadening of the CO vibrational transition, this measurement brings to an improvement of almost an order of magnitude in the laser linewidth determination with respect to our previous measurement [35].

Natural Linewidth	66 Hz
Doppler Broadening	85 kHz
Transit Time Broadening	45 kHz
Magnetic Field Inhomogeneity	25 kHz
Estimated laser linewidth	2.3 kHz

Table 4.1: A summary of the main broadening contributions to the absorption line corresponding to the CO vibrational transition $a^3\Pi_1 : |v = 0, j = 1, + > \rightarrow |v = 1, j = 1, - >$, when a magnetic field of 4.5 G as regular as 50 mG is applied. The final linewidth estimation is based on the noise analysis of the reference DF radiation, to which our QCL laser is phase-locked.

Chapter 5

Conclusions and Future Perspectives

My PhD research activity is mainly focused on high resolution spectroscopy in molecular beams. The preliminary step, to which I contributed at the beginning of my PhD, is the measurement of a vibrational transition of metastable CO with 11 digits of precision [35]. That result, improving the precision of previous measurements by 4 orders of magnitude [23], was possible thanks to a narrow linewidth frequency stabilized Mid-IR QCL linked to the Cs frequency standard.

Thanks to my work, the resolution of the spectroscopic measurements was improved by almost one order of magnitude. This was possible by working on the reduction of the residual Doppler broadening and by improving the frequency stabilization of the QCL. Thanks to the higher resolution, the spectral characterization of the Mid-IR source was possible.

As the main final result, recording of the molecular transition with a linewidth of 177 $\pm$ 10 kHz was possible, almost limited by the transit-time broadening. An upper limit to the stabilized QCL linewidth of few tens of kHz could be set, about one order of magnitude better than that achievable with more standard methods.

To reduce Doppler broadening, I made the molecules direction and the QCL laser propagation vector almost collinear, to exploit the limited velocity spread along the molecular beam propagation axis. In this quasi-collinear configuration, the timing of the pulsed lasers is well known while their precise positions is not. Therefore, the velocity component of the molecular beam that is parallel to the Mid-IR radiation direction is only roughly known and so is the Doppler shift. Thus, the precision of this measurement comes at the cost of its accuracy.

The resolution limit in this setup configuration is given by the Doppler broadening of the absorption line, that is $\sim$ 85 kHz. Resolution can be improved by reducing the UV lasers beam sizes and/or increasing the time delay between the two pulses. The latter action can be performed either by slowing down the molecules or by increasing the distance between the two lasers. Either way, however, the number

of detected molecules decreases, thus reducing the signal-to-noise ratio.

One of the interesting possibilities offered by the quasi-parallel configuration of the molecular and laser beams in our apparatus is the characterization of the QCL spatial profile: if we add a set of electrostatic lenses and a phosphore screen on the back of the MCP, we obtain an image of the distribution of the excited molecules, from which we can extract information on the laser beam profile and on the molecular beam. A good laser beam spatial profile is crucial, for example, in experiments where efficient coupling with an optical resonator is required, or for the study of coherent effects, where high regularity of the phase fronts is mandatory. From early calculations, we predict that such a system could have 100 µm resolution, in line with commercially available, though expensive, IR cameras.

A natural future development would be implementation of an intrinsic Doppler-free experiment, such as two photon spectroscopy. This was not possible till now because of the poor quality of optical isolators, which also introduce significant losses in the available optical power for spectroscopy. Quantum cascade lasers with an optical power up to the Watt level have already been demonstrated around 4 µm [45], and devices emitting hundreds of mW are now commercially available also for some wavelengths above 5 microns. Also technological research on materials is running fast, and we believe that better optical components for the Mid-IR will be soon available. Moreover, on the basis of our experience, smart solutions for optical isolation can be adopted with a high-power QCL, providing at the same time protection of the laser from optical feedback and sufficient power levels for two-photon spectroscopy.

If some improvements are expected from better spectroscopic techniques, a dramatic enhancement both for precision and accuracy of molecular absorption lines measurements would be ensured by a colder and slower molecular sample. To date, only few molecules have been cooled down to sub-mK temperatures but the field of ultracold molecules is rapidly growing as biatomic molecules like SrF [5] and CaF [1, 70], polyatomic molecules like SrOH [38] and dimers formed by pre-cooled atoms [48, 57], have been successfully cooled to the ultracold regime. Moreover, the possibility of laser cooling of simple molecules is the main research field of well-known groups worldwide, and the general feeling in the cold-molecule community is that the goal will be reached in just a few years. We strongly believe that this is the road which will allow to open new fascinating and still unexplored horizons.

Appendix A

Knife-edge method

A laser beam propagating in the z direction and characterized by a TEM_{00} mode has a transversal intensity distribution that can be described by a Gaussian function

$$I(r,z) = I_0 \left(\frac{w_0}{w(z)} \right)^2 e^{-\frac{2r^2}{w(z)^2}} \tag{A.1}$$

where I_0 is the intensity on the optical axis, w_0 is the minimum beam radius also known as waist, r is the radial coordinate and $w(z)$ is the beam radius, defined as the distance from the optical axis where the intensity drops to $1/e^2$ of its axial value. The beam diameter $2w(z)$, according to this definition, is 1.7 times larger than the FWHM.

At a certain position along the propagation axis z the beam radius is given by

$$w(z) = w_0 \sqrt{1 + \left(\frac{z - z_0}{z_R} \right)^2} \tag{A.2}$$

where z_R is generally known as Rayleigh distance and it is the distance where the area of the spot is twice the area of the spot at the beam waist position, z_0. It is given by

$$z_R = \frac{\pi w_0^2}{\lambda}. \tag{A.3}$$

If we assume our definition of beam radius, far from the waist position it linearly increases with z (Figure A.1). The beam divergence θ_0 is strictly related to the beam waist through the relation

$$\theta_0 = \frac{\lambda_0}{\pi n w_0} \tag{A.4}$$

where λ_0 is the wavelength in vacuum and n is the refractive index of the medium where the beam propagates.

The basic principle of the knife edge method is quite simple: with a sharp razor blade mounted on a translational stage the beam is progressively covered, while

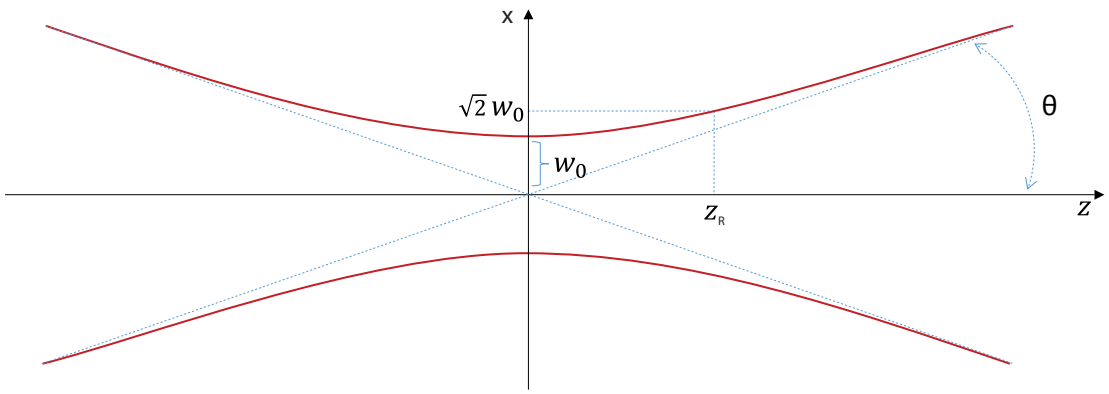

Figure A.1: A Gaussian beam propagating along the direction z, with a divergence θ_0 a beam waist w_0 and Rayleigh distance z_R.

the transmitted power is measured with a photodiode. A typical measurement of a laser intensity profile is showed in Figure A.3. To calculate the beam radius w at this particular $z*$ position, data are fitted with the function

$$P(z*) = P_{\text{off}} + \frac{P_{\max}}{2}[1 - \text{erf}(\sqrt{2}(x - x_0)/w(z*))] \tag{A.5}$$

where the fit parameters are P_{off} and $P_{\max}$ that are respectively an offset and the maximum power, x_0 that is the shift along the x axis where the measured power drops to half the maximum value, and $w(z*)$ that is the beam radius. Repeating this measurement for several positions of the blade along the z axis one obtains $w(z)$, that can be fitted by the A.2 to calculate the beam waist w_0.

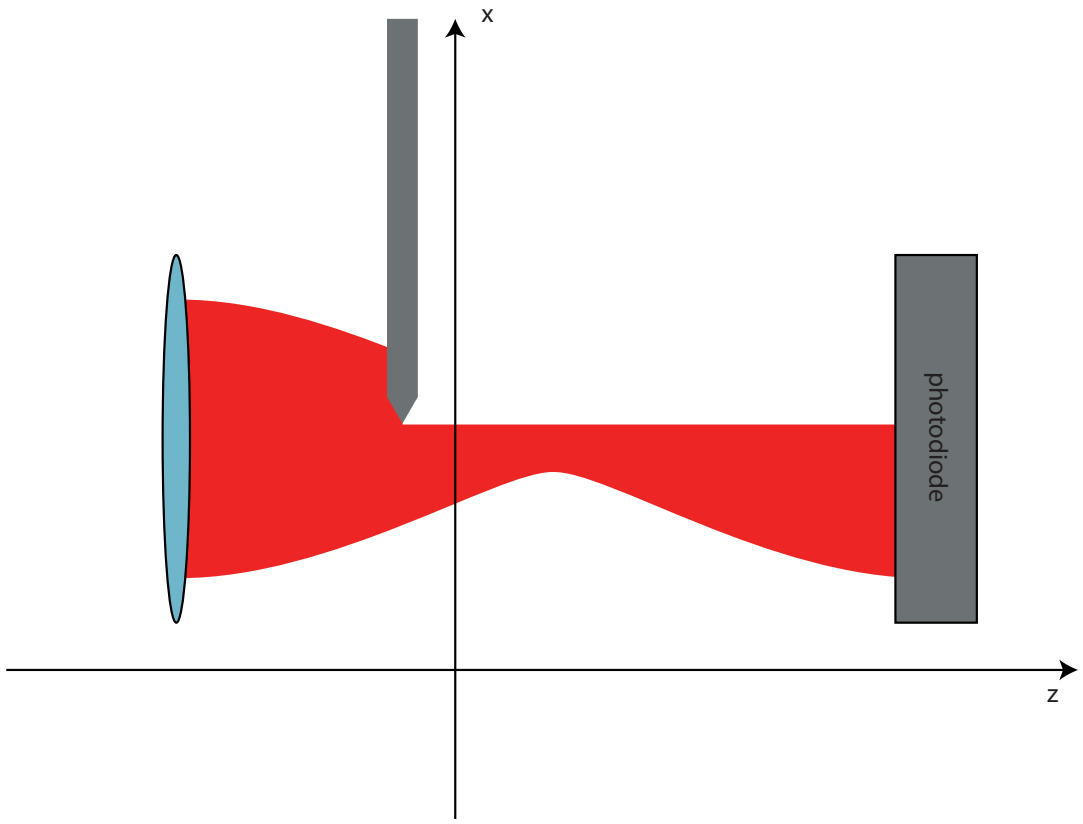

Figure A.2: A razor blade on a micrometric translational stage cuts the laser beam along the x direction, and a photodiode registers the intensity profile. This data, acquired for several positions along the z axis, can be fitted by the equation (A.2) to give an estimation of the beam waist and its position.

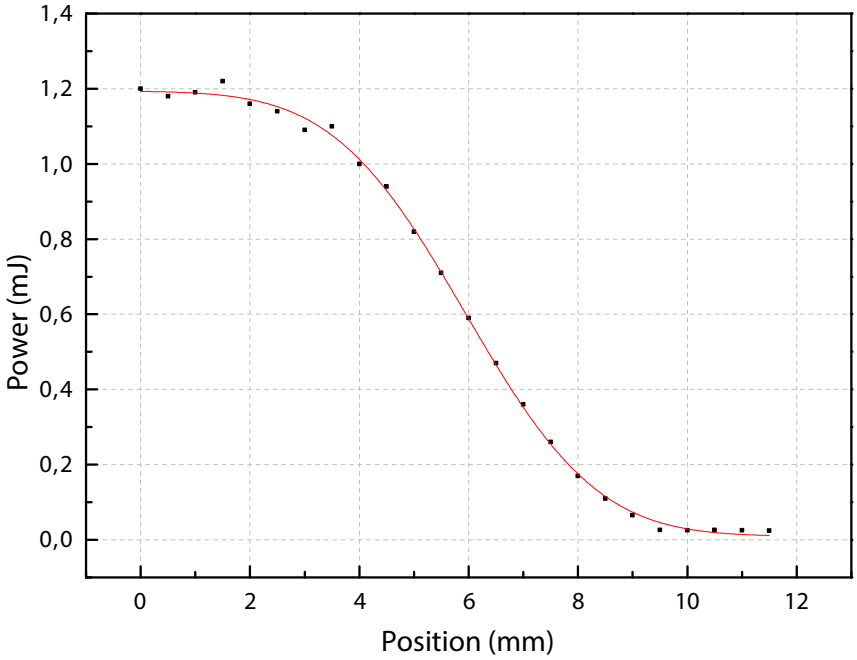

Figure A.3: A typical recording of the measured power as a function of the blade position along the x axis. This measurement is part of the characterization of the ionization UV pulsed laser (283 nm wavelenght), taken at a distance of 387 mm from the focusing lens (f = 300 mm). From the fit (red curve) of this experimental data (dots) we calculated a beam radius of 3.8 ± 0.5 mm.

References

[1] L. Anderegg et al. “Laser cooling of optically trapped molecules”. In: *Nature Phys.* n (2018), n. DOI: 10.1038/s41567-018-0191-z.

[2] B. Argence et al. “Quantum cascade laser frequency stabilization at the sub-Hz level”. In: *Nature Phot.* 9 (2015), p. 456. DOI: 10.1038/nphoton.2015.93.

[3] J. Bagdonaite et al. “A Stringent Limit on a Drifting Proton-to-Electron Mass Ratio from Alcohol in the Early Universe”. In: *Science* 339 (2013), p. 46. DOI: 10.1126/science.1224898.

[4] J. Bagdonaite et al. “Constraint on a Varying Proton-Electron Mass Ratio 1.5 Billion Years after the Big Bang”. In: *Phys. Rev. Lett.* 114 (2015), p. 071301. DOI: 10.1103/PhysRevLett.114.071301.

[5] J. F. Barry et al. “Magneto-optical trapping of a diatomic molecule”. In: *Nature* 512 (2014), p. 286. DOI: 10.1038/nature13634.

[6] S. Bartalini et al. “Measuring frequency noise and intrinsic linewidth of a room-temperature DFB quantum cascade laser”. In: *Opt. Express* 19 (2011), p. 17996. DOI: 10.1364/OE.19.017996.

[7] S. Bartalini et al. “Observing the Intrinsic Linewidth of a Quantum-Cascade Laser: Beyond the Schawlow-Townes Limit”. In: *Phys. Rev. Lett.* 104 (2010), p. 083904. DOI: 10.1103/PhysRevLett.104.083904.

[8] A. Bauch et al. “Comparison between frequency standards in Europe and the USA at the $10^{\hat{a}\hat{\ }'15}$ uncertainty level”. In: *Metrologia* 43 (2006), p. 109. DOI: 10.1088/0026-1394/43/1/016.

[9] J. D. Bekenstein. “Fine-structure constant variability, equivalence principle, and cosmology”. In: *Phys. Rev. D* 66 (2002), p. 123514. DOI: 10.1103/PhysRevD.66.123514.

[10] W. Bernreuther and M. Suzuki. “The electric dipole moment of the electron”. In: *Rev. Mod. Phys.* 63 (1991), p. 313. DOI: 10.1103/RevModPhys.63.313.

[11] S. Borri et al. “Frequency-Noise Dynamics of Mid-Infrared Quantum Cascade Lasers”. In: *IEEE J. Quant. Elec.* 47 (2011), p. 984. DOI: 10.1109/JQE.2011.2147760.

[12] S. Borri et al. “Tunable Microcavity-Stabilized Quantum Cascade Laser for Mid-IR High-Resolution Spectroscopy and Sensing”. In: *Sensors* 16 (2016), p. 238. DOI: 10.3390/s16020238.

[13] Kenneth R Brown. “probing the Electron”. In: *Science* 343.6168 (2014), pp. 255–256.

[14] D. Calonico et al. “High-accuracy coherent optical frequency transfer over a doubled 642-km fiber link”. In: *Appl. Phys. B* 117 (2014), p. 979. DOI: 10.1007/s00340-014-5917-8.

[15] F. Cappelli et al. “Subkilohertz linewidth room-temperature mid-infrared quantum cascade laser using a molecular sub-Doppler reference”. In: *Opt. Lett.* 37 (2012), p. 4811. DOI: 10.1364/OL.37.004811.

[16] S. M. Carroll. “Quintessence and the Rest of the World: Suppressing Long-Range Interactions”. In: *Phys. Rev. Lett.* 81 (1998), p. 3067. DOI: 10.1103/PhysRevLett.81.3067.

[17] C. Clivati et al. “Measuring absolute frequencies beyond the GPS limit via long-haul optical frequency dissemination”. In: *Opt. Express* 24 (2016), p. 11865. DOI: 10.1364/OE.24.011865.

[18] C. Clivati et al. “Planar-waveguide external cavity laser stabilization for an optical link with 10-19 frequency stability”. In: *IEEE Trans. Ultrason. Ferroelectr. Freq. Contr.* 58 (2011), p. 2582. DOI: 10.1109/TUFFC.2011.2121.

[19] The ACME Collaboration et al. “Order of Magnitude Smaller Limit on the Electric Dipole Moment of the Electron”. In: *Science* 343 (2013), p. 6168. DOI: 10.1126/science.1248213.

[20] M. Siciliani de Cumis et al. “Microcavity-Stabilized Quantum Cascade Laser”. In: *Laser Phot. Rev.* 10 (2016), p. 153. DOI: 10.1002/lpor.201500214.

[21] L.S. Cutler and C.L. Searle. “Some aspects of the theory and measurement of frequency fluctuations in frequency standards”. In: *Proc. IEEE* 54 (1966), p. 136. DOI: 10.1109/PROC.1966.4627.

[22] C. Daussy et al. “Direct Determination of the Boltzmann Constant by an Optical Method”. In: *Phys. Rev. Lett.* 98 (2007), p. 250801. DOI: 10.1103/PhysRevLett.98.250801.

[23] P. B. Davies and P. A. Martin. “Diode-laser spectroscopy of $a^3\Pi$ CO”. In: *Mol. Phys.* 70 (1990), p. 89. DOI: 10.1080/00268979000100861.

[24] W. Demtröder. *Laser Spectroscopy: Vol. 1: Basic Principles*. Springer Berlin Heidelberg, 2008.

[25] P. A. M. Dirac. “The Cosmological Constants”. In: *Nature* 139 (1937), p. 323. DOI: 1.

[26] A. Douillet and J.-J. Zondy. "Low-threshold, self-frequency-stabilized $AgGaS_2$ continuous-wave subharmonic optical parametric oscillator". In: *Opt. Lett.* 23 (1998), p. 1259. DOI: 10.1364/OL.23.001259.

[27] L. Dunoyer. "Sur la réalisation d'un rayonnement matériel d'origine purement thermique. Cinétique expérimentale". In: *Le Radium* 8 (1911), p. 142. DOI: 10.1051/radium:0191100804014201.

[28] D. S. Elliott, Rajarshi Roy, and S.J. Smith. "Extracavity laser band-shape and bandwidth modification". In: *Phys. Rev. A* 26 (1982), p. 12. DOI: 10.1103/PhysRevA.26.12.

[29] I. Galli et al. "Comb-assisted subkilohertz linewidth quantum cascade laser for high-precision mid-infrared spectroscopy". In: *Appl. Phys. Lett.* 102 (2013), p. 121117. DOI: 10.1063/1.4799284.

[30] I. Galli et al. "Ultra-stable, widely tunable and absolutely linked mid-IR coherent source". In: *Opt. Express* 17 (2009), p. 9582. DOI: 10.1364/OE.17.009582.

[31] W. Gerlach and O. Stern. "Der experimentelle Nachweis der Richtungsquantelung im Magnetfeld". In: *Z. Physik* 9 (1922), p. 349. DOI: 10.1007/BF01326983.

[32] J. J. Gilijamse et al. "The radiative lifetime of metastable CO (a^3Pi, $v = 0$)". In: *J. Chem. Phys.* 127 (2007), p. 221102. DOI: 10.1063/1.2813888.

[33] R. A. Hegstrom, D. W. Rein, and P. G. H. Sandars. "Calculation of the parity nonconserving energy difference between mirror image molecules". In: *J. Chem. Phys.* 73 (1980), p. 2329. DOI: 10.1063/1.440383.

[34] G. Insero et al. "Difference frequency generation in the mid-infrared with orientation-patterned gallium phosphide crystals". In: *Opt. Lett.* 41 (2016), p. 5114. DOI: 10.1364/OL.41.005114.

[35] G. Insero et al. "Measuring molecular frequencies in the 1–10 μm range at 11-digits accuracy". In: *Sci. Reports* 7 (2017), p. 12780. DOI: 10.1038/s41598-017-12891-6.

[36] K. Kikuchi and T. Okoshi. "Measurement of FM noise, AM noise, and field spectra of 1.3 μ m InGaAsP DFB lasers and determination of the linewidth enhancement factor". In: *IEEE J. Quant. Elec.* 21 (1985), p. 1814. DOI: 10.1109/JQE.1985.1072575.

[37] K. Kikuchi, T. Okoshi, and A. Nakayama. "Novel method for high resolution measurement of laser output spectrum". In: *Elec. Letters* 16 (1980), p. 630. DOI: 10.1049/el:19800437.

[38] I. Kozyryev et al. "Sisyphus Laser Cooling of a Polyatomic Molecule". In: *Phys. Rev. Lett.* 118 (2017), p. 173201. DOI: 10.1103/PhysRevLett.118.173201.

[39] C. Lecaplain et al. “Mid-infrared ultra-high-Q resonators based on fluoride crystalline materials”. In: *Nature Comm.* 7 (2016), p. 13383. DOI: 10.1038/ncomms13383.

[40] T. D. Lee and C. N. Yang. “Question of Parity Conservation in Weak Interactions”. In: *Phys. Rev.* 104 (1956), p. 254. DOI: 10.1103/PhysRev.104.254.

[41] V.S. Letokhov. “On difference of energy levels of left and right molecules due to weak interactions”. In: *Phys. Lett. A* 53 (1975), p. 275. DOI: 10.1016/0375-9601(75)90064-X.

[42] F. Levi et al. “Accuracy evaluation of ITCsF2: a nitrogen cooled caesium fountain”. In: *Metrologia* 51 (2014), p. 270. DOI: 10.1088/0026-1394/51/3/270.

[43] S. A. Levshakov et al. “Searching for chameleon-like scalar fields with the ammonia method”. In: *Astron. Astrophys.* 512 (2010), A44. DOI: 10.1051/0004-6361/200913007.

[44] M. A. Lombardi. “The Use of GPS Disciplined Oscillators as Primary Frequency Standards for Calibration and Metrology Laboratories”. In: *NCSLI Measure J. Meas. Sci.* 3 (2008), p. 56. DOI: 10.1080/19315775.2008.11721437.

[45] Q. Y. Lu et al. “2.4 W room temperature continuous wave operation of distributed feedback quantum cascade lasers”. In: *Appl. Phys. Lett.* 98 (2011), p. 181106. DOI: 10.1063/1.3588412.

[46] R. Maulini et al. “Widely tunable high-power external cavity quantum cascade laser operating in continuous-wave at room temperature”. In: *Electronic Letters* 45 (2009), p. 107. DOI: 10.1049/el:20093057.

[47] L. Moretti et al. “Determination of the Boltzmann Constant by Means of Precision Measurements of H_2O_{18} Line Shapes at 1.39 μm”. In: *Phys. Rev. Lett.* 111 (2013), p. 060803. DOI: 10.1103/PhysRevLett.111.060803.

[48] K.-K. Ni et al. “A dipolar gas of ultracold molecules”. In: *Phys. Chem. Chem. Phys.* 11 (2009), p. 9626. DOI: 10.1039/B911779B.

[49] M. Niering et al. “Measurement of the Hydrogen $1S$-$2S$ Transition Frequency by Phase Coherent Comparison with a Microwave Cesium Fountain Clock”. In: *Phys. Rev. Lett.* 84 (2000), p. 5496. DOI: 10.1103/PhysRevLett.84.5496.

[50] E. B. Norrgard et al. “Submillikelvin Dipolar Molecules in a Radio-Frequency Magneto-Optical Trap”. In: *Phys. Rev. Lett.* 116 (2016), p. 063004. DOI: 10.1103/PhysRevLett.116.063004.

[51] S. Perlmutter. “Nobel Lecture: Measuring the acceleration of the cosmic expansion using supernovae”. In: *Rev. Mod. Phys.* 84 (2012), p. 1127. DOI: 10.1103/RevModPhys.84.1127.

[52] Klaus Petermann. *Laser diode modulation and noise*. Vol. 3. Springer Science & Business Media, 2012.

[53] V. Petrov. "Frequency down-conversion of solid-state laser sources to the mid-infrared spectral range using non-oxide nonlinear crystals". In: *Prog. Quantum Electron.* 42 (2015), p. 1. DOI: 10.1016/j.pquantelec.2015.04.001.

[54] M. de Podesta et al. "A low-uncertainty measurement of the Boltzmann constant". In: *Metrologia* 50 (2013), p. 354. DOI: 10.1088/0026-1394/50/4/354.

[55] M. Pospelov and A. Ritz. "Electric dipole moments as probes of new physics". In: *Ann. Phys.* 318 (2005), p. 119. DOI: 10.1016/j.aop.2005.04.002.

[56] M. Prevedelli, T. Freegrade, and T. W. Hänsch. "Phase locking of grating-tuned diode lasers". In: *Appl. Phys. B* 60 (1995), S241.

[57] G. Quéméner and P.S. Julienne. "Ultracold Molecules under Control!" In: *Chem. Rev.* 112 (2012), p. 4949. DOI: 10.1021/cr300092g.

[58] B. Ratra and P. J. E. Peebles. "Cosmological consequences of a rolling homogeneous scalar field". In: *Phys. Rev. D* 37 (1988), p. 3406. DOI: 10.1103/PhysRevD.37.3406.

[59] D. W. Rein. "Some remarks on parity violating effects of intramolecular interactions". In: *J. Mol. Evol.* 4 (1974), p. 15. DOI: 10.1007/BF01732768.

[60] I. Ricciardi et al. "Frequency-comb-referenced singly-resonant OPO for sub-Doppler spectroscopy". In: *Opt. Express* 20 (2012), p. 9178. DOI: 10.1364/OE.20.009178.

[61] A. G. Riess. "Nobel Lecture: My path to the accelerating Universe". In: *Rev. Mod. Phys.* 84 (2012), p. 1165. DOI: 10.1103/RevModPhys.84.1165.

[62] Boris Sartakov. "Private communications". In: (2016).

[63] A. A. Savchenkov et al. "Optical resonators with ten million finesse". In: *Opt. Express* 15 (2007), p. 6768. DOI: 10.1364/OE.15.006768.

[64] B. P. Schmidt. "Nobel Lecture: Accelerating expansion of the Universe through observations of distant supernovae". In: *Rev. Mod. Phys.* 84 (2012), p. 1151. DOI: 10.1103/RevModPhys.84.1151.

[65] A. Shelkovnikov et al. "Stability of the Proton-to-Electron Mass Ratio". In: *Phys. Rev. Lett.* 100 (2008), p. 150801. DOI: 10.1103/PhysRevLett.100.150801.

[66] P. L. T. Sow et al. "A widely tunable 10-μm quantum cascade laser phase-locked to a state-of-the-art mid-infrared reference for precision molecular spectroscopy". In: *Appl. Phys. Lett.* 104 (2014), p. 264101. DOI: 10.1063/1.4886120.

[67] G. M. Stéphan et al. “Laser line shape and spectral density of frequency noise”. In: *Phys. Rev. A* 71 (4 Apr. 2005), p. 043809. DOI: 10.1103/PhysRevA.71.043809.

[68] H.R. Telle, B. Lipphardt, and J. Stenger. “Kerr-lens, mode-locked lasers as transfer oscillators for optical frequency measurements”. In: *Appl. Phys. B* 74 (2002), p. 1. DOI: 10.1007/s003400100735.

[69] S. Truppe et al. “A search for varying fundamental constants using hertz-level frequency measurements of cold CH molecules”. In: *Nature Comm.* 4 (2013), p. 2600. DOI: 10.1038/ncomms3600.

[70] S. Truppe et al. “Molecules cooled below the Doppler limit”. In: *Nature Phys.* 1 (2017), p. 1. DOI: 10.1038/nphys4241.

[71] P. A. Williams, W. C. Swann, and N. R. Newbury. “High-stability transfer of an optical frequency over long fiber-optic links”. In: *J. Opt. Soc. Am. B* 25 (2008), p. 1284. DOI: 10.1364/JOSAB.25.001284.

[72] C. S. Wu et al. “Experimental Test of Parity Conservation in Beta Decay”. In: *Phys. Rev.* 105 (1957), p. 1413. DOI: 10.1103/PhysRev.105.1413.

[73] J-J. Zondy. “The effects of focusing in type-I and type-II difference-frequency generations”. In: *Opt. Commun.* 149 (1998), p. 181. DOI: 10.1016/S0030-4018(97)00663-9.

This Ph.D. thesis has been typeset by means of the TEX-system facilities. The typesetting engine was pdfLATEX. The document class was `toptesi`, by Claudio Beccari, with option `tipotesi=scudo`. This class is available in every up-to-date and complete TEX-system installation.